ATMOSPHERIC PHYSICS AND CHEMISTRY OF PLUTO'S HAZE LAYERS

by

Adam Jacobs
A Dissertation
Submitted to the
Graduate Faculty
of
George Mason University
in Partial Fulfillment of
The Requirements for the Degree
of
Doctor of Philosophy
Physics

Committee:

_____	Dr. Michael E. Summers, Committee Chair
_____	Dr. W. Dean Pesnell, Committee Member
_____	Dr. Robert Weigel, Committee Member
_____	Dr. Erdal Yigit, Committee Member
_____	Dr. Paul So, Department Chairperson
_____	Dr. Donna M. Fox, Associate Dean, Office of Student Affairs & Special Programs, College of Science
_____	Dr. Ali Andalibi, Dean (Interim), College of Science
Date: _____	Fall Semester 2019 George Mason University Fairfax, VA

Atmospheric Physics and Chemistry of Pluto's Haze Layers

A Dissertation submitted in partial fulfillment of the requirements for the degree of Doctor of Philosophy at George Mason University.

by

Adam Jacobs
Master of Science
George Mason University, 2016
Bachelor of Science
Millersville University, 2012

Director: Michael E. Summers, Professor
Department of Physics and Astronomy

Fall Semester 2019
George Mason University
Fairfax, VA

Copyright 2019 Adam Jacobs
All Rights Reserved

DEDICATION

I dedicate this dissertation to my family and friends—without their support over the years this would not have been possible.

ACKNOWLEDGEMENTS

I would like to thank the many teachers, professors, and research advisers who helped me, and continue to help me, develop as a scientist. Specifically, I would like to thank Dr. Richard Clark and the other faculty in the Earth Science and Physics departments at Millersville University for promising beginnings and opportunities. I would also like to thank Dr. W. Dean Pesnell for his guidance throughout undergraduate and graduate studies and research. At GMU I would like to thank the many faculty in the Physics and Astronomy Department, but in particular Paul So for guiding me through the program, my committee members for their time and efforts helping me develop this thesis, and especially to my advisor Mike Summers for his guidance and patience through my PhD project.

TABLE OF CONTENTS

LIST OF TABLES

LIST OF FIGURES

LIST OF EQUATIONS

ABSTRACT

ATMOSPHERIC PHYSICS AND CHEMISTRY OF PLUTO'S HAZE LAYERS

Adam Jacobs, Ph.D.

George Mason University, 2019

Dissertation Director: Dr. Michael E. Summers

Observations made by the NASA New Horizons (NH) spacecraft mission's flyby of Pluto on July 14, 2015 provided a vast amount of new information on Pluto's surface and atmosphere. The New Horizons observations showed a planet that is geologically active with a diverse surface covered by ices of nitrogen, methane, carbon monoxide, as well as water. We now know these ices buffer its atmosphere through sublimation and drive winds over highly variable terrain containing mountain ranges and a large basin. Pluto's atmosphere supports an extensive circumplanetary haze with embedded layers, suggesting several possible microphysical and/or dynamical excitation processes. The photochemistry leading to the formation of the haze is outlined, as well as timescales for multiple growth processes to understand haze particle lifetime and processing in the context of possible haze layer formation mechanisms. Many haze layers exist in an altitude range where Pluto's atmosphere is highly subsaturated, making local regions of rapid particle growth from supersaturation unlikely. Particles likely grow gradually by

coagulation as they fall through a large altitude region, which also cannot explain the formation of layers with the observed thicknesses. The brightness of the haze and embedded layers is proportional to the line of sight column particle number density—posing the possibility that haze layers form and are made visible by perturbations in haze particle number density. The haze particle sedimentation timescale to traverse the measured average haze layer spacing is much greater than the buoyancy or wave oscillation period in Pluto's atmosphere, supporting the explanation that atmospheric waves are the most likely formation mechanism behind Pluto's complex haze layer structure by wave action imparted on the background sedimenting particles to cause layers of particle compaction and rarefaction. Images of Pluto's limb taken by NH/Long Range Reconnaissance Imager (LORRI) were analyzed here. Several haze layer characteristics were extracted, namely—slope, amplitude, waveform, and the associated power spectral densities (PSDs); and their variations with local geography. These were then explored in the context of possible wave types in Pluto's atmosphere, such as tidal and orographically driven inertia-gravity (buoyancy) waves. A single-scattering model was also adapted to Pluto's atmospheric scattering and LORRI's observing characteristics to simulate images. The scattering model was used to directly compare observations of layers to haze layering generated by an orographic gravity wave model. Qualitative and quantitative comparisons informed which wave types are likely to cause most of the layers observed by NH. Observations, models, and theory are then considered in the context future work for better understanding waves in Pluto's atmosphere is proposed.

CHAPTER ONE

1.1 Introduction

1.1.1 Pluto's History

Clyde Tombaugh discovered Pluto in 1930, and its largest moon Charon was discovered by James Christy in 1978 (Stern *et al.* 1997). Since their discovery, the Pluto-Charon system has drawn much interest due to its major differences from the two main types of solar system planetary categories - terrestrial and gas giant planets. Pluto has a heliocentric orbit with an inclination of 17.2 degrees and an eccentricity of 0.25. Its heliocentric distance ranges from 29.7 AU to 49.3 AU, resulting in a factor of 2.8 in received insolation over the course of its orbit (Young *et al.* 2008). Observed characteristics of Pluto after its discovery classified it as an approximate twin to Neptune's largest satellite Triton—both having a mean density around 2 gcm^{-3}, and radii of 1150-1200 km and 1352 km for Pluto and Triton, respectively. Solar reflection spectra in the near IR indicated several surface ices on Pluto's surface, mainly N_2 and CH_4 (Strobel *et al.* 1996). The solid N_2 absorption band profile was used to estimate a surface temperature of 40±2 K (Tryka *et al.* 1994).

The first measurements showing the existence of Pluto's atmosphere were made by stellar occultations in both near IR and microwave wavelengths in the 1980s (Young *et al.* 2008). These observations indicated an atmosphere composed mainly of N_2, with smaller amounts of CH_4. A warm stratosphere ~ 100 K, and a surface pressure in the range of 3-60 μbar was also estimated. Later observations have shown large changes in Pluto's atmosphere in the years leading up to the New Horizons flyby in July 2015. A series of stellar occultations between 1988 and 2015 indicated an increase in pressure by a factor of three at a reference level of 1275 km from Pluto center, inferring a similar rise in surface pressure (Olkin et al. 2015; Forget et al. 2017).

1.1.2 The New Horizons Mission

There was a rapid expansion in our knowledge of the Pluto system in the 1980's and early 1990's, and the 1992 NASA's Outer Planet Science Working Groups laid out three high priority, nine second priority, and four third priority science objectives to be pursued with a flyby reconnaissance mission. The importance of these science goals was increased by the observations of Pluto's post-perihelion atmospheric expansion, discovery of two additional satellites Nix and Hydra, and spatially resolved measurements of Pluto's temperature, surface composition, and color ultimately leading to and guiding the design of the New Horizons mission (Young *et al.* 2008). A prioritized set of measurement objectives were established for the New Horizons mission, and including color and panchromatic maps, 1.25-2.50 micron spectral images for surface and atmosphere studies, and solar wind interaction measurements which were designed to not only

expand our understanding of the Pluto system, but also to understand its context and similarity to other solar system bodies. Additionally, understanding the similarities between Titan and Pluto was given high priority. Both bodies exhibit surfaces in vapor-pressure equilibrium with a N_2: CH_4 atmosphere (Young *et al.* 2008).

The New Horizons spacecraft was launched on 19 January 2006, and made closest approach with Pluto on 14 July 2015, marking a 9.5-year journey and the first reconnaissance of the Pluto system. The science payload included the Alice (Ultraviolet spectrometer), Ralph/MVIC (Visible panchromatic and color imager), Ralph/LEISA (Infrared imaging spectrometer), REX (Radio Science Experiment), LORRI (High-resolution panchromatic imager), PEPSSI (Energetic particle detector), SWAP (Solar wind analyzer), and SDC (Student-built dust counter) experiments. Observations informing atmospheric studies is the focus of this dissertation. The characterization and composition of the atmosphere was primarily carried out by REX's uplink X-band radio occultations, Alice's extreme and far-ultraviolet solar occultations, and LORRI and MVIC high phase angle imaging (Gladstone *et al.* 2016).

1.1.3 NH Observations: Pluto's Surface and Atmosphere

Perhaps the most breathtaking observations of the Pluto system beamed back to Earth by New Horizons were of its surface features and ices. Figure 1 shows the highest resolution images of Pluto by the Hubble Space telescope that were available before the New Horizons flyby (NASA, ESA, and M. Buie (Southwest Research Institute)).

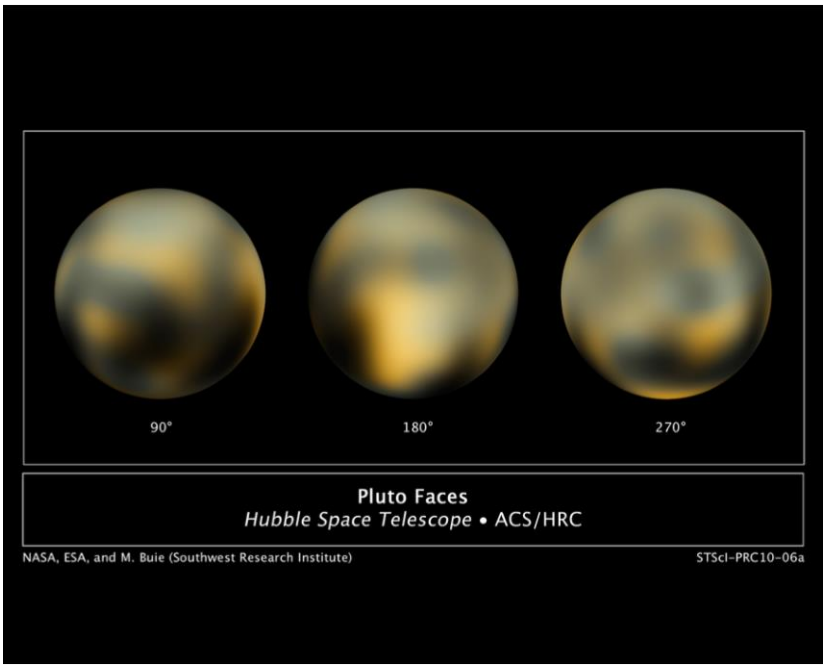

Figure 1: Images of Pluto's surface features, as constructed by Hubble Space Telescope observations of Pluto-Charon mutual eclipses before the New Horizons flyby (NASA, ESA, and M. Buie (Southwest Research Institute)).

Figure 2 shows a composite image taken by the LORRI and RALPH instruments near closest approach to Pluto, with 2.2 km/pixel and 5.0 km/pixel resolutions, respectively, and illustrating the diversity of Pluto's surface features. The heart shaped basin Sputnik Planum (SP, unofficial New Horizons name), is shown as a large smooth icy plain of several million square kilometers. As estimated from shadow length measurements, mountains 2-3 km in height rise above SP's basin. The height of these structures constrains their composition as well as that of material just below the surface. Due to the weak van der Waals-bonds of N_2, CH_4, and CO solids, the existence of a widespread—possibly water based solid just below the surface is strongly suggested (Gladstone *et al.* 2016).

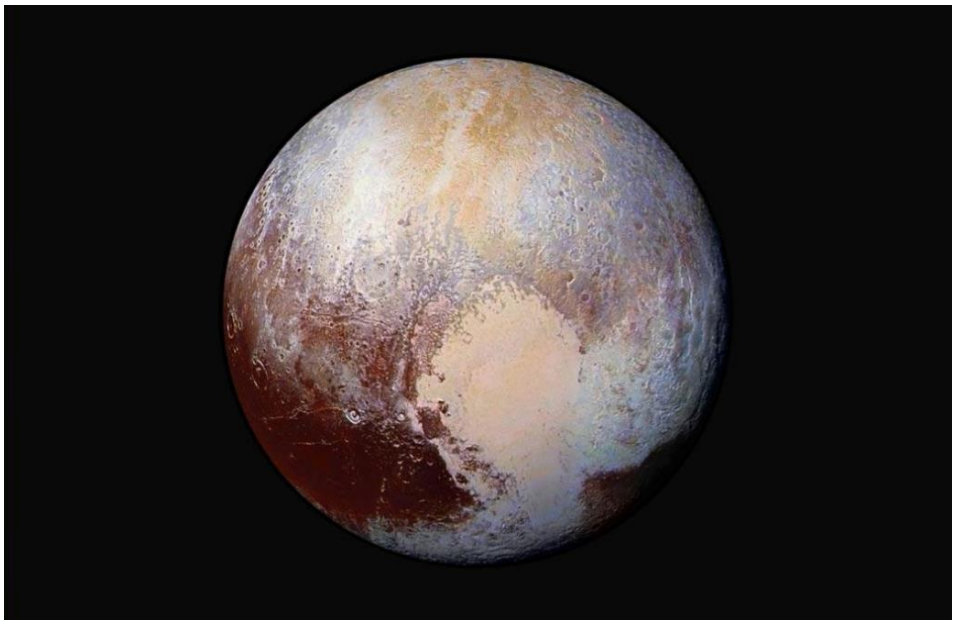

Figure 2: New Horizon's image of Pluto showing the large diversity of surface features, including the heart shaped region informally named Sputnik Planum basin filled with nitrogen ice, as well as the dark region Cthulhu Regio thought to be composed of tholins.

The composition and abundance of surface ices in the SP basin has a large effect on the sublimation driven dynamics and boundary layer characteristics in the overlying atmosphere (Gladstone *et al.* 2016). Confirmation of CH_4 and CO ices (Grundy *et al.* 2013) was made with the RALPH and LEISA instruments, respectively (Gladstone *et al.* 2016). Figure 3 shows a region composed of CH_4 ice (Panel B, Regions of redder color indicating higher amounts) and CO ice (Panel C, White indicating higher concentrations). Panel A is the projection of a LORRI image for the same region. Concentrations were determined from absorption spectra (Stern *et al.* 2015). The western edge of Sputnik Planum is covered primarily by CH_4 ice while the basin is covered primarily of CO,

although large concentrations of N_2 were also detected in the basin (Stern *et al.* 2015). An average surface temperature of ~38 K was also detected for SP (Stern *et al.* 2015).

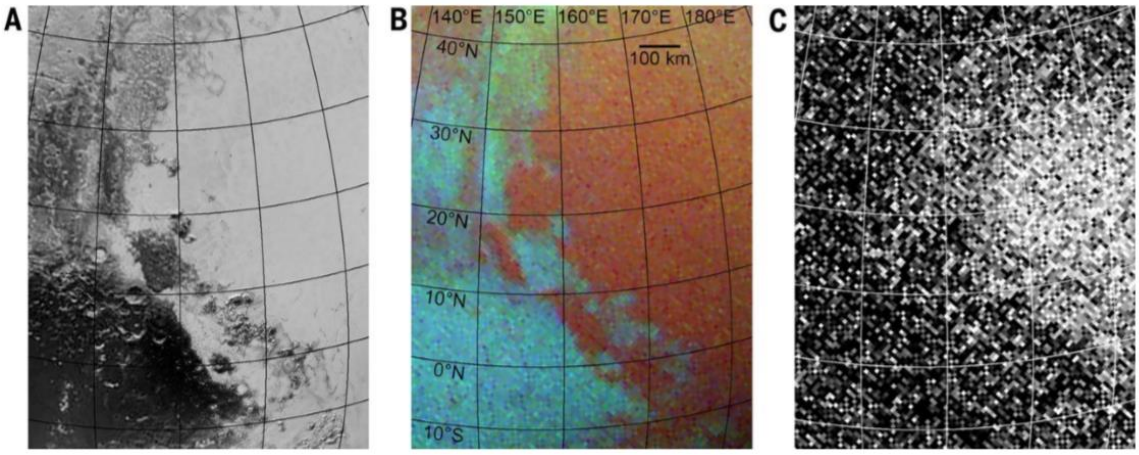

Figure 3: (A) Projection of a LORRI image along the western edge of SP. (B) CH4 ices shown as reddish pixels. (C) CO ices shown as white pixels in the SP basin.

Pluto's atmospheric temperature structure and composition was characterized by the REX and ALICE instruments using radio and solar occultations, respectively (Gladstone *et al.* 2016). REX determined the surface pressure as well as the near surface vertical temperature profiles. Profiles of retrieved pressure and temperature at ingress (Red) and egress (Blue) are shown in Figure 4. These profiles are similar and consistent with sublimation driven dynamics as well as weak horizontal winds (Gladstone *et al.* 2016). The REX profiles are most accurate below ~100 km (Hinson *et al.* 2017), with the variations above 20km caused by measurement uncertainty. The vertical dashed line indicates the saturation temperature of N_2. Most notable is the potential existence of a

boundary layer in the ingress profile, whereas the temperature inversion continues all the way to the surface on egress. This asymmetry in temperature indicates that SP is an active sublimation source that maintains a cold boundary layer over at least part of its surface (Gladstone *et al.* 2016).

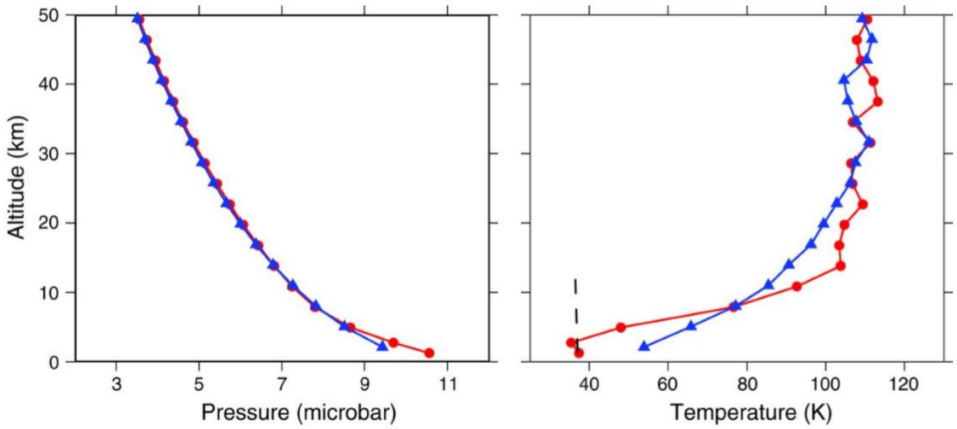

Figure 4: Retrieved temperature and pressure profiles retrieved from the REX radio occultation data at ingress (Red) and egress (Blue). The profiles are seen to deviate most near/at the surface (Hinson *et al.* 2017).

A synoptic map showing where the ingress (entry) and egress (exit) points were located on the surface of Pluto is shown in Figure 5 (Hinson *et al.* 2017).

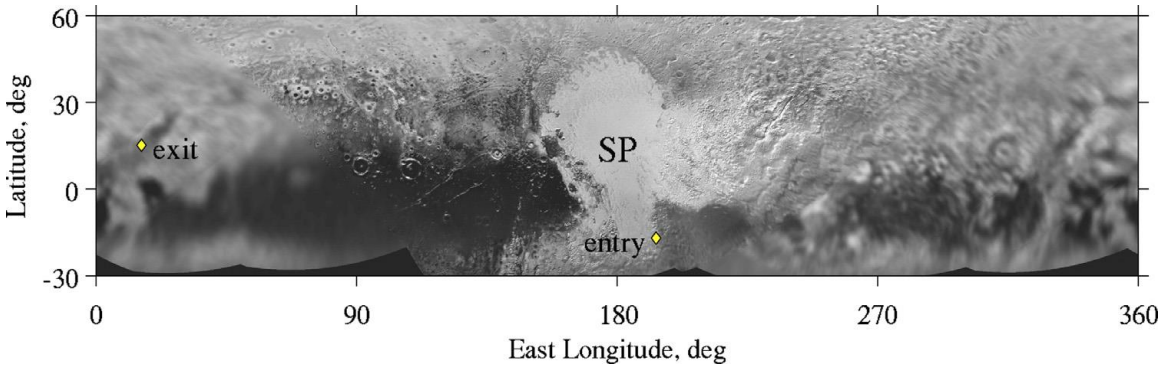

Figure 5: Synoptic map of the Pluto surface indicating the ingress (entry) and egress (exit) points where radio occultations were collected by REX.

The New Horizons ALICE instrument provided atmospheric absorption observations of solar ultraviolet light from which composition was determined along the occultation line-of-sight (LOS). The LOS transmission of UV light between the spacecraft and the sun is shown in Figure 6. Panel A shows transmission predicted from a pre-encounter model atmosphere and Panel B shows the actual transmission data collected by ALICE. Panel C shows model abundances of each constituent as a function of tangent altitude for ingress and egress determined by analysis of the transmission profile (Gladstone *et al.* 2016).

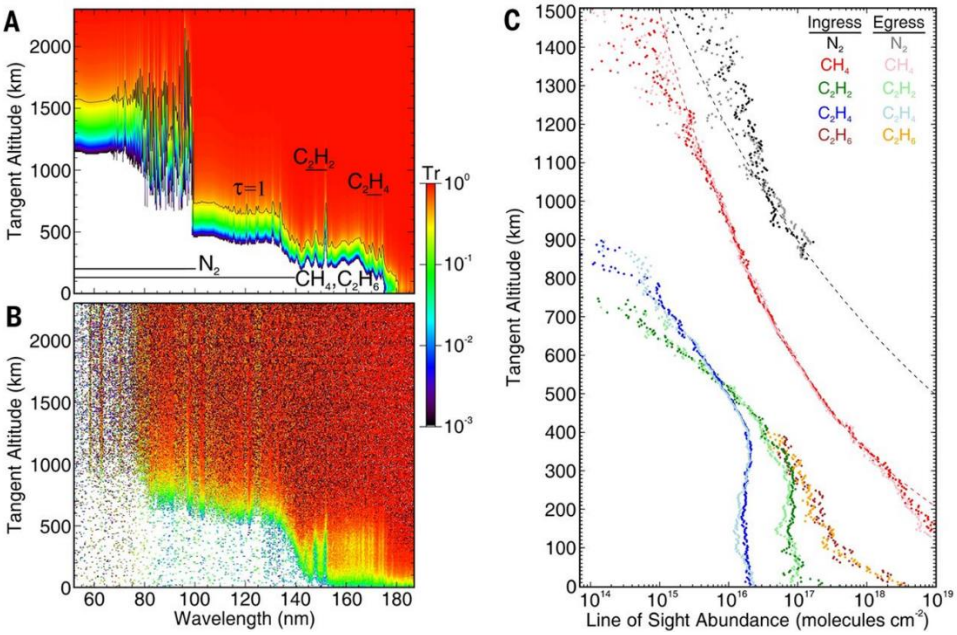

Figure 6: (A) Transmission spectra predicted from a pre-encounter model atmosphere. (B) Transmission spectrum observed by ALICE. (C) LOS column density profiles retrieved from the transmission data of (B) with known absorption cross sections for the given constituents (Gladstone *et al.* 2016).

The most notable features in the transmission spectra are the enormous differences in modeled and observed opacities of CH_4 vs. N_2 at high altitudes. A large opacity of N_2 at wavelengths of 65-100 nm was surprisingly absent in upper atmosphere observations compared to the predictions using pre-flyby models. The upper atmospheric opacity was found to be mainly due to CH_4 from analysis of the Alice observations (Gladstone *et al.* 2016). This result implies that the upper atmosphere is much cooler than expected by the pre-encounter models. The upper atmospheric temperature is constrained to be ~70 K by the observed absorption of N_2 in the 57-64 nm wavelengths (Gladstone *et al.* 2016). Absorption by C_2H_2, C_2H_4, C_2H_6 and haze was also revealed in the transmission spectra, and accounts for most of opacity for wavelengths longer than 100 nm. Deduced model

atmospheric profiles using the transmission data are shown in Figure 6, and the local gravity and scale heights are shown in Figure 7 (Gladstone *et al.* 2016). Pre-encounter model values are shown in dashed lines, and solid lines show the post-encounter model profiles that are consistent with transmission data.

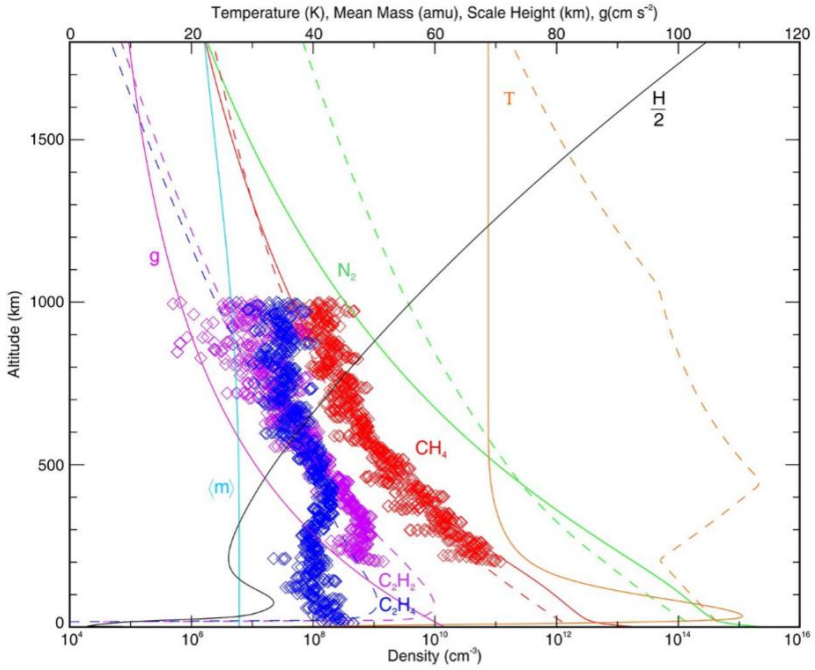

Figure 7: Pre-flyby model C2 hydrocarbon profiles (Dashed), model profiles that agree with transmission spectra (Solid), and data retrieved by occultations (Diamonds) (Gladstone *et al.* 2016).

Photochemical processes are believed to lead to the build-up of the observed C_2 hydrocarbons, which then are lost by attachment to the haze particles that then grow primarily through coagulation. The optically thin haze is seen to extend to an altitude of at least ~200 km, with a brightness scale height of around 50 km (Cheng *et al.* 2017).

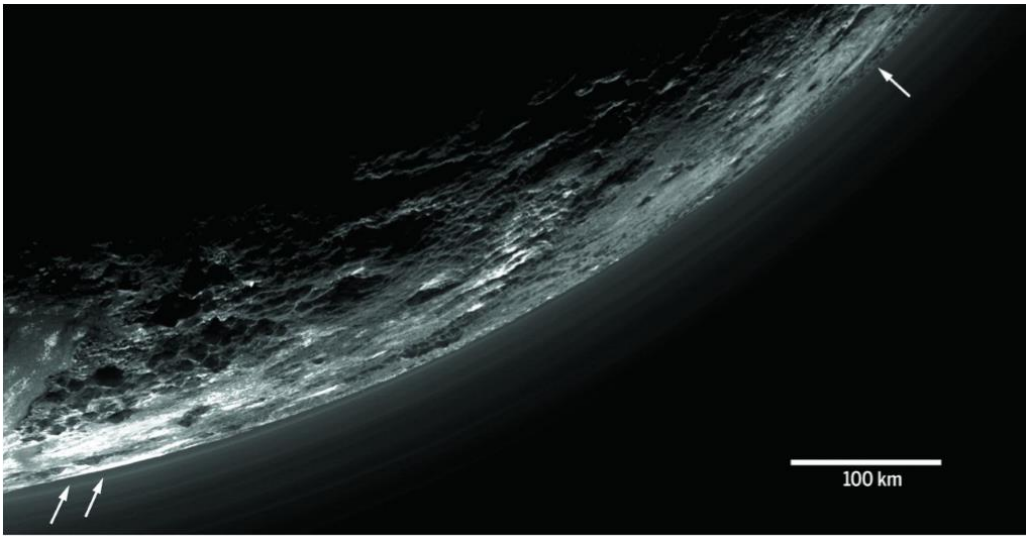

Figure 8: MVIC image of distinct Pluto haze layers above the limb. At least 20 layers are seen to extend of hundreds of kilometers horizontally, with some layers like the one pointed out near limb exhibiting a slight tilt (Cheng *et al*. 2017).

Thin embedded haze layers can be seen to extend more than 100 km horizontally in these images. Figure 8 shows an MVIC image of Pluto's limb and reveals at least 20 layers between the ground and ~200 km altitude. The lowest haze layer (~5-8 km altitude) is tracked with arrows and seen to tilt toward the surface. This image was taken at a phase angle of 147°, showing brightness variations from strongly forward scattered sunlight (Gladstone *et al*. 2016). Figure 9 shows two stacked LORRI images of the haze layers, taken with a phase angle of 169° and resolution of 0.95 km/pixel. The layers are seen to extend above 200 km altitude. The orientation of Pluto's South Pole relative to the spacecraft field of view is shown (Gladstone *et al*. 2016).

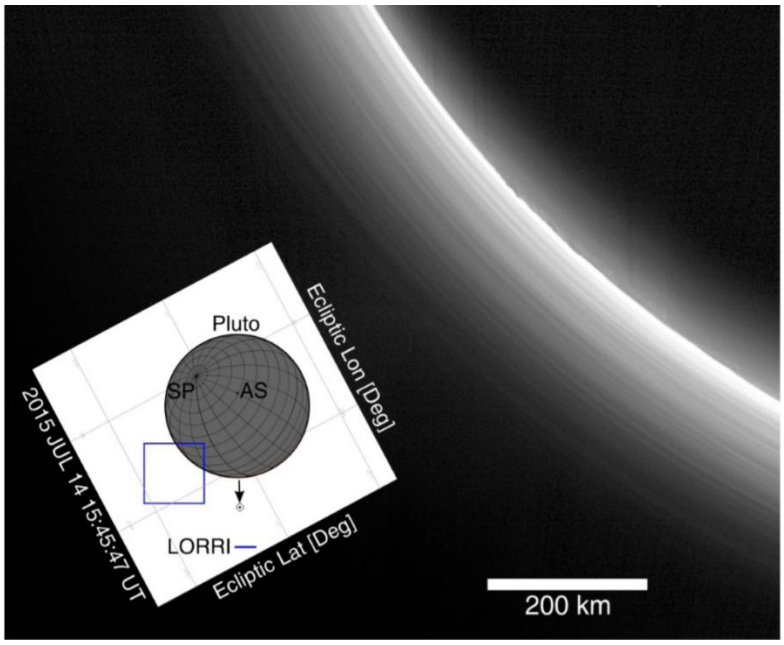

Figure 9: Two stacked LORRI images showing haze layers extending far above Pluto's surface. Pluto's axis orientation relative to the NH field of view and solar position is inlayed (Cheng *et al*. 2017).

1.1.4 Coupling Between Chemistry, Dynamics, and Haze Formation

The processes that produce the observed haze characteristics in Pluto's atmosphere suggest strong coupling between chemistry, small-scale dynamics (microphysics), and large-scale dynamics (atmospheric circulation and oscillations). Chemistry produces hydrocarbons and nitriles because of chemical reactions that follow the photolysis of CH_4 from Lyman-α and of N_2 from solar EUV, respectively (Gladstone *et al*. 2015). Two sources contribute to the photolysis for methane at Pluto—solar and ISM Lyman-α (Gladstone *et al*. 2015). Large ions produced at high altitudes in the ionosphere act as condensation nuclei for the hydrocarbons and nitriles. The concentrations of photochemical products available for condensation onto the haze

particles can be determined from the observed atmospheric absorption measurements along with photochemical models constrained by those observations as shown in Figure 6 and Figure 7 (Gladstone *et al*. 2016). The hydrocarbon concentrations and their variation with altitude are extremely important in determining the composition of haze particles—which influence their structure and scattering properties. Atmospheric dynamical transport processes then transport the molecules, nuclei, and particles both vertically and horizontally.

The observed haze has a blueish color, indicating Rayleigh scattering by small particles (monomers) around 10 nm and larger. Measurements over a large range of phase angles (15-169°) show a strongly forward scattered peak in I/F at large phase angles, indicating haze with larger particles (> 0.2 μm). Once nucleation has occurred and condensational growth has produced the monomers, coagulation is believed to dominate the growth of the haze particles by Brownian motion and gravitational sedimentation. Surface interactions are then thought to be significant processes for these larger particles, acting to round them and as a sink for molecules like hydrocarbons by condensation. An analog has been drawn between nucleation processes on Pluto, Titan, and Triton (Gladstone *et al*. 2016; Cheng *et al*. 2017).

Gravity (buoyancy) waves are thought to be a dominant dynamical process leading to the production of observed bright and thin embedded layers. The generation, vertical propagation, and haze layer generation by gravity waves is largely the focus of this dissertation.

1.1.5 Key Science Questions Addressed by This Dissertation

Many questions about Pluto's formation and evolution were answered from the analysis of New Horizons observations during the fly-by, but many additional questions were raised from the surprising nature of its atmosphere. Questions most relevant to this dissertation include the following: (1) What are the scales and geographic variation of the haze layers and their associated driving mechanism(s)? (2) How are layers formed from the background haze particles? (3) Are gravity waves the dominant process for producing the thin layers? (4) Are the haze layers we see in LORRI and MVIC images generated mainly by thermal tides or orographically forced gravity waves? (5) Layers appear tilted—what is the dominant process behind this tilting and can the tilt orientation and magnitude be used to test dynamical models and constrain horizontal winds?

1.2 Pluto's Atmospheric Structure and Mean State

1.2.1 Pressure and Temperature Processes

Observations of a distinct kink in an Earth-based stellar occultation light-curve near 1215 km (from Pluto disk center) suggested the existence of either a strong near-surface temperature inversion or a thin haze layer (Summers *et al*. 1997). As shown in Figure 4, the New Horizons observations during ingress and egress show a strong temperature inversion above the cold icy surface of Sputnik Planum, with a possible shallow boundary layer detected on ingress (Gladstone *et al.* 2016). It is believed that this boundary layer is produced over regions of sublimation that drive upward flux and cooling (Gladstone *et al.* 2016). However, this boundary layer is thought to be extremely shallow due to the higher altitude temperature inversion inhibiting boundary layer convection. The observed narrow temperature decrease above SP is better characterized as a local boundary layer than as a troposphere (Gladstone *et al*. 2016).

The increase in temperature with altitude above the boundary layer is attributable to the absorption of solar radiation by the 3.3 μm CH_4 bands. The cause(s) of the decrease to cooler temperatures at much higher altitudes in the atmosphere (and specifically how cool the upper atmosphere becomes) is still poorly understood. Possible explanations include cooling by CH_4 7.6 μm band radiation, cooling by C_2H_2 ν_5 band emission, and/or HCN line emission, or cooling by water vapor deposited in the upper atmosphere by cosmic dust ablation (Strobel *et al.* 1996; Gladstone *et al.* 2016; Poppe 2017). The most

recent explanation involved absorption and radiative loss/cooling to space by an extensive haze in Pluto's atmosphere (Zhang *et al*. 2017).

The vertical temperature profile is mainly consistent with a model of the atmosphere consisting of two domains - a clear upper atmosphere with a small negative temperature gradient and a lower atmosphere with a large positive gradient and haze layer. An example of the pre-NH occultation data and corresponding models are shown in Figure 10 (Olkin *et al*. 2015). Models suggest that climatic changes in Pluto's temperature and pressure occur over timescales of 800,000 years (Stern *et al*. 2017; Forget *et al*. 2017). Pluto's eccentric orbit (e=0.26) and high obliquity (102-126°) cause large variations in insolation. Also, stellar occultations between 1988-2015 show a three-fold increase in pressure during this much shorter time period (at ~1215 km distance from Pluto center) (Olkin *et al*. 2015).

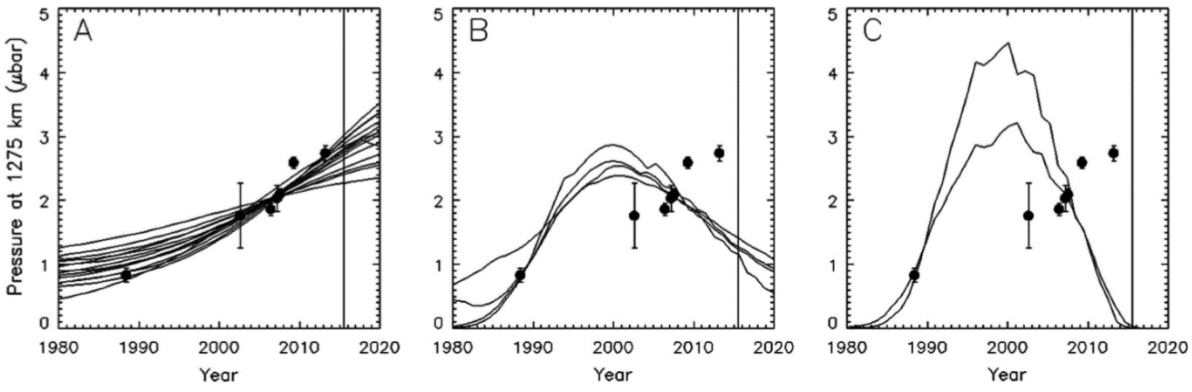

Figure 10: Observed and retrieved pressure data showing a 3-fold pressure increase from 1988 to 2014. Models of the surface pressure are shown along with the occultations for three different model atmosphere scenarios. Only the first reproduces observations of the pressure increase (Olkin *et al*. 2015).

Pluto's atmosphere has many similarities to the atmospheres of Titan and Triton (Summers *et al*. 1997; Krasnopolsky and Cruikshank, 1999; Lavvas *et al*. 2010). Figure 11 shows the temperature profiles for all three atmospheres, with locations of the haze layers for Titan and Pluto. Pluto's haze occurs at the same pressure levels as Titan's detached haze layer (1-10 μbar, Cheng *et al.* 2017), and in a pressure/temperature regime where the temperature is too high for direct condensation of known hydrocarbons and nitriles (Lavvas *et al*. 2010, Cheng *et al*. 2017). The atmospheric composition is very similar for Titan, Triton, and Pluto—all dominated by N_2 and containing CH_4 in smaller amounts, but still enough for photochemistry to produce a variety of chemical products that are initiated by methane photolysis. Many similarities exist between Triton and Pluto's ionospheric photochemistry as well, and perhaps similar nucleation processes. However, Pluto's haze microphysics is believed to be more analogous to Titan's detached haze layer—specifically when coagulation becomes the dominant growth process for the aerosol particles (Lavvas *et al*. 2010).

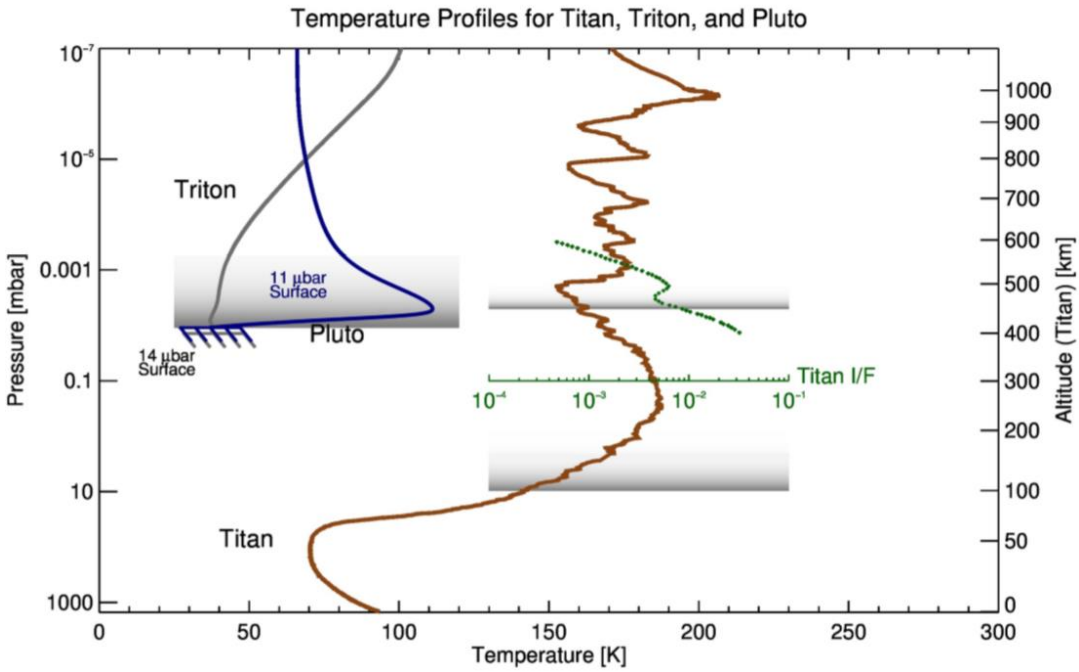

Figure 11: Comparison of temperature structures of Pluto, Titan, and Triton. Pluto's haze layer is in the same pressure regime as Titan's detached haze layer (Cheng *et al.* 2017).

1.2.2 Atmospheric Photochemistry

Photolysis and ionization of N_2 and CH_4 initiates the chemical production of nitriles and higher order hydrocarbons in all three atmospheres Titan, Triton, and Pluto, only a few of which (C_2H_2, C_2H_4, and C_2H_6) were observed by ALICE in Pluto's atmosphere (shown in Figure 7). The main driver of Pluto's photochemistry is the photochemical destruction of CH_4 by solar and interplanetary Lyman-α. The chemical branches are:

Equation 1

$$\begin{aligned} CH_4 + hv &\rightarrow CH_3 + H \\ &\rightarrow CH + H + H_2 \\ &\rightarrow C(1D) + 2H\,, \end{aligned}$$

with the first two accounting for most of the photolysis products. The efficiency of methane destruction can be reduced by 3-body recombination of the methyl radical in

Equation 2

$$CH + CH_3 + M \rightarrow CH_4 + M\,,$$

which is significant on Titan but is relatively slow at the low atmospheric pressures in Pluto's atmosphere. The higher order hydrocarbons are produced by reactions such as

Equation 3

$$\begin{aligned} CH_3 + CH_3 + M &\rightarrow C_2H_6 + M \\ CH + CH_4 &\rightarrow C_2H_4 + H\,. \end{aligned}$$

Ethane (C_2H_6) is photolyzed and leads to

Equation 4

$$\begin{aligned} C_2H_6 + hv &\rightarrow C_2H_4 + H_2 \\ &\rightarrow C_2H_4 + 2H \\ &\rightarrow C_2H_2 + 2H_2\,. \end{aligned}$$

Ethylene (C_2H_4) photolysis is an efficient source of C_2H_2, which in turn is photolyzed to

Equation 5

$$C_2H_2 + hv \rightarrow C_2H + H\,.$$

A product of this reaction, C_2H, then participates in the catalytic destruction of methane and ethane to recover additional acetylene through

Equation 6

$$C_2H + CH_4 + M \rightarrow C_2H_2 + CH_3$$
$$C_2H + C_2H_6 \rightarrow C_2H_2 + C_2H_5\,.$$

The concentration of H controls the ultimate methane destruction efficiency. Photochemistry of methane and the higher order hydrocarbons also produces H and H_2 that are transported upwards to the ionosphere, where ion-molecule reactions and/or escape from the top of the atmosphere can take place. The photochemistry of N_2 also leads to the release of H.

One chemical pathway that is important for aerosol formation is the production of nitriles that may act as nucleation sites. Most of the EUV absorbed by the upper atmosphere and ionosphere of Pluto is by N_2. There is an important coupling between the neutral atmosphere and the ionosphere that produces atomic nitrogen. Atomic N mostly diffuses to the exobase (around 1562-1662 km altitude; Gladstone *et al.* 2016) where it escapes, but a considerable amount diffuses downward into the CH_4 photochemical region where it interacts with several photochemical products. Due to its relatively low

density, N is not lost through 3-body recombination to N_2, but instead to the following chain of reactions:

Equation 7

$$\begin{aligned} N + CH_3 &\rightarrow H_2CN + H \\ H_2CN + H &\rightarrow HCN + H_2 \\ HCN + hv &\rightarrow H + CN\,. \end{aligned}$$

Once the cyanogen (CN) radical is produced, it readily reacts with several molecules to produce additional nitriles through

Equation 8

$$\begin{aligned} CN + C_2H_6 &\rightarrow HCN + C_2H_5 \\ CN + C_2H_2 &\rightarrow HC_3N + H \\ CN + C_2H_4 &\rightarrow C_2H_3CN + H \\ CN + HC_3N &\rightarrow C_4N_2 + H\,. \end{aligned}$$

The above processes provide a net loss of N that is replenished by the sublimation of N_2 ices on Pluto. A small amount of N_2 is also produced by

Equation 9

$$N + NH \rightarrow N_2 + H\,.$$

The above processes act as the main photochemical pathways for the neutral atmosphere, (taken from Summers *et al.* 1997). The major condensing nitriles, at higher altitudes than the hydrocarbons, are HCN, C_2H_3CN, and C_4N_2.

Another aspect of the atmospheric chemistry important in the formation of nucleation sites is ion-molecule photochemistry in the ionosphere. Although Pluto is subjected to the solar wind, the high conductivity of the ionosphere prevents ionizing particles from penetrating to the same level as does EUV radiation. Starlight ionization is relatively unimportant for the day-side of Pluto but may contribute on the night-side. The conclusion is that solar EUV is the main driver of Pluto's ionosphere, with initial ionization branches

Equation 10

$$\begin{aligned} N_2 + \begin{pmatrix} hv \\ e^* \end{pmatrix} &\rightarrow N_2^+ + e \\ &\rightarrow N^+ + N + e\,. \end{aligned}$$

Above, e^* denotes a photoelectron. As discussed before, H_2 and H diffuse upward into the ionosphere, where the following charge exchange reactions can occur:

Equation 11

$$\begin{aligned} N_2^+ + H_2 &\rightarrow N_2H^+ + H \\ N_2^+ + H &\rightarrow H^+ + N_2\,. \end{aligned}$$

Recombination occurs dissociatively for molecular ions leading to

Equation 12

$$N_2H^+ + e \rightarrow N_2 + H$$
$$N_2^+ + e \rightarrow N(2D) + N$$
$$N(2D) \rightarrow N + hv\,,$$

and radiatively (and thus much more slowly) for atomic ions by

Equation 13

$$N^+ + e \rightarrow N + hv$$
$$H^+ + e \rightarrow H\,.$$

The photolysis of CH_4, and the reactions between CN and N, provide carbon for the following charge exchange reaction:

Equation 14

$$N_2^+ + C \rightarrow C^+ + N_2\,.$$

The resulting ionosphere from the above reactions would be expected to be dominated by N^+, C^+, N_2^+, and N_2H^+ with the relative proportions of ions determined by the H, H_2, and C production rates.

New Horizons observed an upper atmosphere relatively rich in CH_4, and Earth based observations suggest considerable CO is present in the upper atmosphere (Lellouch

et al. 2016). The following charge exchanges will occur with nitrogen ions because of the higher concentration of CH_4:

Equation 15

$$\begin{aligned} N_2^+ + CH_4 &\rightarrow CH_3^+ + N_2 + H \\ N^+ + CH_4 &\rightarrow CH_3^+ + NH \\ &\rightarrow H_2CN^+ + H_2 \\ N_2H^+ + CH_4 &\rightarrow CH_5^+ + N_2 \end{aligned}$$

These exchanges will be followed by

Equation 16

$$CH_3^+ + CH_4 \rightarrow C_2H_5^+ + H_2 \, .$$

All these reactions act to decrease nitrogen ion densities and produce an ionosphere containing CH^+, CH_2^+, CH_3^+, CH_5^+, and $C_2H_5^+$ (Summers *et al.* 1997).

CO acts to add carbon atoms to the atmosphere by

Equation 17

$$\begin{aligned} N_2^+ + CO &\rightarrow CO^+ + N_2 \\ N^+ + CO &\rightarrow CO^+ + N \\ &\rightarrow NO^+ + C \\ CO^+ + e &\rightarrow C + O \\ NO^+ + e &\rightarrow N + O \, . \end{aligned}$$

The water content in Pluto's atmosphere is highly uncertain. The main source of water is thought to be the ablation of meteoroids/solar system dust (Poppe 2017). Even with small amounts of water the following charge-exchange reactions are fast and could prevent N^+ from becoming a major ion by

Equation 18

$$\begin{aligned} N^+ + H_2O &\rightarrow H_2O^+ + N \\ N_2^+ + H_2O &\rightarrow H_2O^+ + N_2 \\ &\rightarrow N_2H^+ + OH\,. \end{aligned}$$

The chemical interactions involved when H_2O is highly abundant are complex and, in many cases, rapid. A few of the ions produced from these interactions would include HCO^+, CH_3O^+, and H_3O^+ with H_3O^+ expected to be the dominant ion (Summers *et al.* 1997).

Before the New Horizons mission, several photochemical modeling studies predicted the concentration profiles of a wide range of plausible constituents in Pluto's atmosphere. It became apparent in all of these studies that there was considerable sensitivity of the model results to the CH_4 surface layer mixing ratio and to the assumed model eddy diffusion coefficient profile. In the study by Summers *et al.* (1997), three cases were considered—(A) Triton Analog, where N_2 and CH_4 surface partial pressures were determined by ices at 35 K, (B) High CH_4 atmosphere, with a larger CH_4 source such as pure CH_4 ice with a higher equilibrium vapor pressure than the N_2 ice, and (C) A Pluto Mean Atmosphere, with mean orbit conditions and a surface equilibrium at 31 K.

The New Horizons observations revealed that Case (B) was based closest to the actual conditions. For this case, the surface mixing ratio of CH_4 was set to 4×10^{-2}. The mixing ratio was also assumed to be constant with altitude—a consequence of its escape flux being at the Jeans limit. The peak altitude of the electron density was found to be around 1200 km, with an ionosphere dominated by CH^+, CH_2^+, $C_2H_5^+$, and CH_5^+ (Summers *et al.* 1997).

Establishing the CH_4 mixing ratio profile is of utmost importance, as its column integrated destruction rate controls the downward mass flux of photochemical products (the best model agreement with NH observations found $\approx 1.2\times10^{-14}$ $gcm^{-2}s^{-1}$ by Gao *et al.* 2016). Once the higher concentration of CH_4 in Pluto's atmosphere was established, Krasnopolsky and Cruikshank (1999) conducted a photochemical study with a background model incorporating a hydrodynamically escaping Pluto atmosphere near perihelion (~30 AU). They found that due to the higher methane abundance the resulting photochemistry was more like Titan than Triton. The observed column abundance of CH_4 gas at the time was 3.2 (+8.5/-2.3) $\times$ 10^{19} cm^{-2}. This high abundance of CH_4 results in a significant reduction in N due to charge exchange between N_2^+ and CH_4. That study also found that the most abundant photochemical products were those listed in Table 1, with their respective column densities (Krasnopolsky and Cruikshank 1999).

Table 1: A list of the most abundant photochemical products in an atmosphere with a relatively high methane concentration, given many of the reactions outlined above (Krasnopolsky and Cruikshank 1999).

KC 1999 Photochemical Products [cm^{-2}]	
Product	Column Density
C_2H_2	3×10^{17}
C_4H_2	1×10^{17}
HCN	6×10^{16}
H_2	4×10^{16}
C_2H_4	4×10^{16}
HC_3N	3.4×10^{16}
C_2H_6	2×10^{16}
C_3H_2	9×10^{15}
C_3H_4	8×10^{15}

Most notable are the hydrocarbons C_2H_2, C_2H_4, and C_2H_6 that were observed in the NH flyby observations (Gladstone *et al*. 2016). Krasnopolsky and Cruikshank (1999) predicted the detectability of those hydrocarbons in a fly-by mission, for which the minimum column density for a constituent to be detectable given by

Equation 19

$$N = \frac{0.1}{\sigma\sqrt{\frac{2\pi r}{H}}} \approx 10^{15} cm^{-2}.$$

With a cross section (σ) of 10^{-17} cm^2 and limiting value of UV occultation spectroscopic absorption optical depth of 0.1, many of the predicted hydrocarbons were also predicted to be detectable. For the model ionosphere, it was found that the electron density peaked at ~800 cm^{-3} near 2250 km altitude (much higher than Summers *et al*. 1997), with dominating ions being $HCNH^+$, $C_3H_3^+$, and $C_3H_5^+$.

One of the main issues with the Krasnopolsky and Cruikshank (1999) photochemical model were the assumed temperature profile. Observations by NH show that the upper atmosphere is much cooler than expected, and that a troposphere is almost certainly non-existent, albeit with a possible shallow boundary layer observed at ingress (Figure 4) (Gladstone *et al.* 2016).

The NH Alice data for methane absorption above 200 km tangent altitude, and thus the inferred C_2 hydrocarbons in the altitude range of 200-800 km, are the most robust (high S/N). Above 800 km tangent altitude the signal-to-noise ratio becomes too small to detect C_2 trace species. Below 200 km tangent altitude the measurements are no longer sensitive to CH_4 absorption, because most of the photons below 140 nm have been absorbed. This lack of measured absorption for CH_4 also makes the retrieved values for C_2H_6 unphysical and those for C_2H_2 "untrustworthy" in that region. However, because C_2H_4 has easily identifiable spectral features, the derived abundances are reasonably confident from 800 km down to the surface.

The Alice instrument was unable to detect CO and HCN in the atmosphere, but the Atacama Large Millimeter/submillimeter Array (ALMA) detected trace amounts of both in June 2015 (CO (3-2) and HCN (4-3) rotational transitions were observed, Lellouch *et al.* 2017). The detection of CO probed the region from ~450 km to the ground, and HCN from ~900 km to the ground. The mole fraction of CO was found to be 515 ± 40 ppm with an assumed 12 μbar surface pressure (Lellouch *et al*. 2017). The observed HCN line shape implies a large abundance in the upper atmosphere, with a mole fraction > 1.5×10^{-5} above 450 km and 4×10^{-5} near 800 km, respectively. This

suggests that HCN is highly supersaturated at the inferred low temperatures in the upper atmosphere (Lellouch *et al*. 2017).

A post-flyby photochemical model study was conducted by Wong *et al*. (2017) who used the Caltech/JPL photochemical-vertical transport model KINETICS with the aim of reproducing the observations of CH_4 and the C_2 hydrocarbons, and to predict abundances of other species not yet detectable. It is important to note that the altitude ranges where the NH Alice data is most reliable when comparing with current photochemical model output is 200-800 km altitude. Alice gives reliable measurements for CH_4 above 200 km, hydrocarbons for 200-800 km. But the signal-to-noise ratio is too small for trace species' abundances above 800 km. Below 200 km almost all photons attributed to CH_4 are absorbed, causing unreliable results for retrieved C_2H_2 and C_2H_6. However, due to spectral features of C_2H_4, these measurements/data are reliable from 800km down to the surface. Like previous model studies, KINETICS assumes a spherically symmetric atmosphere. The KINETICS chemical production and loss budget is calculated using the 1D continuity equation

Equation 20

$$\frac{\partial n_i}{\partial t} + \frac{1}{r^2}\frac{\partial (r^2 \varphi_i)}{\partial r} = P_i - L_i \,,$$

with n_i being the number density for species i, φ_i the vertical flux, P_i and L_i the chemical production and loss rates, respectively (all evaluated at time t) and radius $r = r_0 + z$ (z defined as altitude above surface). The vertical flux is defined as

Equation 21

$$\varphi_i = -\frac{\partial n_i}{\partial r}(D_i + K_{zz}) - n_i\left(\frac{D_i}{H_i} + \frac{K_{zz}}{H_{atm}}\right) - \frac{\partial T}{\partial r}\left[\frac{(1+\alpha_i)D_i + K_{zz}}{T}\right]$$

where D_i is the molecular diffusion coefficient, H_i the species scale height, H_{atm} the atmosphere scale height, α_i the thermal diffusion parameter, K_{zz} the vertical eddy diffusion coefficient, and T the temperature. Inputs for this model include the temperature and pressure profiles. The most consistent pressure and temperature model atmosphere is that determined by Strobel *et al*. (2017) which were constrained by REX measurements at low altitudes and the Alice observations at high altitude (Wong *et al.* 2017). The CH_4 profile was then fit by varying the surface mixing ratio and assuming a specified profile for the vertical eddy mixing coefficient to initialize the photochemical model.

There is significant uncertainty in the loss term of the 1D continuity equation due to the condensation of hydrocarbons and nitriles upon condensation nuclei—a process that is believed to be very rapid below the ~200 km region. This condensation loss rate for a condensable species is given by

Equation 22

$$J = \frac{1}{4}\gamma \upsilon A N \, .$$

where γ is the sticking coefficient, υ the thermal velocity, A the total surface area per unit volume of the aerosol particles, and N the particle density of aerosols. Due to the

complex nature of this loss process on aerosols (a consequence of their unknown shapes and compositions), this rate is highly uncertain (Gao *et al*. 2017). The effect of this uncertainty was explored through variation of the sticking coefficient (Best fits given by $\gamma_{C2H2} = 3 \times 10^{-5}$, $\gamma_{C2H4} = 1 \times 10^{-4}$, $\gamma_{C2H6} = 3 \times 10^{-6}$, and $\gamma_{HCN} = 1 \times 10^{-2}$). Another source of uncertainty in the photochemical modeling of hydrocarbons is the poorly known saturation vapor pressure of C_2H_4.

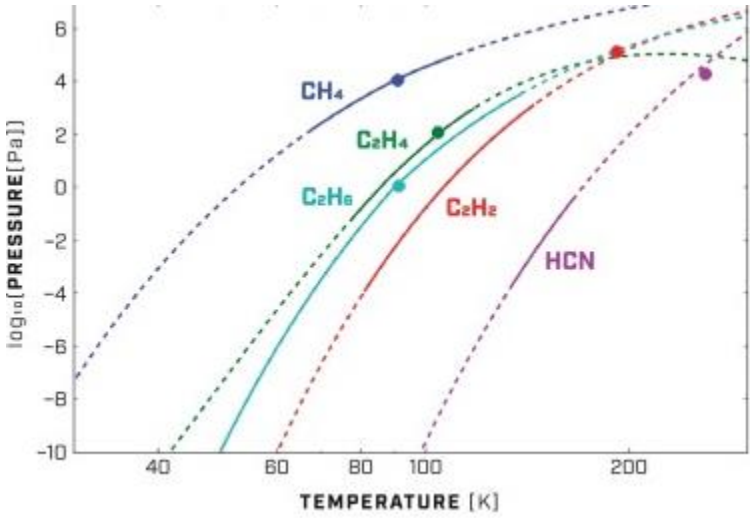

Figure 12: Saturation vapor pressures for major hydrocarbons observed in Pluto's atmosphere, as shown in Wong *et al.* (2017). The unknown region of saturation vapor pressure for C_2H_4 is shown by the green dashed extrapolation line.

The temperature-pressure regime of Pluto's surface and atmosphere presents a previously unexplored low temperature region for the study of planetary atmospheres and such comparisons to laboratory experiments. Wong *et al*. (2017), Figure 12 shows the saturation vapor pressures for the major hydrocarbons they studied. Best fits for the

concentrations of several hydrocarbons with Alice data are shown in Figure 13. The cavity in hydrocarbon concentration around 200 km hypothesized to be caused by condensation onto the haze particles, is shown for C_2H_2 and C_2H_4, but not C_2H_6. This is likely due to an incomplete understanding in the microphysics and saturation vapor pressure of C_2H_6. The saturation vapor pressure and condensation behavior of C_2H_6 has yet to be measured for Pluto's T-p regime. The saturation vapor pressure for C_2H_2 was assumed to be the same as C_2H_4 in the model.

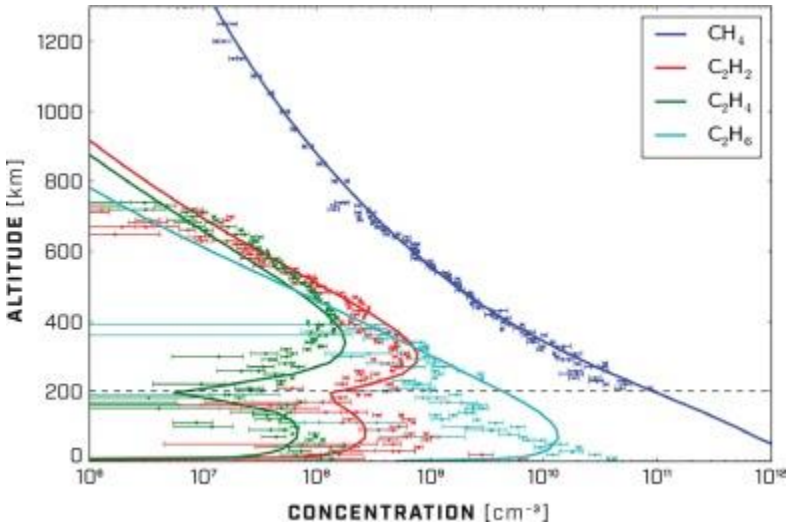

Figure 13: Concentration profiles for the major hydrocarbons produced in the Wong *et al*. (2017) photochemical model. Observations are data points and solid lines are model fits. The "cavity" near 200 km altitude that is likely due to condensation can be seen clearly.

One way to quantify the total column loss rate of hydrocarbons is by the precipitation rates. A comparison of precipitation rates for several photochemical products between Krasnopolsky and Cruikshank (1999) and Wong *et al.* (2017) is given

in Table 2. Differences in these rates for the simpler hydrocarbons are attributed to the better knowledge of the photochemical rate coefficients, eddy mixing coefficient, and model atmosphere.

Table 2: Comparison of the photochemical models produced precipitation rates for major constituents.

Species Precipitation rates [$gcm^{-2}Gyr^{-1}$]		
Species	Precip. rate Wong 2016	Precip. rate KC 1999
C_2H_2	179	195
C_2H_4	95	18
C_2H_6	62	27
CH_3C_2H	48	
HCN	35	42
C_6H_6	34	
C_4H_2	26	174
C_3H_6	8	
CH_3C_2CN	6	
H_6C_3N	4	69

As previously mentioned, the water content of the atmosphere may also be important in Pluto's photochemistry. In the study by Poppe (2015), the water source was assumed to be solely from ablation of dust grains. The influx of dust at the time of NH flyby was assumed to be about 1.4×10^{-17} $gcm^{-2}s^{-1}$. Assuming a composition of pure water ice, this corresponds to a H_2O influx of 5×10^5 molecules $cm^{-2}s^{-1}$. This is enough water to significantly influence the photochemistry and could also play a role in cooling the upper atmosphere. Incorporating assumed abundances of CO and H_2O derived from earlier observations and models (Lellouch *et al*. 2017; Poppe 2015), the photochemical

model (Wong *et al.* 2017) predicted abundances of several oxygen-bearing molecules. These can be seen in Figure 14.

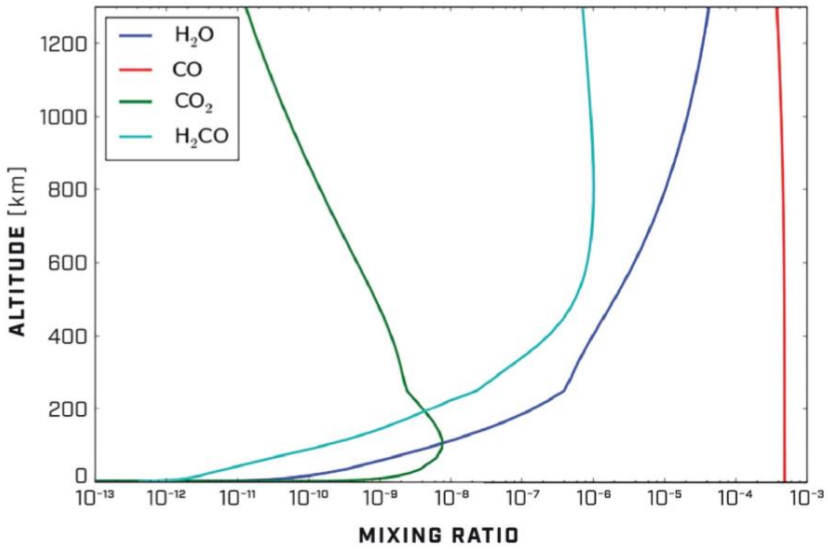

Figure 14: Mixing ratio predictions for major oxygen bearing molecules that may be confirmed with future measurements and missions (Wong *et al*. 2017).

1.2.3 Atmospheric Haze and Embedded Layers

An extensive, optically thin haze was observed in Pluto's atmosphere during the New Horizons fly-by on July 14, 2015. A background haze indicative of Rayleigh scattering by small particles can be observed to altitudes greater than 200 km above the limb. The MVIC blue/red ratio increases with distance from the limb, suggesting smaller particles with higher altitude. I/F increases toward the surface, with a maximum just

above the limb of around 0.22. The haze is not homogeneous with Latitude and Longitude. Specifically, the haze is brighter towards northern Latitudes. This becomes apparent in Figure 15.

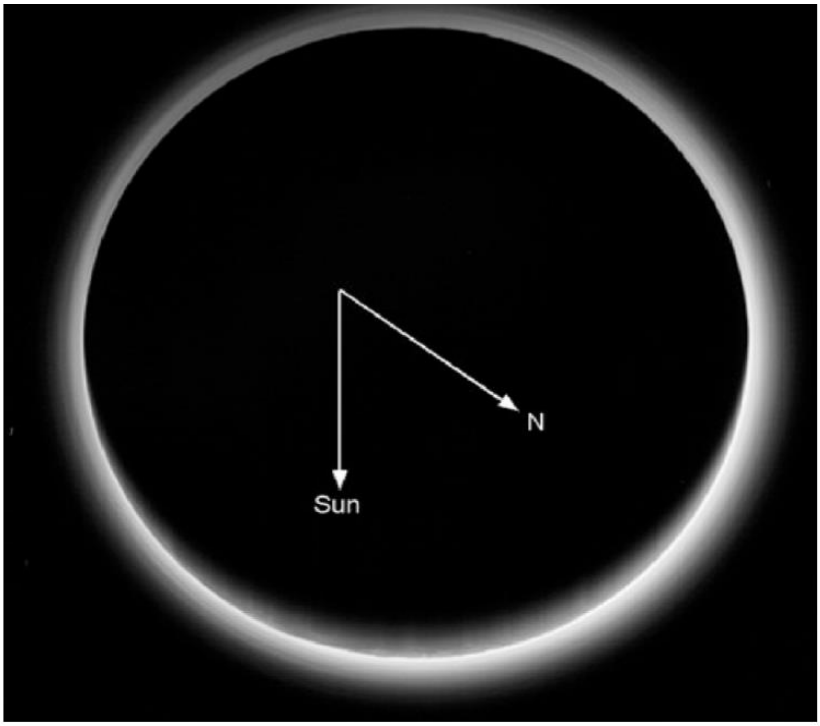

Figure 15: LORRI image showing brighter, more extensive haze over the northern Latitudes (Cheng *et al*. 2017).

Observations of the haze extend over large phase angles between 20-169°. Observed I/F increases with increasing phase angles, implying larger particles exhibiting a large forward scattering lobe. Both conditions can be satisfied if the high-altitude haze is composed of 10 nm particles, from which larger aggregates grow rapidly toward lower

altitudes. These aggregates (with radii around 0.2 μm.) would then be Mie scatterers in the visible band of LORRI and MVIC (Gladstone *et al.* 2016; Cheng *et al*. 2017).

At least 20 distinct bright, thin embedded layers have been observed as well. The most prominent layers are located at around 10, 30, 90, and 190 km altitudes and traceable up to 1000 km in the horizontal. The lowest haze layer is around 3-5 km altitude, with a width varying from 1-3 km, although this is barely resolved in the images. This layer is observed to go from 5 km altitude to nearly the surface over 600 km in the horizontal. Although the haze is brightest over northern Latitudes, the layers appear more numerous and distinct over equatorial regions of the limb.

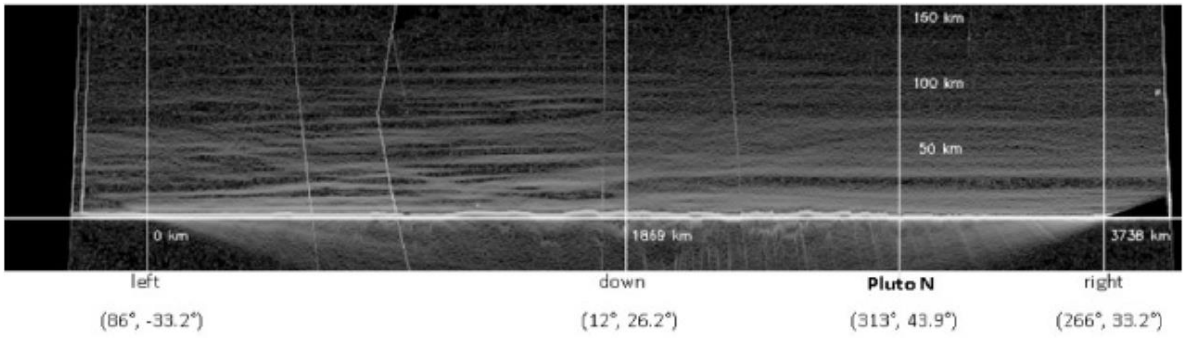

Figure 16: Unwrapped composite LORRI image showing haze layers across the limb of Pluto. Many structures become apparent, including more defined layers in equatorial and low-latitude regions and a dark lane above northern latitudes (Cheng *et al.* 2017).

This can be seen in Figure 16, where more distinct layers are seen on the left side of the unwrapped image corresponding to the equatorial and low-latitude regions. Also visible are two dark lanes, one around 30 km and the other around 72 km. Although persistent

over large horizontal distances, the layers do merge, break, and tilt (Gladstone *et al*. 2016, Cheng *et al*. 2017). Of specific interest are the regions and amounts of tilting in certain layers, as this can help constraint certain atmospheric processes/dynamics.

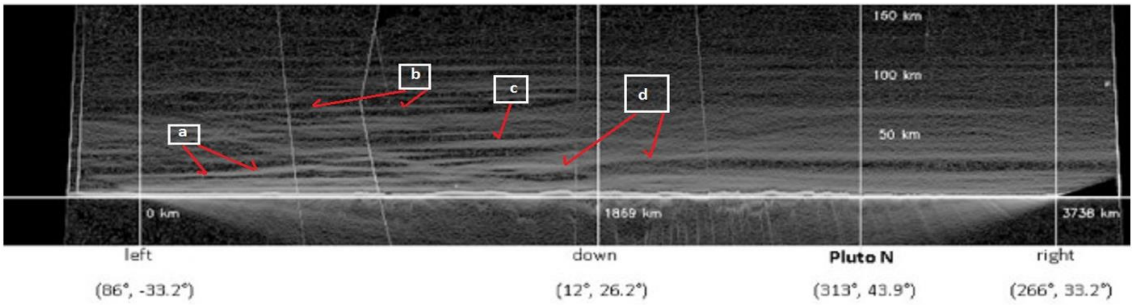

Figure 17: Layers exhibiting considerable tilt relative to the limb are labeled (a)-(d) (Cheng *et al*. 2017).

Several layers and dark lanes with considerable tilt and of specific interest due to their Latitude location are labeled in Figure 17. Layers (a)-(c) are seen to tilt down from right to left, and dark lane (d) is seen to dip abruptly down toward the surface from around 30 km. The consequences and information that can be extracted from layers like these will be discussed later.

Another goal in characterizing the layers was to quantify their temporal evolution using NH images/data. A search was done using three comparisons in the north with time intervals of 1.97, 3.46, and 5.43 hours. Another comparison was done for southern latitudes using a 2.61-hour interval. Over these comparisons, changes were seen in I/F but not in the layer positions. Haze scale height changes were also seen above 100 km. The I/F changes of around 30% are not believed to be physical but are due to the forward

scattering lobe of the phase function with increasing phase angle along New Horizons trajectory with time. The scale height change could be physical. Overall, considerable evolution in the haze is not seen over the 2-5-hour intervals. The background haze and haze layers appear to be very stable, with relatively long lifetimes (Cheng *et al*. 2017).

1.2.4 Pluto vs. Titan

Pluto's haze occurs within the same pressure regime as Titan's detached haze layer—indicated in Figure 11. Also note the difference in temperature for the haze regions. Even so, the dominant atmospheric compositions of N_2 and CH_4 creates similar, to almost identical, photochemical pathways and products. Once generated, these products undergo nucleation and growth to create aerosols. The formation of Titan's detached haze layer by condensation is ruled out due to its high temperature/sub-saturation conditions (Lavvas *et al.* 2009). This is also believed to be the case for Pluto below 200 km due to a methane heated stratosphere producing high temperatures and thus sub-saturation of all major hydrocarbons.

However, condensation may still play a key role for Pluto above 200 km altitude where the temperature drops enough for certain species (other than hydrocarbons) like HCN to be supersaturated and nucleate and/or condense (Cheng *et al*. 2017). The ionosphere of Pluto is thought to behave like Titan's for nucleation and aerosol growth (Lavvas *et al*. 2010). Titan's nuclei form in its ionosphere around 1000-1200 km altitude, near the peak electron density in the ionosphere. Low energy electrons attach to nitriles (like HCN and HC_3N), forming negative ions (CN^- and C_3N^-). Eventually, negatively

charged macromolecules attract positive ions and begin to form small haze particles. Although direct measurement by REX has not revealed an ionosphere, models suggest a peak electron density of ≤ 1300 cm^{-3} at around 700 km. REX's sensitivity may be above this density. The peak also occurs hundreds of kilometers above Pluto's observed haze as in Titan's atmosphere. This could lead to haze formation in the hottest part of Pluto's atmosphere—where hydrocarbons are greatly sub-saturated. It is the settling of these particles downward into supersaturated regions, which leads to condensation of hydrocarbons at lower altitudes.

The expected ionospheric chemistry occurs in the presence of hydrocarbons on Titan and Pluto, but not on Triton. This is another strong reason for the Pluto—Titan analog more so than Pluto—Triton. Where the diffusional growth transitions to growth by coagulation is still not completely understood. It is known that the detached layer occurs within the vicinity of this transition (Lavvas *et al*. 2010; Cheng *et al*. 2017). Since many properties of Titan's haze are better established, due to more extensive observations spatially and temporally, additional characteristics of Titan's haze will be outlined here for later comparison (Lavvas *et al.* 2010; Cheng *et al.* 2017).

Titan's detached haze layer has been characterized through Cassini/Huygens observations (Lavvas *et al*. 2010). The layer is composed of 40 nm average size particles, with a number density of 30 particles cm^{-3}. The detached layer is in Titan's mesosphere, at around 520 km altitude. It coincides with a temperature maximum that is believed to be in part due to absorption of solar radiation by the haze. Using aerosol microphysics

models, Titan's implied vertical mass flux of photochemical products is 2.7-4.6 × 10^{-14} $gcm^{-2}s^{-1}$ (Lavvas *et al*. 2009).

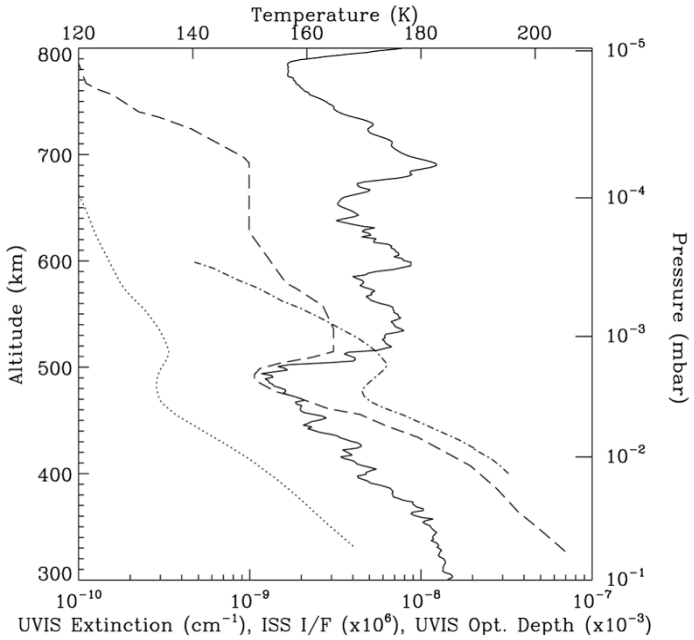

Figure 18: Observations of the LOS extinction (long-dashed line), I/F (dash-dotted line), and vertical temperature structure (solid line), and opacity calculated from the extinction profile (dotted line) of Titan's detached haze layer region obtained by Cassini/Huygens (Lavvas *et al*. 2010).

Observations gathered by three Cassini/Huygens instruments are shown in Figure 18, taken from Lavvas *et al*. (2009). The observations were made in July 2004, at 10° S latitude, within the region where the detached haze layer is most distinct (Low-mid latitudes.). The ISS (I/F at 338 nm, dash-dotted.) and UVIS (retrieved extinction profile at 187.5 nm, long-dashed line.) data both show the detached haze layer around 500 km altitude. The UVIS extinction profile also shows a near co-location with a local

temperature maximum in the HASI vertical temperature profile (solid line). Observations from Pioneer 11 and Voyager 1 photometry and polarimetry have led to disagreements in the deduced particle sizes of Titan's haze. Polarimetric data from both show large single-scattering polarization near 90 degrees phase angle—indicating small particles with radii around 0.1 μm. However, photometric data at high phase angles (130-160 degrees) from Voyager 1 require the existence of larger particles ranging from 0.2-0.5 μm. Both can be true if aggregates are growing at the expense of smaller monomers.

Microphysics models for Titan show that the extinction profiles can be reproduced if, first the compact monomers are formed at high altitude (just above visible haze layer) from elementary photochemical particles. The interactions of these original particles/nuclei can be described by a classical liquid drop model. Once these particles begin to settle, they will undergo coagulation, becoming fractal aggregates. This transition is the dominant physical process responsible for a transition from fractal dimension of 3 (spherical) to 2 (aggregate). Some details of this fractal growth are covered in Section 2.7. Once the aggregates fall further into regions where hydrocarbons and/or additional species are at supersaturation, they undergo particle rounding and a transition back to fractal dimension of 3 (Cabane *et al.* 1993).

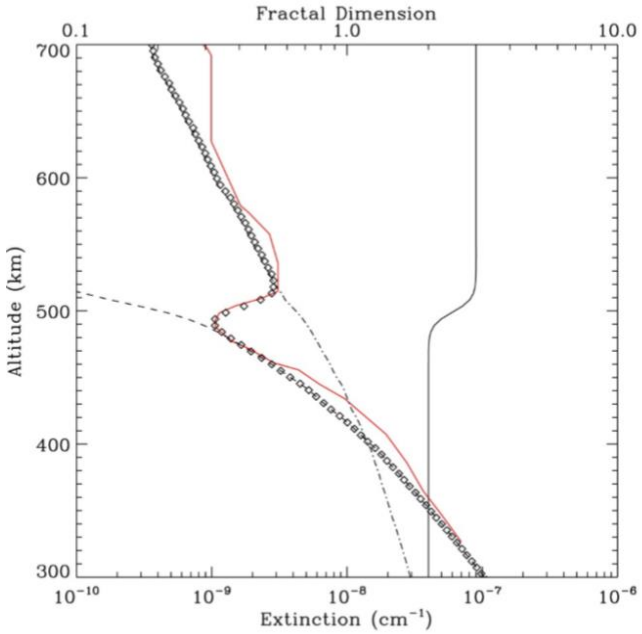

Figure 19: The evolution of fractal dimension (with altitude) is plotted along with the extinction profile of Titan's detached haze layer. A similar evolution of fractal dimension is believed to occur for Pluto's haze (Lavvas *et al*. 2010).

A plot of this fractal dimension transition, as well as the extinction profile that is produced, is shown in Figure 19 (taken from Lavvas *et al*. 2009). The transition is seen to occur just above 500 km altitude (solid line). Also shown are the contributions from fractal (dashed) and spherical (dash-dotted) particles to the total extinction (diamonds), along with the observed extinction profile (red line).

A thermospheric origin for the aerosols in Titan's atmosphere is supported by observations of large positive and negative ions by CAPS/ELS and CAPS/IBS, respectively (Lavvas *et al*. 2011). The origin of heavy ions is likely not due to a single chemical process, since spectra show a continuous and diverse population of masses. Certain pathways are currently being modeled with the goal of confirming the products.

One such pathway is the growth of polycyclic aromatic compounds (PACs) due to the large observed abundance of benzene. These PACs then form primary particles which undergo coagulation to produce aggregates. Particle rounding is also of interest at the PAC level. A visualization of the different stages/processes of particle growth that occur in both Titan and Pluto's atmosphere are shown in Figure 20 (Lavvas *et al*. 2011).

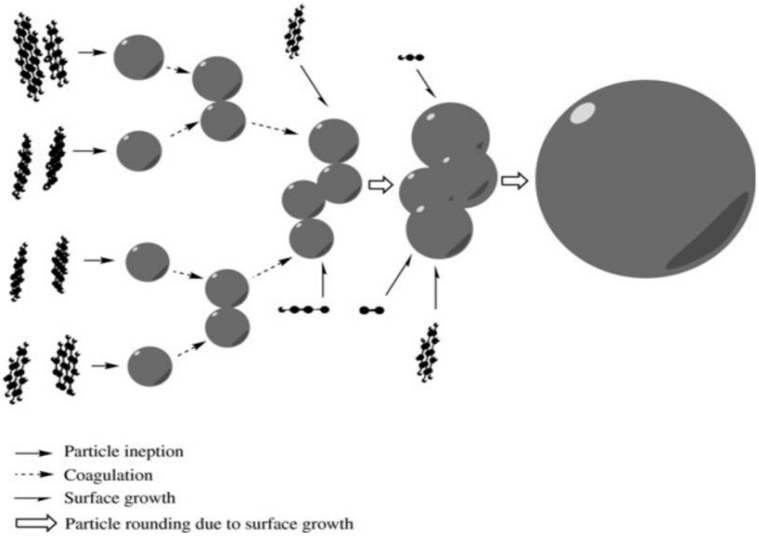

Figure 20: A schematic illustrating the processes leading to both fractals and particle rounding—applicable to Titan and Pluto (Lavvas *et al*. 2011).

1.2.5 Haze Nucleation

Possible nucleation processes for Titan and Pluto's atmospheres are constrained by a comparison of the nucleation rate to the particle production rate (inferred to be around 1 $cm^{-2}s^{-1}$ from the observed haze characteristics; Gladstone *et al*. 2016). Models

of particle lofting from horizontal winds, assuming low surface cohesion, can get enough particles in the air but cannot get them above a very shallow boundary layer observed in Pluto's ingress temperature inversion profile above Sputnik Planitia (SP). This would be sufficient for low altitude fog but not for upper atmospheric haze nucleation (Gladstone *et al*. 2016, Cheng *et al*. 2017). Therefore, the production of condensation nuclei from solar EUV and cosmic ray ionization is more likely. The total peak EUV ionization rate below 1000 km altitude is ~ 2×10^{-4} $cm^{-3}s^{-1}$, and peak electron density there of 14 cm^{-3}. It can be shown that if just a small fraction of the ionization products act as condensation nuclei, then enough nucleation occurs to support the deduced particle production rate (Summers *et al*. 1997; Krasnopolsky and Cruikshank, 1999; Cheng *et al*. 2017).

Another possible source of nucleation is the ablation products from incoming dust particles—specifically water. If cosmic dust particles are composed of pure water, then a downward transport of around 1×10^5 $cm^{-2}s^{-1}$ would occur if ablation occurs in the upper atmosphere. However, it is uncertain if all ablation would occur above 800 km in Pluto's atmosphere—where nucleation is believed to occur and form primary particles that coagulate upon settling (Cheng *et al*. 2017). If nuclei can form above or around 800 km, the temperature may be low enough for some species like HCN to condense and form large enough primary particles to undergo coagulation at rates that will sustain the haze production in the warm stratosphere.

After the study of (Wong *et al*. 2017), it seems that condensation of certain hydrocarbons on nuclei could peak between 200-400 km. Therefore, a formation mechanism for condensation nuclei is needed which will produce enough nuclei in the

region. An example of this nucleation source has been suggested by Lavvas *et al*. (2011) for Titan. Three regions are defined: Region 1 (1000-650 km)—PAC growth and deposition; Region 2 (650-500 km)—Particle Aggregation; Region 3 (below 500 km)—Surface Chemistry. Region 1 is where nucleation occurs by benzene molecules reacting with other radicals to form PACs—reaching around 40 atoms in size by 520 km altitude. Because of the small collision cross section and sticking efficiency, a small fraction of the PACs would go on to form primary particles, but with enough concentrations of condensing molecules and ions that could explain observed haze extinction (Lavvas *et al*. 2011). Whether Pluto's condensation nuclei are heavy negative macromolecules that attract positive ions, PACs, or water molecules is uncertain and is an area of active research.

1.2.6 Haze Sedimentation Timescale

Pluto’s atmosphere, although extensive (Several radii to exobase), is very tenuous. An object falling in this atmosphere will experience a drag force described and characterized by the Stoke’s regime. This is the regime for which the atmospheric mean free path is large when compared to the particle radius. The sedimentation velocity is then defined as the velocity the falling particle will have in equilibrium—when a balance between gravity and drag has occurred—also known as the terminal velocity. The drag on a spherical particle can be easily obtained, however several adjustment factors need to be taken into account for slipping and porosity if the particle is non-spherical or fractal in nature. A particle with porosity will have a decrease in drag, leading to an increase in

sedimentation velocity (Pruppacher and Klett 1997, Seinfeld and Pandis 2006, Lavvas *et al.* 2010). The correction has a complex altitude dependence and was taken from the Lavvas *et al*. (2010) study on fractals in Titan's atmosphere. Examples of sedimentation velocities for fractal aggregates falling in Pluto's atmosphere are shown in Figure 21. Several particle sizes within the altitude range where most of the haze and embedded layers were observed are shown with different colors. A comparison between sedimentation velocities calculated by Gao *et al.* (2016) (dash-dotted lines) and velocities using the Lavvas et al. (2010) correction factors with KINETICS model atmospheric inputs (solid lines) is also shown.

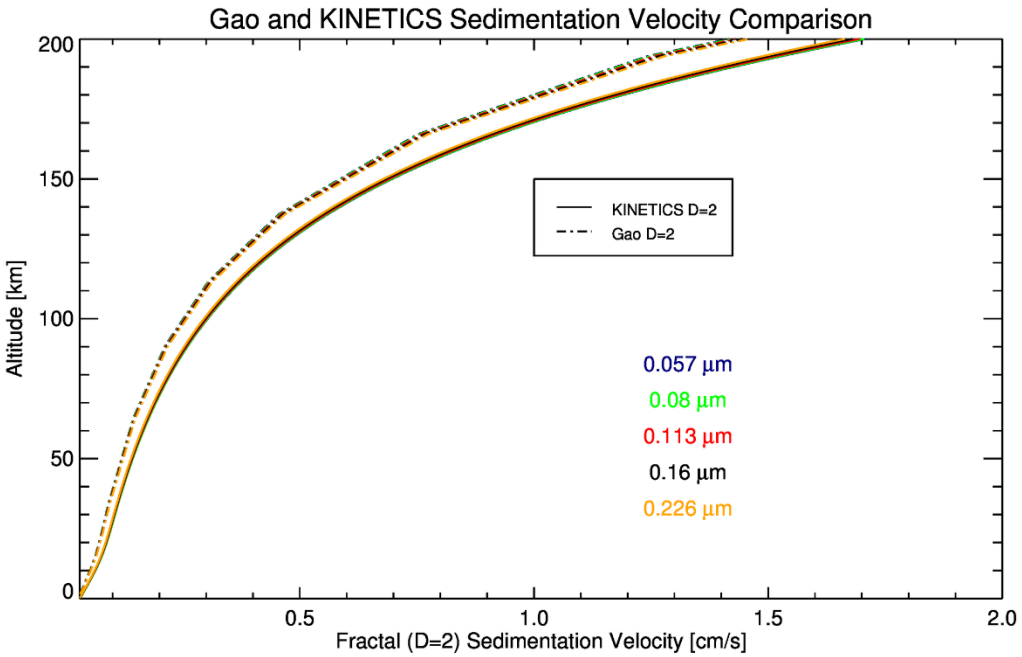

Figure 21: A comparison of sedimentation velocities for and fractal aggregated of different sizes calculated using two different models. The majority of haze layers reside in this altitude range (0-200 km).

The sedimentation velocity can be used to construct a sedimentation timescale—which is simply the time it would take for a given particle under certain atmospheric conditions to traverse a given distance. Two distances were defined and used in this study—atmospheric scale height and average haze layer separation distance (~ 10.5 km). The range in timescale to traverse the average separation distance for this altitude range is ~ 10^6 – 10^7 s. Another representation of the time it takes for the same range of particle sizes to fall from ~ 200 km and reach the surface is shown in Figure 22, this time for both spheres and fractals.

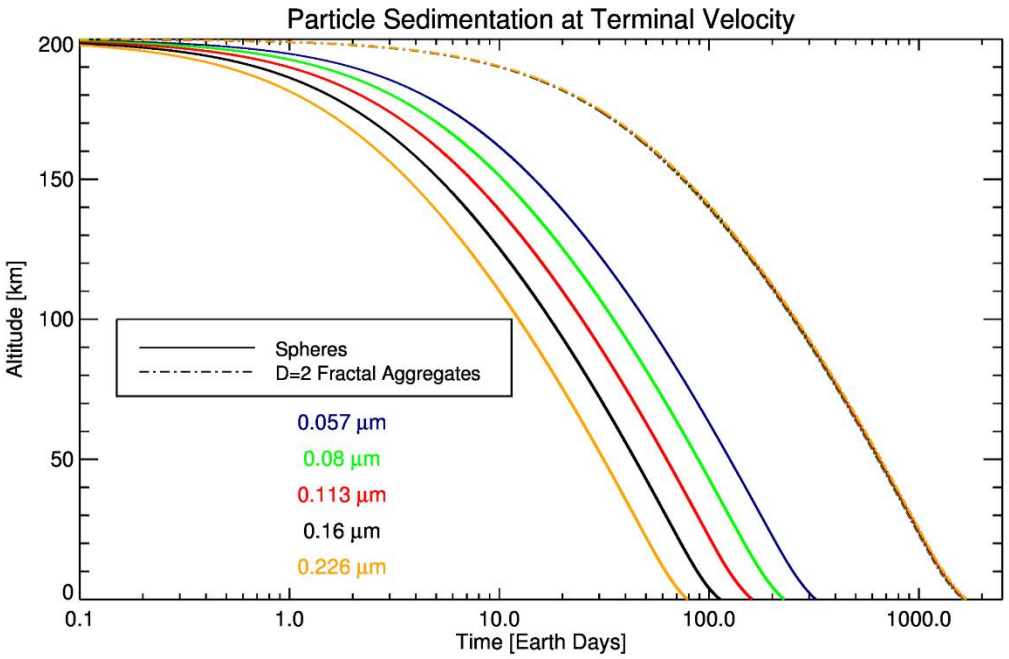

Figure 22: Haze sedimentation of spherical and fractal particles starting at 200 km altitude is plotted for several particles size.

1.2.7 Haze Growth Timescales: Diffusion and Coagulation

Once nucleation occurs, haze particles may grow through diffusion or coagulation. Again, looking to Titan's detached haze layer, haze particles are thought to grow initially through diffusion/condensation to reach monomer size (Around 10 nm for Pluto, Gladstone *et al*. 2016), where coagulation into larger, fractal aggregates is believed to take over as the dominant process. The details of these processes and exactly where each dominates, as well as the transition region, is still an active area of research. What is known is that haze exists above supersaturation conditions for Pluto, in a warmer region where homogenous kinetic diffusional growth should not occur. The concentration profile for one of the most abundant hydrocarbons (C_2H_2) observed and modeled (KINETICS output profile), as well as several particle saturation profiles, is shown in the left panel of Figure 23. The particle supersaturation profiles overlap. In the right panel, a homogeneous diffusional growth/sublimation timescale is shown for both continuum and kinetic regimes.

These regimes designate how the particle "sees" surrounding constituents undergoing diffusion—as either a fluid or kinetic/statistical bombardment. Pluto's atmosphere is in the kinetic regime, where the mean free path is much larger than the particles size. The timescale is defined as the time to take a given particle to either double in size or decrease to half its original size through condensation or sublimation. The condensation discussed there is for heterogeneous nucleation around 200 km, and is a way around subsaturation conditions that involves interaction of multiple molecules and

sticking efficiencies. Figure 23 shows why condensation has to be heterogeneous at high altitudes, as well as shows a viable mechanism for growth of particles in haze close to the surface where supersaturation does exist.

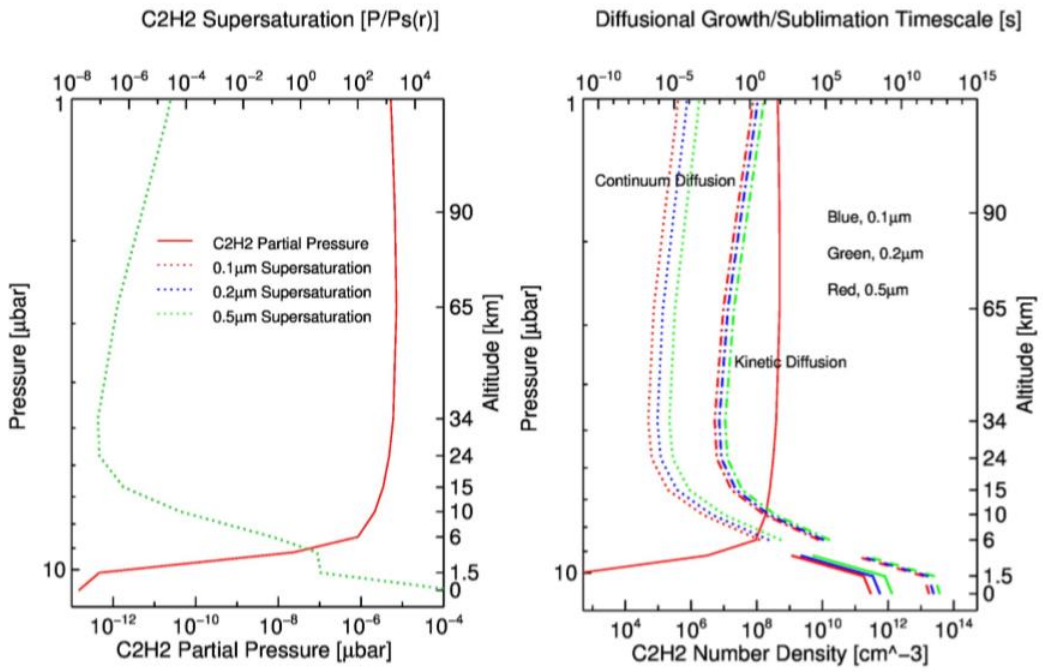

Figure 23: Atmospheric conditions from the KINETICS model output are shown in the left panel. In the right panel, diffusion timescales are shown for both the continuum and kinetic regimes. Supersaturation and growth only occur near the surface and above 200 km.

Another growth mechanism is coagulation. Coagulation is initiated by any process which leads to collision and sticking of particles. The two dominant coagulation mechanisms in Pluto's atmosphere are gravitational and Brownian. Gravitational coagulation occurs due to a difference in sedimentation velocity between particles in the same volume. The faster particle sweeps out a volume containing the slower particles. Brownian coagulation

occurs due to the thermal motion of the particles relative to each other. A coagulation timescale was defined as the time for a primary particle to double its radius due to collisions with a background population of monomers. These two coagulation timescales are shown for spheres in Figure 24. Several primary particle sizes are shown, with gravitational coagulation (solid) taking over as a faster growth process when compared to Brownian coagulation (dashed) at higher altitudes for larger particles.

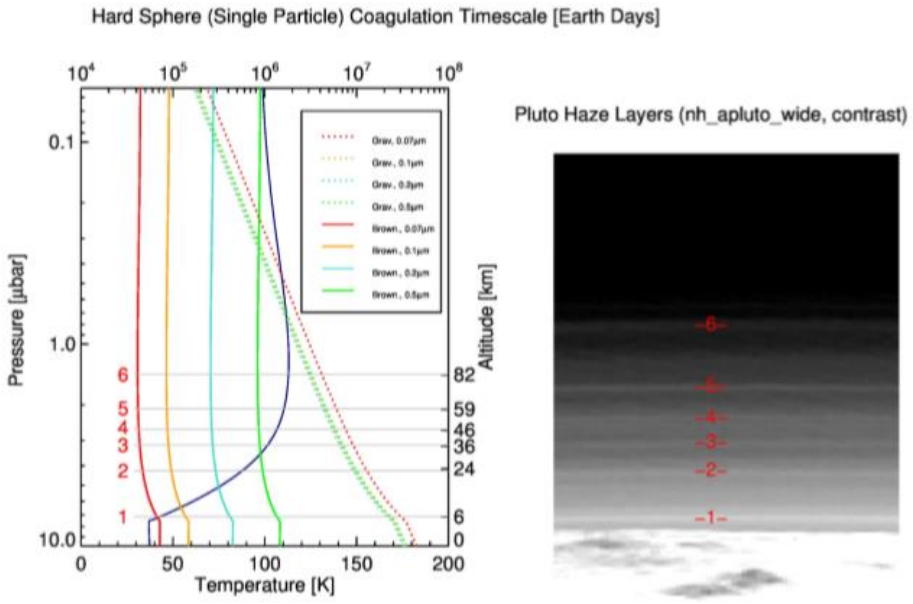

Figure 24: Coagulation timescales due to Brownian motion and gravitation settling. This timescale is defined as the time for a primary particle to reach double its original size. The particle is assumed to be in constant atmospheric conditions with a constant concentration of monomers.

1.3 Atmospheric Dynamics: Several Possible Wave Types in Pluto's Atmosphere

1.3.1 Internal Gravity (Buoyancy) Waves

Given a forcing mechanism, air parcels in the atmosphere can be displaced from equilibrium and undergo oscillations. The nature of these oscillations is dictated by the amount and type of atmospheric stability. If flow is both gravitationally and inertially stable, then parcel displacements are resisted by both rotation and buoyancy from their respective associated restoring forces. When both forces are important the waves generated are of the inertia-gravity wave type. The Boussinesq form of the linearized dynamical equations including rotation on the beta-plane are (Holton 2004)

Equation 23

$$\frac{\partial u'}{\partial t} - fv' + \frac{1}{\rho_0}\frac{\partial p'}{\partial x} = 0$$

$$\frac{\partial v'}{\partial t} + fu' + \frac{1}{\rho_0}\frac{\partial p'}{\partial y} = 0$$

$$\frac{1}{\rho_0}\frac{\partial p'}{\partial z} - \frac{\theta'}{\bar{\theta}}g = 0$$

$$\frac{\partial u'}{\partial x} + \frac{\partial v'}{\partial y} + \frac{\partial w'}{\partial z} = 0$$

$$\frac{\partial \theta'}{\partial t} + w' \frac{d\bar{\theta}}{dz} = 0.$$

The first two equations in this set are the horizontal momentum equations with the perturbed zonal (u') and meridional (v') winds, as well as the Coriolis parameter (f) and the constant mean density (ρ_0). The third of this set is the vertical momentum equation assuming hydrostatic balance, containing the perturbed pressure (p'), perturbed and mean state potential temperatures (θ' and $\bar{\theta}$), and gravity (g). The fourth equation is the continuity equation with the Boussinesq approximation. Here the atmospheric density can be treated as constant outside of the buoyancy term in the vertical momentum equation. The atmosphere is often stated to be incompressible with only local perturbations in density amongst a constant background density. This approximation is likely valid for Pluto because the vertical scales of wave motions (~ 20-40 km) associated with observed haze layer vertical separation distances remain less than the atmospheric scale height (H ~ 50 km for a large portion of the atmospheric column where layers are observed). Another interpretation of this approximation is that by assuming incompressibility one is taking the speed of sound in the atmosphere to be much greater than the speed of internal gravity waves (essentially filtering out physics of sound waves in equations of motion). With a wavelength of 20 km and temperature of 100 K the period of a sound wave in Pluto's atmosphere would be ~ 10^2 s, which predominantly remains at least an order of magnitude less than the buoyancy oscillation periods in Pluto's atmosphere (Sutherland

2010). The last of this equation set is then the thermodynamic energy equation, which contains the vertical velocity perturbation (w').

If the third of this equation set is used to eliminate θ' in the fifth then,

Equation 24

$$\frac{\partial}{\partial t}\left(\frac{1}{\rho_0}\frac{\partial p'}{\partial z}\right) + N_B^2 w' = 0.$$

One can assume sinusoidal solutions that are functions of the zonal (k), meridional (l), and vertical wavenumbers (m), as well as the wave frequency (ω), and of the form

Equation 25

$$u' = Re[\hat{\mathrm{u}}\, exp\, i(kx + ly + mz - \omega t)]$$

$$v' = Re[\hat{\mathrm{v}}\, exp\, i(kx + ly + mz - \omega t)]$$

$$w' = Re[\hat{\mathrm{w}}\, exp\, i(kx + ly + mz - \omega t)]$$

$$\frac{p'}{\rho_0} = Re[\hat{\mathrm{p}}\, exp\, i(kx + ly + mz - \omega t)].$$

Substituting these perturbations into the first and second of Equation 23 and in Equation 24, the resulting set of equations is

Equation 26

$$\hat{\mathrm{u}} = (\omega^2 - f^2)^{-1}(\omega k + ilf)\,\hat{\mathrm{p}}$$

$$\hat{v} = (\omega^2 - f^2)^{-1}(\omega l - ilf)\,\hat{p}$$

$$\hat{w} = (\omega^2 - f^2)^{-1}(\omega k + ilf)\,\hat{p}.$$

If this set is combined with the fourth of Equation 23, the dispersion relation becomes

Equation 27

$$m^2\omega^3 - [N_B^2(k^2 + l^2) + f^2m^2]\omega = 0.$$

Two roots exist—$\omega = 0$ is the case for stationary Rossby waves. Inertia-gravity waves are represented by $\omega \neq 0$, and have a dispersion relation of the form

Equation 28

$$\omega^2 = f^2 + N_B^2(k^2 + l^2)m^{-2}.$$

The vertical scale of these waves was assumed to be much smaller than the horizontal scale ($k^2 \ll m^2$). If a coordinate system is chosen so that $l = 0$, then the dispersion relation is of the form

Equation 29

$$\omega^2 = \frac{N_B^2k^2 + f^2m^2}{k^2 + m^2},$$

found in Hubbard *et al*. (2009) and McCarthy *et al*. (2008). Here the more general case of comparable horizontal and vertical scales of the waves are considered ($k^2 \neq 0$ in the denominator). For vertical propagation (m real), the condition of $|f| < |\omega| \ll N$ must hold for the wave frequency. If rotation is slow (as it is on Pluto), or if $\omega \gg f$ and the waves are of sufficiently small scale ($\lambda_z \sim 10\ km,\ \lambda_x \sim 100\ km$), then $f \to 0$ and purely internal gravity waves can be approximated. The slope of phase lines is defined by the ratio of vertical to horizontal group velocity, and for purely internal gravity waves using Equation 29 is

Equation 30

$$s \equiv layer\ slope \equiv \left|\frac{c_{gz}}{c_{gx}}\right| = \left|\frac{k}{m}\right| = \frac{\lambda_z}{\lambda_x} = \left[\frac{{N_B}^2}{\omega^2} - 1\right]^{-\frac{1}{2}}.$$

This slope can also be represented by an angle relative to vertical (α), $\cos^2 \alpha = \lambda_z/(\lambda_z^2 + \lambda_x^2)^{1/2}$. In the regime where $k^2 \ll m^2$ and when rotation is still not important the slope can simply be represented by $k/m \approx \omega/N_B$. For inertia-gravity waves where rotation is important (usually when $k^2 \ll m^2$), the slope is reduced by f as

Equation 31

$$s = \frac{(\omega^2 - f^2)^{1/2}}{N_B}.$$

For rotation to be important, Holton (2004) states that the order of magnitude of the ratio between the buoyancy frequency and Coriolis parameter must be $N_B^2/f^2 \leq 10^4$. This holds true for Pluto, where the Buoyancy frequency is ~ 10^{-3} and the Coriolis parameter around 30° N is ~ 10^{-5}. For rotation to affect the slopes and wave propagation considerably, the scale of the waves must be large. Slopes will not be altered by f for waves with vertical and horizontal wavelengths on the order of $\lambda_z \sim 10\ km$, $\lambda_x \sim 100\ km$. However, as will be covered in Chapter 3, observations exist of haze layers whose vertical wavelengths approach 20-30 km and who's horizontal wavelengths inferred from slopes and tracking of layers around the limb approach 1000 km. The location and horizontal dimensions of Sputnik Planitia certainly provide the opportunity for larger scale waves that can be altered even by Pluto's slow rotation.

A pair of studies, Hubbard *et al*. (2009) and McCarthy *et al*. (2008), analyzed fluctuations in stellar flux pre-NH flyby of the Pluto system with the occultation of star P445.3 by Pluto on March 18th, 2007 using the inertia-gravity wave interpretation and dispersion relation discussed above. They adopted the values for scale height, horizontal wavenumber, Coriolis parameter, and buoyancy frequency of 60 km, $2\pi/1000$ km^{-1}, 2×10^{-5} s^{-1}, and 1.44×10^{-3} s^{-1}, respectively. They extracted power spectra of *m* for the altitude ranges of 165-215 km, 215-265 km, and 265-315 km. The dominant peaks in power spectra occurred at vertical wavelengths of ~ 8 km and 18 km. The power spectra are shown in Figure 25 for the three altitude ranges.

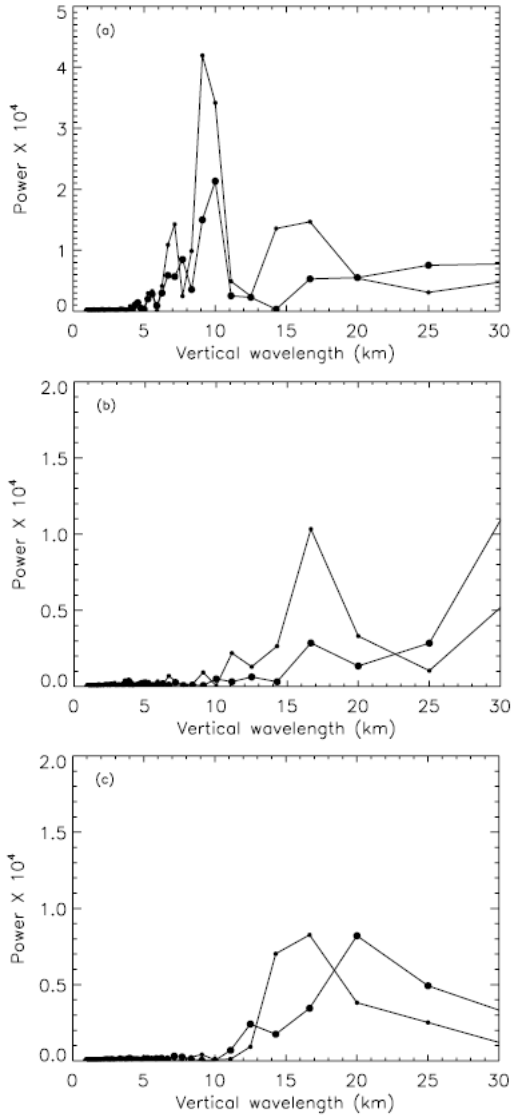

Figure 25: Power spectra extracted for altitude ranges of (a) 165-215 km, (b) 215-265 km, and (c) 265-315 km. Figure 3 in McCarthy *et al*. (2008).

In addition, McCarthy *et al*. (2008) analyzed the amplitudes of observed perturbations in the context of nearly breaking or saturated gravity waves. The ratio between background relative pressure and mass density perturbations can be shown to be related to the vertical wavenumber by

Equation 32

$$\frac{(P'/\bar{P})}{(\rho'/\rho_0)} = -\frac{1}{Hm}.$$

The background atmosphere is assumed to be isothermal with a constant scale height. For an ideal gas, the background relative temperature perturbations are related by

Equation 33

$$\frac{T'}{\bar{T}} = \frac{P'}{\bar{P}} - \frac{\rho'}{\bar{\rho}} = \frac{P'}{\bar{P}}(1 + Hm)\,.$$

If a gravity wave with vertical wavenumber *m* breaks when

Equation 34

$$|\nabla| \equiv \frac{d\ lnT}{d\ lnP} > \frac{(\gamma - 1)}{\gamma},$$

then the background relative density perturbation for which a wave will break or become saturated can be expressed as

Equation 35

$$(\rho'/\bar{\rho}) \approx \frac{(\gamma - 1)}{\gamma}\frac{1}{Hm}.$$

McCarthy *et al*. (2008) found that for vertical wavelengths of 8 km and 20 km, density perturbation amplitudes relative to background would be saturated at 0.006 and 0.015, respectively. They found inferred density fluctuations in their data that are close to these values. Observations for lower altitudes will be compared to these values in Chapter 3.

In Hubbard *et al*. (2009), the observed power spectrum was compared to several theoretical spectra to further inspect for the signature of variations with the gravity wave interpretation. As shown in Figure 26, the observed spectrum falls well within a saturated gravity wave spectrum produced by Smith *et al*. (1987). Turbulence was ruled out at producing the observed spectrum (on the Kolmogorov scale).

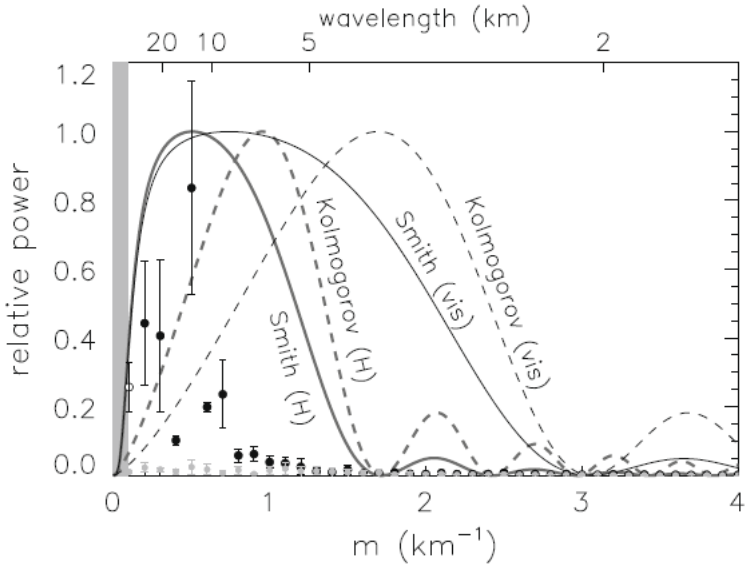

Figure 26: Theoretical spectra and observed power spectra data points. Figure 4 in Hubbard *et al*. (2009).

1.3.2 Orographically Driven Gravity Waves on Pluto

Atmospheric gravity waves can be generated by flow over topography, forcing parcel oscillations. These oscillations can then propagate both vertically and horizontally.

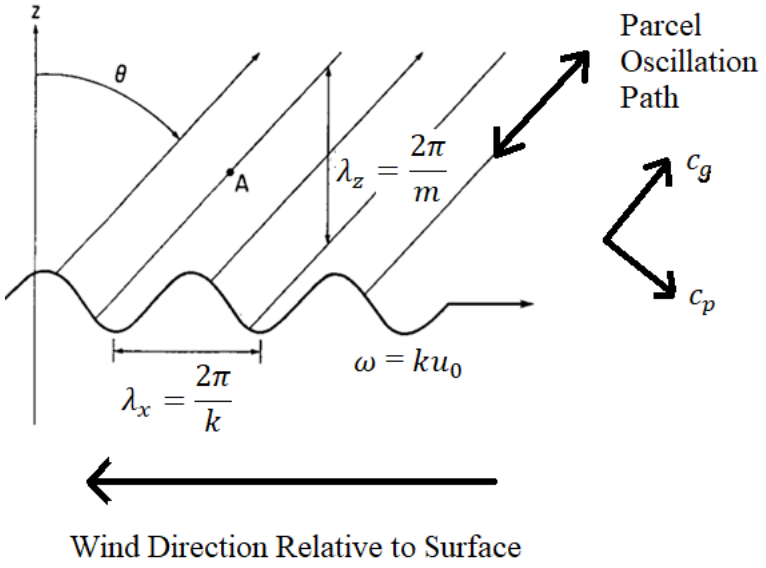

Figure 27: Adapted from Lindzen (1990) for the heuristic treatment of gravity wave parcel oscillations due to either flow over a stationary surface corrugation or a corrugation being pulled through the atmosphere. Tilted lines of constant phase are shown, along which pressure-temperature-density perturbations occur to possibly produce clouds or haze layers.

Flow of velocity u_0 over this type of topography was considered. The Taylor-Goldstein equation to describes this wave type and forcing mechanism (Nappo 2002). After applying the double Fourier transform (assuming wave like solutions in perturbation theory) to the linearized equations of motion as in section 1.3.1 and solving the perturbation equations for the vertical parcel velocity perturbation, this expression becomes

Equation 36

$$\frac{d^2w'}{dz^2} + m^2(z)w' = 0$$

$$m(z) = \left[\frac{{N_B}^2 - \omega^2}{\omega^2 - f^2}(k\delta)^2 - \frac{1}{4H^2} + \left(\frac{1}{H}\frac{du_0}{dz} + \frac{d^2u_0}{dz^2}\right)\frac{1}{c - u_0}\right]^{1/2}.$$

In the second expression of this equation set, c is the zonal phase speed and $\delta = [1 + (l/k)^2]^{1/2} \approx 1$, and is called the aspect ratio. For simplicity, the waves here are assumed to be standing waves (c = 0), generated by evenly spaced ridges with height h_0 represented by

Equation 37

$$w'(z = 0) = w_0 = u_0(z)\frac{\partial h}{\partial x}$$

$$h = h_0 \cos(kx)\,.$$

The dispersion relation and variables contained in the above equations are listed below for wind that quickly becomes constant with altitude

Equation 38

$$m(z) = \left[\frac{{N_B}^2 - \omega^2}{\omega^2 - f^2}(k\delta)^2 - \frac{1}{4H^2}\right]$$

$$N_B{}^2 = -\frac{g}{\rho_0}\frac{d\rho_0}{dz}$$

$$\omega = -ku_0 \, .$$

A solution to the Taylor-Goldstein equation can be approximated for the full expression of vertical wavenumber in Equation 36 if the vertical wavenumber is assumed to be slowly varying (or u_0 and N_B are slowly varying with altitude). This is called the WKB method/approximation named after Wentzel-Kramers-Brillouin and is commonly used for providing solutions to the wave equation for gravity waves (Nappo 2002). The solution here with forcing topography topography (lower boundary condition) is

Equation 39

$$w' = w_0 \left(\frac{\rho(0)}{\rho(z)}\right)^{1/2} \left(\frac{m(0)}{m(z)}\right)^{1/2} exp[i(kx + ly - ku_0)] exp\left[i \int_0^z m(z)dz\right].$$

One of the most notable influences of the zonal wind velocity u_0 is on the vertical wavelength of the gravity waves, which are, to zeroth order, defined to be

Equation 40

$$\lambda_z = \frac{2\pi u_0}{N_B \delta} \, .$$

The impact of gravity waves on the mean state that is believed to cause the layers that are seen in NH images is through the perturbations in atmospheric and haze particle number densities. The perturbation in haze particle number density $n'_H(x,z,t)$, is described by the linearized continuity equation

Equation 41

$$\frac{\partial n'_H(x,z,t)}{\partial t} + \frac{\partial [n_H(z)\, u'(x,z)]}{\partial x} + \frac{\partial [n_H(z) w'(x,z)]}{\partial z} = 0\,.$$

The perturbations in u' and w' come directly from gravity wave action on the atmospheric gas, whose perturbation linear continuity equation for the nitrogen atmosphere mass density, $\rho(z)$, is given as

Equation 42

$$\frac{\partial u'(x,z)}{\partial t} + \frac{\partial w'(x,z)}{\partial x} + \frac{w'(x,z)}{H} = 0; \quad \text{where } \frac{1}{\rho}\frac{d\rho}{dz} = -\frac{1}{H}.$$

The horizontal and vertical wave velocities are related through

Equation 43

$$u'(x,z) = \frac{m}{k} w'(x,z) + \frac{w'(x,z)}{ikH}\,.$$

Lastly, if the time derivative in Equation 41 is approximated by the period of one Pluto day ($2\pi/\Omega$), and also divided by the mean/background number density, $n_H(z)$, then the expression for background relative haze number density perturbations is

Equation 44

$$\frac{n_H'(x,z,t)}{n_H(z)} = -\frac{2\pi}{\Omega\, n_H(z)}\left[\frac{\partial[n_H(z)\, u'(x,z)]}{\partial x} + \frac{\partial[n_H(z) w'(x,z)]}{\partial z}\right].$$

One of the first solutions of this expression is plotted in Figure 28. Numerical solutions to the first order linearized continuity equation and perturbations were calculated and convergence occurred with a range between -1 and 1. At least 25 tilted layers that are parallel to constant phase lines are visible.

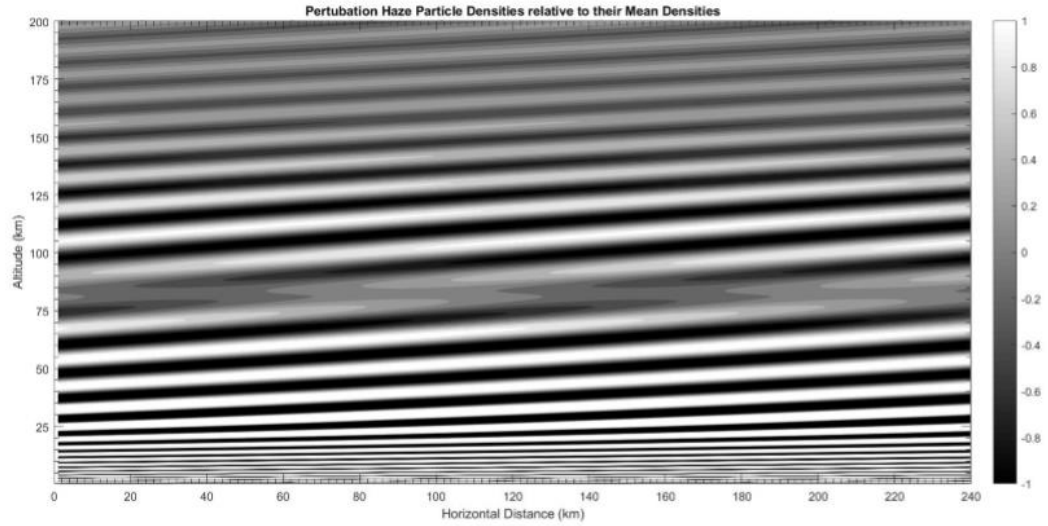

Figure 28: Haze particle density perturbations for the 2D gravity wave model. Light regions correspond to denser particles, dark regions to rarefied densities.

NH observations indicate a topographic relief around the basin informally known as Sputnik Planum (SP) of around 5 km, as well as semi-periodic ridges to the basins NE with a spacing on the order of 100 km (Gladstone *et al*. 2016, Schenk *et al*. 2018). The basin can be seen in the center of the synoptic map in Figure 29, and the semi-periodic ridges are the brighter region to the right.

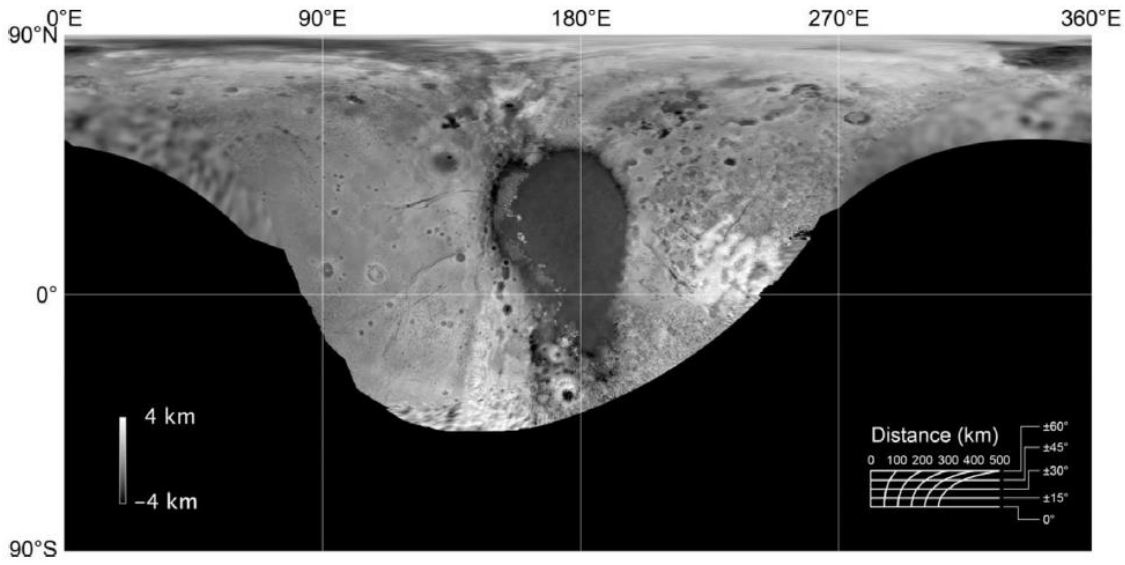

Figure 29: Global digital elevation model (DEM) of Pluto from Schenk *et al*. (2018). A large basin with abrupt changes in elevation is shown around SP, and semi-periodic ridges are shown to the basin's East—both large scale topographic features likely to interact with atmospheric flow and possibly generate atmospheric gravity waves.

A zoom in of the region with semi-periodic ridges is shown in Figure 30. The ridge spacing appears to be ~ 100 km with amplitudes/heights of 1.5-3 km. These values are reasonably close to the preferred values used in the orographic gravity wave model implemented in this dissertation.

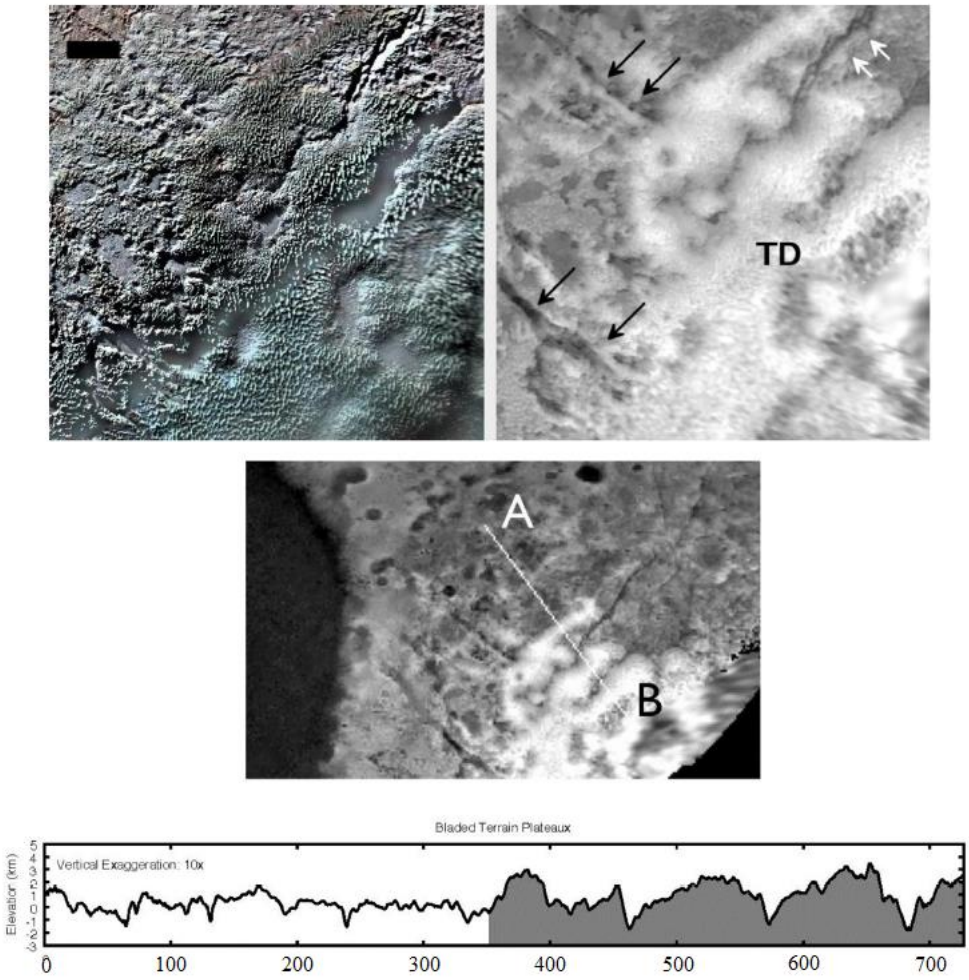

Figure 30: Best known resolved portions of Tartarus Dorsa (TD) also taken from Schenk *et al.* (2018) where semi-periodic ridges are present. An elevation profile was taken A-B and is shown at bottom. This profile shows approximately sinusoidal variations in elevation with an amplitude of at least 2-3 km.

When stationary waves are generated by flow over sinusoidal terrain in statically stable conditions (where the wind speed u, and N_B can vary with height), the differential equation governing the perturbed vertical velocity becomes

Equation 45

$$\left(\frac{\partial^2 w'}{\partial x^2} + \frac{\partial^2 w'}{\partial z^2}\right) + \varphi^2 w' = 0\,.$$

The ability for waves generated by topography to vertically propagate through the atmosphere (related to the scale of the topography and atmospheric conditions) is then dictated by the Scorer parameter, φ, which is defined by

Equation 46

$$\varphi^2 = \frac{{N_B}^2}{u^2} - \frac{1}{u}\frac{d^2 u}{dz^2}\,.$$

The condition for vertical propagation is then given by $k^2 < \varphi^2$. Profiles of the Scorer parameter are plotted in Figure 31, with vertical lines representing k^2 values with their associated horizontal wavelength/scale labeled.

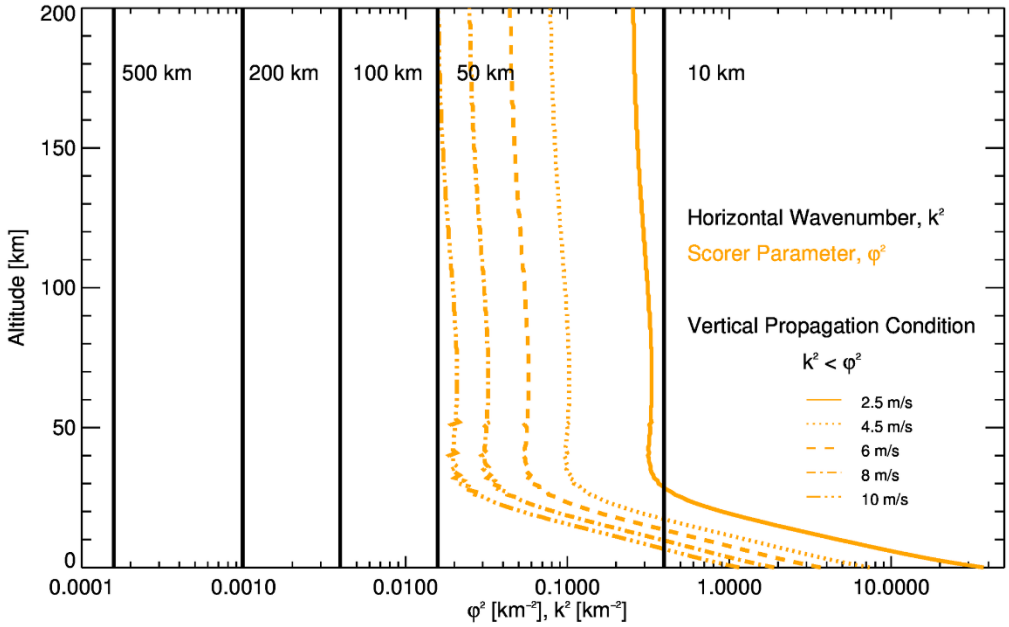

Figure 31: Comparison of Scorer parameter for several wind speed cases to several horizontal wavenumbers (wavelengths). Orographic gravity waves generated by ridges with horizontal scales less than 10 km will not propagate above ~ 30 km altitude for all wind cases. Topography with scales larger than 50 km can vertically propagate throughout the atmosphere for all wind cases.

1.3.3 Atmospheric Tides on Pluto

Atmospheric tides were first proposed by Toigo *et al*. (2010) to explain atmospheric density perturbations in stellar occultation data. Their model sought solutions to the forced tidal equations driven by a vertical velocity at the surface boundary from "breathing" (sublimation cycles) of ices induced by Pluto's diurnal cycle. This is the most likely driving mechanism for tides in Pluto's atmosphere, as the radiative time constant is large (estimated diurnal fractional response of ~ 2 x 10^{-3}, or 0.2 K; Strobel *et al*. 1996) making it unlikely for atmospheric oscillations to be generated

directly by day-night heating variations. Convection is also unlikely to be a main driver of tides as Pluto's atmosphere has a strong temperature inversion in the lowest scale height preventing the development of a substantial boundary layer (Toigo *et al*. 2010).

In the classical tidal model of Toigo *et al*. (2010), the driving mechanism can be represented as a vertical velocity function at the surface, $w_S(\lambda, \phi, t)$, defined by

Equation 47

$$w_S(\lambda, \phi, t) = [1 - A(\lambda, \phi)] \frac{F'(\lambda, \phi, t)}{\rho_S \, L} M(\lambda, \phi) \, .$$

The vertical velocity is a function of albedo A, diurnal thermal forcing F', and a frost map function M—which are in turn functions of latitude and longitude (λ, ϕ). The vertical velocity is also dependent on the atmospheric density at the surface ρ_S, and the latent heat of sublimation of N_2. Estimates of the vertical forcing velocity are ~ 2.7 cm/s, temperature perturbations of ~ 1.4 K and background relative pressure perturbations of ~ 10^{-2}.

Toigo *et al*. (2010) numerically solved the differential equation representing the vertical structure of the tides for a range of eigenvalues. The vertical structure equation can be derived from the linearized tidal equations for a thin atmosphere (Kato 1966a,b; Chapman and Lindzen 1970)

Equation 48

$$\frac{\partial u'}{\partial t} - 2\Omega v' \sin\phi = -\frac{1}{\rho_0 a \cos\phi}\frac{\partial P'}{\partial \lambda}$$

$$\frac{\partial v'}{\partial t} + 2\Omega u' \sin\phi = -\frac{1}{\rho_0 a}\frac{\partial P'}{\partial \phi}$$

$$\frac{\partial P'}{\partial z} = -g\rho'$$

$$\frac{\partial \rho'}{\partial t} + w'\frac{d\rho_0}{dz} + \rho_0 \chi' = 0$$

$$\frac{\partial P'}{\partial t} + w'\frac{dP_0}{dz} = \gamma g H_0 \left(\frac{\partial \rho'}{\partial t} + w'\frac{d\rho_0}{dz}\right).$$

Heating and friction are neglected in the above set of equations, and χ' is the divergence expressed as,

Equation 49

$$\chi' = \frac{1}{a\cos\phi}\left[\frac{\partial u'}{\partial \lambda} + \frac{\partial}{\partial \phi}(v'\cos\phi)\right] + \frac{\partial w'}{\partial z}$$

The influence of Pluto's strong temperature inversion and structure enter through P_0 and ρ_0, which are only functions of radial distance. This set of equations can be combined into one differential equation that can be solved with separation of variables into the vertical and horizontal differential equations. The separation constants become an infinite series of eigenvalues with corresponding eigenfunctions that represent different modes. Eigenvalues can be found by specifying a longitudinal wavenumber, s, and frequency of

oscillation of the forcing ($\sigma = \Omega$). The horizontal structure equation is solved for a series of eigenvalues, each corresponding to a Hough function. Hough functions are a sum over Legendre polynomials whose coefficients are functions of s, σ, and the eigenvalue. Each eigenvalue is also used to solve for an individual mode in the vertical structure equation (Toigo *et al*. 2010).

The method of solution by Toigo *et al*. (2010) was adopted from Kato (1966a,b), and wavelengths that best matched observations were found from the lowest horizontal structure modes (s = -1, 0). These two modes yielded vertical wavelengths 12 km and 7.7 km. The latitudinal structure and extent of temperature perturbations from their solution is shown in Figure 32.

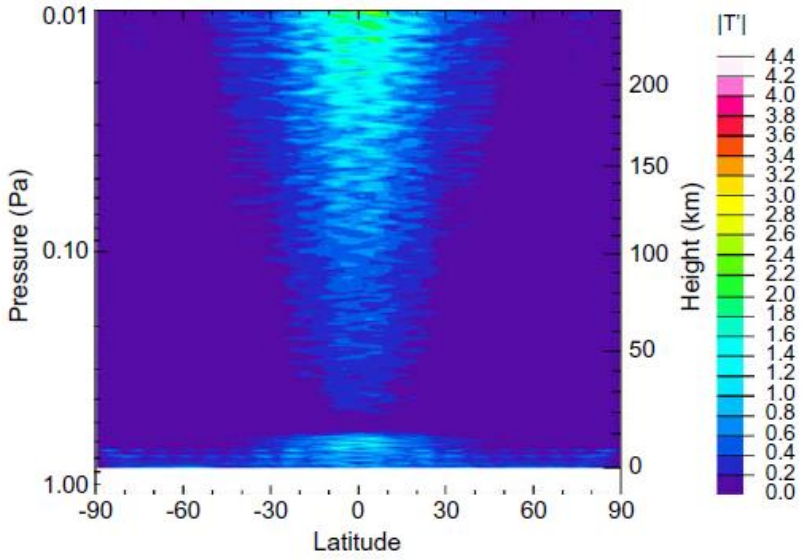

Figure 32: Amplitude of the sum of all diurnal gravity wave modes as a function of pressure and latitude. Perturbations are mainly confined to low latitudes. A "cross hatching" pattern of both positively and negatively sloped linear features is visible. There is also a considerable gap in perturbations between ~10-20 km, a likely result of the strong temperature inversion and maximum there. All these features are important to note for comparison to observed haze layers (Toigo *et al*. 2010).

Another comparison for results found in this dissertation are the resulting power spectra from the tidal model that were calculated by taking vertical profiles of Figure 32.

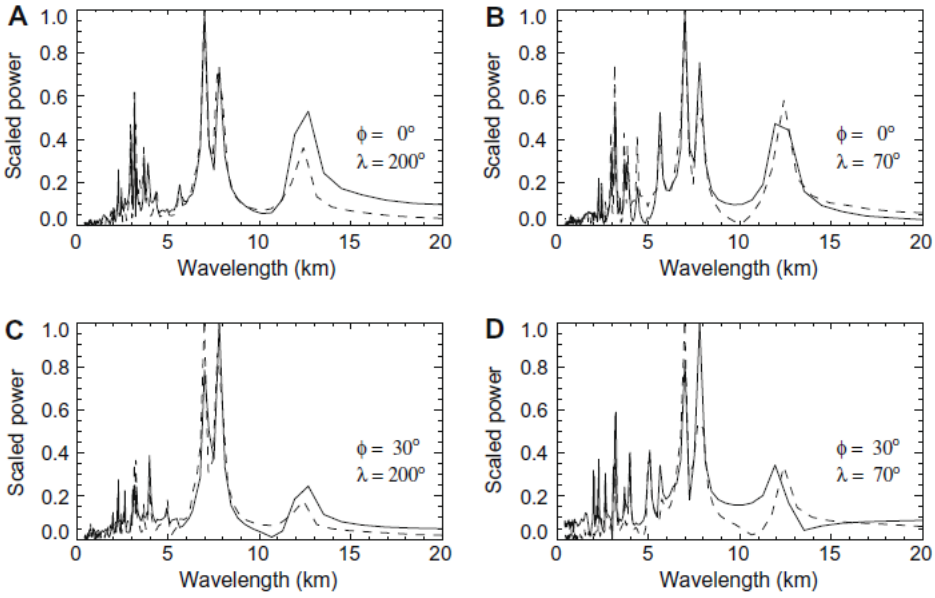

Figure 33: Power spectra for vertical profiles taken from a solution of the tidal model as shown in Figure 32. The power is scaled so that the maximum power is 1 for each plot. The relative power between the 7.7 km and 12 km peaks are shown for (a) the equator and 200E, (b) equator and 70E, (c) 30N and 200E, and (d) 30N and 70E. (Toigo *et al*. 2010).

A later study was conducted which used the same tidal model but looked for seasonal variation in Pluto's tides. This study also included damping effects onto the resulting modes of oscillation. Damping was found to be very effective in suppressing the vertical propagation of the shorter vertical wavelength listed above (~7.7 km), making the dominant surviving tidal modes have characteristic vertical wavelengths between 10-13 km (French *et al*. 2015).

Post-NH observations studies (Forget & Bertrand 2017; Bertrand *et al*. 2019b, c) have used Global Climate Models (GCMs) to examine circulations and dynamics in Pluto's atmosphere given the rich, new observations. In Bertrand *et al*. (2019b, c) detailed sublimation/deposition cycles and topography were used to reveal temperature

oscillations throughout the entire atmosphere with a strong diurnal pattern. This oscillation is shown in Figure 34. Unfortunately, relatively course resolution in the model (150 km horizontally and only 27 vertical layers) prevented more detailed inspection of structures for comparison to Toigo *et al.* (2010) and French *et al.* (2015).

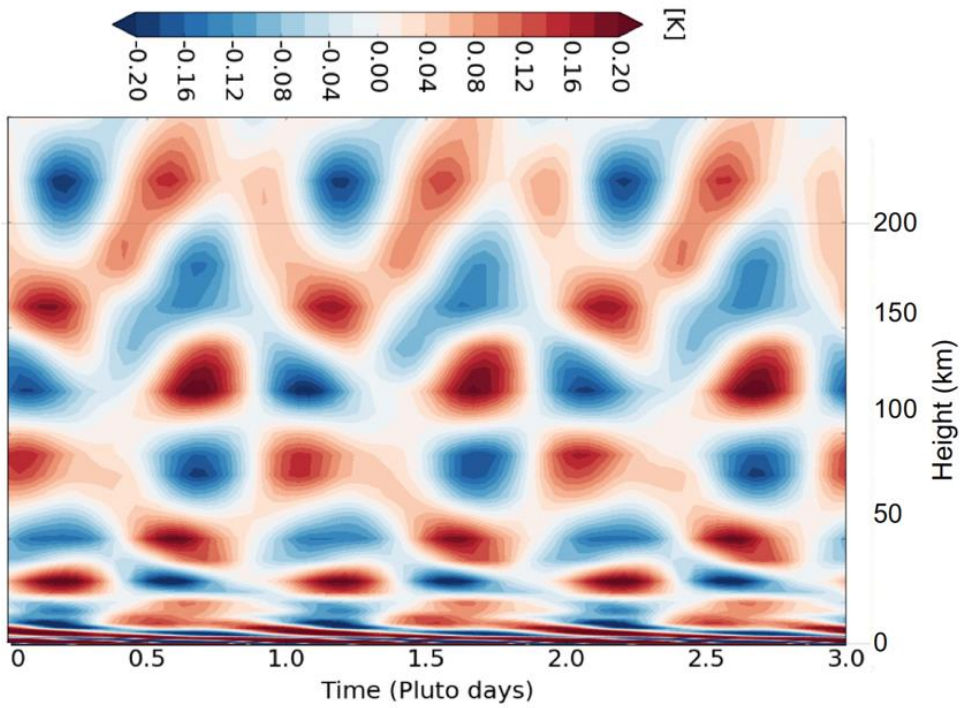

Figure 34: Temperature oscillations/perturbations resulting from sublimation/deposition cycles of ices with details topography informed by NH observations. The perturbations exhibit a strong diurnal pattern and are likely to induce thermal tides on Pluto (Bertrand *et al.* 2019b, c).

The vertical scale of this oscillation is important to note here. The vertical separation between maxima of high and low temperature perturbations above this location with time starts around 10 km below 50 km altitude and grows to around 50 km by 100 km altitude.

Since density perturbations are proportional to temperature perturbations, this rapid increase in vertical scale of the oscillations is a feature to look for in observations.

1.3.4 Rossby-Planetary Waves

A parameter used to determine the plausibility of Rossby waves to exist in a planetary atmosphere is the Rossby Radius of Deformation. This is the scale below which synoptic scale meteorology (e.g. jet stream waves, Rossby waves, etc.) is suppressed and unlikely to occur. The Rossby radius of deformation L_R, is commonly defined as

Equation 50

$$L_R = \frac{N_B H}{f}.$$

Pluto's small size (1190 km radius), largescale height above the first few kilometers altitude (50 km), and slow rotation (6.4 Earth days) implies a Rossby radius of deformation ~ 5000 km—much larger than the body's radius. An example of the Rossby radius for a planet where Rossby waves are common is that of Earth—around 1000 km, which is less than ~ 1/6 of Earth's radius. This is a common scale observed on weather charts for cyclones and anticyclones at the tropopause (Holton 2004). Because Rossby waves were first postulated by Person *et al*. (2008) to be a cause of density excursions extracted from the same March 2008 stellar occultation a more thorough consideration follows.

Person *et al.* (2008) calculated background relative density amplitudes to be ~ 0.01 with a vertical wavelength ~ 35 km at 275 km decreasing linearly to ~ 25 km at 155 km. The longer wavelength signals could be consistent with the Rossby wave dispersion relation. Person *et al*. (2008) also found that under the Rossby wave interpretation for vertically propagating wavs, relatively stringent bounds could be put on the mean zonal wind magnitude. The study found an upper bound of 3 ms^{-1}, and a lower bound of 0.1 ms^{-1}. Unique investigation of Rossby waves can be done here (post-New Horizons flyby) due to three additional pieces of information—(1) several studies have used the temperature/pressure structure of Pluto obtained by REX and surface ice distributions to calculate/constrain zonal winds likely present in Pluto's general circulation, (2) the temperature profile and surface features/dimensions such as that of Sputnik Planum are now well measured to inform Rossby wave theory, and (3) layer slopes obtained here could help constrain possible Rossby wave dimensions/dynamics.

Again, haze layer tilt would imply that the Rossby waves would be vertically propagating, and stationary vertical haze layer positions for timescales up to ~5 hrs (Cheng *et al*. 2017) suggests stationary waves relative to Pluto's surface. Linearizing the quasi-geostrophic potential vorticity equation, adopting the β-plane approximation, and neglecting changes in zonal wind speed with height and latitude (for qualitative inspections) the vertical wavenumber can be expressed as

Equation 51

$$m^2 = \frac{{N_B}^2}{f_0^2}\left[\frac{\beta}{(\bar{u} - c_x)} - (k^2 + l^2)\right] - \frac{1}{4H^2}.$$

Vertical propagation requires that $m^2 > 0$, so that for stationary Rossby waves ($c_x = 0$) a critical velocity can be found above which the waves can no longer vertically propagate. As derived in Holton (2004) and shown in Person *et al*. (2008), the expression for Rossby critical velocity is

Equation 52

$$\bar{u}_c < \beta\left[(k^2 + l^2) + f_0^2/4{N_B}^2H^2\right]^{-1}.$$

An average Brunt Vaisala frequency can be taken as ~ 1.5x10^{-3} s^{-1}, and the scale height can be adopted from Cheng *et al*. (2017) to be ~ 50 km. The Rossby parameter, $\beta \equiv 2\Omega\cos\phi_0/r_p$ and Coriolis parameter, $f_0 \equiv 2\Omega\sin\phi_0$ are defined with respect to a reference latitude, ϕ_0. Pluto's angular velocity and radius are taken to be 1.319x10^{-5} rad s^{-1} and 1185 km, respectively. Due to the position of SP, the reference latitude at which flow is disturbed was taken to be 30N. Ranges in the horizontal scale/wavelength of stationary Rossby waves were considered in order to explore the resulting ranges in Rossby critical velocity and inferred layer slopes to compare with GCM wind profiles and observed layer slopes, respectively. The presence of SP is believed to be a large disruptor to zonal mean flow and diurnal variations the drive inflows/outflows to SP. A lower bound on the Rossby wave horizontal scale can be approximated from the angular widths at Pluto's surface of the basin and an upper bound as the angular distances between day and night (terminator). The resulting Rossby critical velocities and slopes

for 25 km and 40 km vertical wavelength signals are shown in Table 3. The horizontal wavelength is taken to be $1/\lambda_H^2 = 1/\lambda_x^2 + 1/\lambda_y^2$, and a diagonal intersection of the SP region is approximated.

Table 3: Rossby wave values of critical velocity and inferred slopes using two vertical wavelengths with the approximated horizontal wavelengths.

Horizontal Wavelength [km]	$\boldsymbol{\lambda_z}$ **=40 km Slopes**	$\boldsymbol{\lambda_z}$ **=25 km Slopes**	$\boldsymbol{\bar{u}_c}$**[m/s]**
1292 (SP Scale)	0.027	0.018	0.21
1865	0.018	0.012	0.40
2460	0.014	0.009	0.63
3064	0.011	0.008	0.89
3672 (Diurnal Scale)	0.009	0.006	1.18

The other restriction for vertically propagating, standing Rossby waves is that they must exist in westward flow, with an eastward velocity matching that of the zonal mean wind. This condition is plausible considering recent Global Climate Model (GCM) predictions of a robust retrograde wind between the equator and ~ 45° N (Bertrand *et al*. 2019b, c). The slope using the SP scale is in good agreement with the slopes extracted over SP. The upper bound on zonal mean wind speed must be low to allow vertical propagation.

CHAPTER TWO

2.1 Scattering Model Development and Methods

2.1.1 Single Scattering Approximation

The intensity of light reaching an observer from a given field of view (FOV) can be expressed by Schwarzschild's Equation (including scattering) and is given by

Equation 53

$$dI = dI_{ext} + dI_{emit} + dI_{scat}$$

$$= -\beta_e I ds + \beta_a B_\lambda(T) + \frac{\beta_s}{4\pi}\int_{4\pi} P(\Omega', \Omega)\, I(\Omega')\, d\omega\, ds\,.$$

The angles presented in this equation define the direction of incident radiation ($\Omega' = (\theta', \phi')$), the direction of the observer ($\Omega = (\theta, \phi)$), and the solid angle ($d\omega' = sin\theta' d\theta' d\phi'$). The second term with $B_\lambda(T)$ is the intensity due to emission, or Planck's function defined as

Equation 54

$$B_\lambda(T) = \frac{2hc^2}{\lambda^5(e^{hc/k\lambda T} - 1)}.$$

The first approximation made to the full Schwarzschild's Equation is that the emission term can be neglected relative to other terms. This can also be interpreted as a result of single scattering, since the probability of absorption is lower when a photon is only scattered once before transmission (or that simply emission intensity at the wavelength of interest is known to be small). Mathematically this is represented by

Equation 55

$$dI_{emit} = \beta_a B_\lambda(T) \rightarrow 0 \, .$$

The phase function, $P(\Omega', \Omega)$, is defined from the scattering matrix derived in Mie Theory. It depends on the size and shape of the particles. In the case of spherical particles, or a population of randomly oriented non-spherical particles, the phase function only depends on the relative angle between the source and the observer (or phase angle), given by

Equation 56

$$cos\ \Theta = \Omega' \cdot \Omega \, .$$

The phase function must satisfy the normalization condition

Equation 57

$$\frac{1}{4\pi}\int_0^{2\pi}\int_0^{\pi} P(cos\,\Theta)dcos\,\Theta = 1\,.$$

The respective definitions of the opacities (also commonly called the volume extinction, scattering, and absorption coefficients, respectively) are defined as

Equation 58

$$\beta_e = N\sigma_e$$
$$\beta_s = N\sigma_s$$
$$\beta_a = N\sigma_a\,.$$

Above, *N* is the local number density of scattering particles. The notation $\mu = cos\,\theta$ can be introduced (note $\theta \neq \Theta$). Using the plane parallel atmosphere approximation (specifically that the optical depth along *ds* can be related to the vertical optical depth by, $\tau_z = \tau_s\mu_0$), and dividing by $d\tau_s = -\beta_e ds$, Equation 53 becomes

Equation 59

$$\mu\frac{dI(\mu,\phi)}{d\tau_z} = I(\mu,\phi) - \frac{1}{4\pi}\frac{\beta_s}{\beta_e}\int_0^{2\pi}\int_{-1}^{1} P(\mu,\phi;\mu',\phi')\,I(\mu',\phi')\,d\mu' d\phi'.$$

This equation can be further simplified by identifying $I(\Omega')$ (incident intensity on a given scattering volume) as the source intensity multiplied by an attenuation factor, e^{τ_z/μ_0}. Additional sources due to multiple scattering can be neglected in an optically thin

atmosphere (when $\tau_z \ll 1$). This approximation is valid in Pluto's atmosphere for visible wavelengths with vertical optical depths of ~ 0.02 (Gladstone *et al*. 2016, Cheng *et al*. 2017), and is mathematically stated as

Equation 60

$$I = I_0 \delta(\mu' - \mu_0)\delta(\phi' - \phi_0) e^{\tau_z/\mu_0} .$$

In addition, the intensity of emission from the sun can be taken as independent of direction out at Pluto's orbital radius (far field source of radiation, $I_0 = \pi F_0$) so that the integral in Equation 62 collapses to

Equation 61

$$\mu \frac{dI}{d\tau_z} = I - \frac{I_0}{4} \frac{\beta_s}{\beta_e} P(cos\ \Theta)\ e^{\tau_z/\mu_0} .$$

This equation can be rearranged so that

Equation 62

$$\frac{d}{d\tau_z}\left[I\ e^{-\tau_z/\mu_0}\right] = -\frac{F_0}{4\mu} \frac{\beta_s}{\beta_e} P(cos\ \Theta)\ exp\left[\tau_z \left(\frac{1}{\mu_0} - \frac{1}{\mu}\right)\right].$$

Integrating this equation from $\tau_z = 0$ to $\tau_z = \tau_z^*$, and utilizing that for limb measurements at high phase angle where there is no direct transmission contribution in the image/LOS ($I_0 = 0$), an expression for the observed intensity is found in the optically thin limit (Petty 2006) to be

Equation 63

$$I(\tau_z^*) = \frac{1}{4} F_0 \frac{\beta_s}{\beta_e} \frac{\tau_z^*}{|\mu|} P(cos\ \Theta) .$$

The intensity of radiation reaching NH/LORRI from Pluto's atmosphere/haze, specifically during egress at LORRI's pivot wavelength (607.6 nm), is assumed to be highly forward scattered radiation from haze particles with weak absorption $\left(\frac{\beta_s}{\beta_e} \approx 1\right)$. Defining the line of sight (LOS) optical depth observed by LORRI as $\tau_{LOS} \equiv \tau_s = \frac{\tau_z^*}{\mu}$, the observed, dimensionless, *I/F* for a given LORRI pixel located at (*x,y*) on an image can be expressed as

Equation 64

$$I/F = \frac{1}{4} P(\Theta) \tau_{LOS}$$

$$= \frac{1}{4} \int_{s_0}^{\infty} P(\mathrm{x}, \mathrm{y}, \mathrm{s})\ \sigma_s(x, y, s)\ N(x, y, s)\ ds .$$

The phase function, scattering cross section, and number density are now evaluated at each point, *s* (representing a column), along the LOS.

2.1.2 Model Numerical Solution for Image Simulations

The numerical form of Equation 64 is a sum of volume contributions along the LOS within a set domain of atmosphere (near spacecraft starting point and maximum range), LOS resolution, and assumptions/inputs on particle characteristics throughout the atmosphere. The most general expression for a given image pixel accounting for 3D variation in particle characteristics throughout the atmosphere as well as contributions across a distribution of particles within each scattering volume is

Equation 65

$$\frac{I}{F} = \frac{1}{4} \sum_{k=1}^{n_{LOS}-1} \sum_{n=1}^{n_{rbin}-1} P_{kn}(\Theta)\sigma_{s_{kn}} N_{kn}(z)\delta s,$$

where the sums along the LOS are in index *k* at resolution δs for some number of points n_{LOS} and across the particle distribution in index *n* for some number of radius bins n_{rbin} . The variable z is introduced above in order to show that Pluto's mean state/background atmospheric number density and haze brightness can be taken as azimuthally symmetric and represented by a decaying exponential with a constant scale height ($N(z) = N_0\, e^{-z/H}$). This scale height was found to be around 50 km (Cheng et al. 2017). For the

simple case of a monodisperse particle distribution, where particle characteristics are approximately constant along the LOS, the expression for I/F can be simplified to

Equation 66

$$I/F = \frac{1}{4} P(\Theta)\sigma_s \sum_{k=1}^{n_{LOS}} N_k(z)\delta s \, .$$

This expression can also be used if the variation in particle number density is assumed to dominate changes in I/F.

2.1.3 Simulating LORRI's Field of View (FOV)

The scattering model developed and used in this dissertation has been adopted from a previous version dedicated to simulating images taken by the Inner Magnetosphere Imager (IMI) mission of optically thin scattering in Earth's plasmasphere (Gladstone et al. 1992). The model uses NH/LORRI ephemeris data from the Planetary Data System (PDS). These inputs are the Pluto nadir point in Latitude and Longitude using Pluto right hand rule (RHR) and in ecliptic coordinates, range to Pluto, LORRI boresight (BS) location in ecliptic coordinates, and LORRI roll angle relative to Celestial N. A grid equal to the imager's resolution (LORRI, 1024x1024) is generated with nadir point at center, which is then translated to the BS, rolled by the proper angle, and

rotations conducted in order to get LOS points into Pluto RHR coordinates for calculations and output.

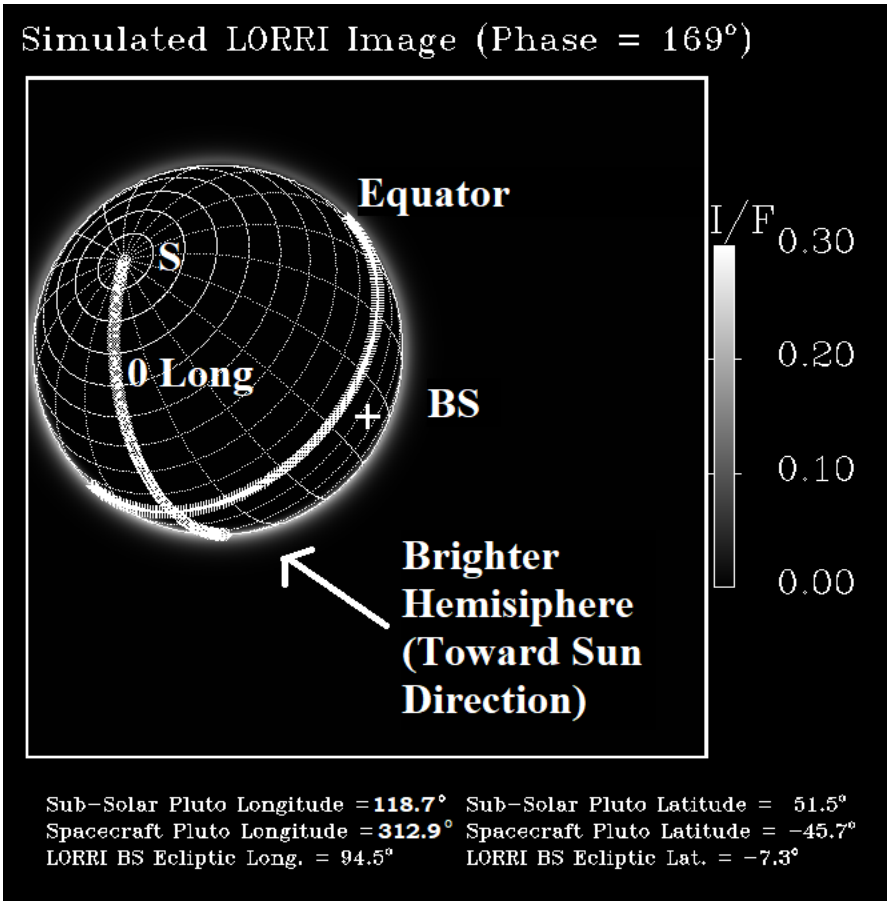

Figure 35: A simulation of LORRI's FOV using the scattering model viewing geometry. Some of the ephemeris data used is shown at bottom, with a projection of Pluto's Lat./Long. grid in Pluto RHR shown on disk. A brighter lower hemisphere is indicated, showing that Pluto's shadow is properly being considered, reducing I/F within the shadowed region. A monodisperse population of spherical particles was used to simulate the I/F range indicated.

An example of the simulated I/F with LORRI's FOV is shown in Equation 35. The projection of Pluto's graticules are shown, with 0° Longitude and the equator

indicated with diamond and cross symbols, respectively. Pluto RHR is defined as Longitude increasing in the direction of fingers curling around the thumb of the right hand with the thumb in the direction of Pluto's North pole. Latitudes are in increments of 10° and Longitudes in increments of 20°. LORRI's FOV is $0.29 \times 0.29^{\circ}$, but a FOV of several degrees is shown for demonstration. LORRI's BS position is indicated with some of the ephemeris data used at bottom. A scale for the simulated I/F range is also shown, with a brighter I/F for the lower hemisphere of the disk due to Pluto's shadow decreasing I/F contributions in the upper hemisphere.

The wavelengths LORRI is sensitive to are shown as the black line in Figure 36, below. Other instrument response functions (all normalized to the maximum response value for each instrument) are shown for comparison. LORRI has a broad response function compared to the other instruments to maximize spatial resolution in the optical band.

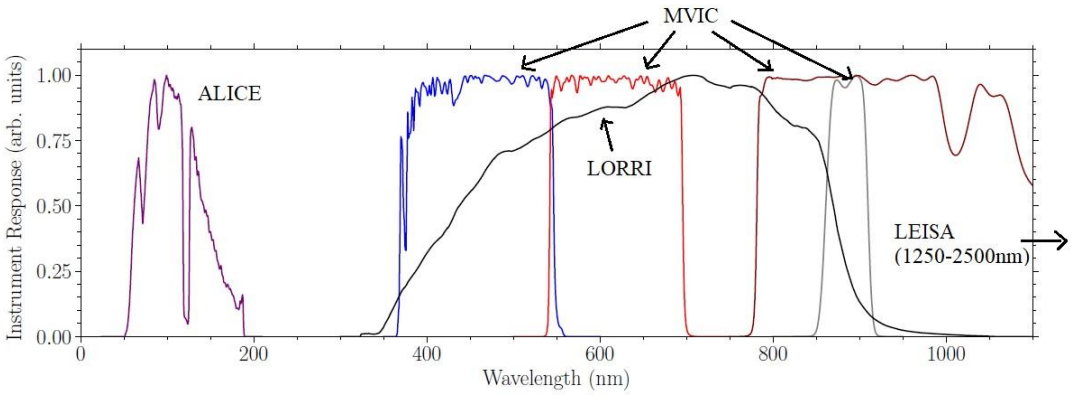

Figure 36: Normalized responses of several NH instruments including LORRI for comparison of band passes. LORRI's bandpass is the largest to maximize spatial resolution in the optical range.

2.2 Scattering Calculations and Parameters

2.2.1 Scattering by Spheres

Mie Theory describes the scattering of radiation by particles. There are three commonly referred to scattering regimes defined by the particle's radius relative to the wavelength of light being scattered. This quantity is called the scattering parameter, defined as

Equation 67

$$x = \frac{2\pi r_p}{\lambda}.$$

The scattering regimes are then given as

Equation 68

$$x \ll 1, Rayleigh$$

$$x \approx 1, Mie$$

$$x \gg 1, Geometric\ .$$

The simplest light scattering regime is Rayleigh scattering. In this regime, the phase function can be taken as

Equation 69

$$P(\Theta) = \frac{3}{4}(1 + cos^2\Theta).$$

This results in light being scattered symmetrically forward and backward by particles that are ≤ 10 nm in the optical band (Petty 2008). Additionally, the scattering cross section can be approximated (due to the scattering efficiency being truncated) so that

Equation 70

$$\sigma_s \propto \frac{r_p^6}{\lambda^4}\ .$$

Consequently, the shorter wavelengths (blue) are scattered much more efficiently that longer (red) wavelengths (by a factor $(\lambda_2/\lambda_1)^4$ for $\lambda_2 > \lambda_1$). This leads to a blue sky on Earth due to Nitrogen scattering. This higher scattering efficiency for bluer (shorter) wavelengths is also why sunsets appear red. When looking toward the sun at sunset (small scattering angles) a large portion of the LOS is through a dense atmosphere where multiple scattering becomes important. Although all colors are scattered efficiently at small scattering angles (due to same phase function), the bluer wavelengths are more likely to be scattered more than once, or out of our LOS, leading to a larger fraction of yellow, orange, and red passing through our LOS.

The MVIC imager onboard NH has red and blue channels and observed a large blue/red intensity ratio implying Rayleigh scattering as described above. This ratio decreased with altitude indicating a transition away from the Rayleigh regime with decreasing tangent altitude. Although Pluto's skies appeared blue, a large forward scattering component in intensity was measured for a large range in phase angle indicating that haze particles are large enough to fall within the Mie regime (Gladstone *et al*. 2016). A diagram illustrating the difference between the Rayleigh and Mie regimes, mainly differentiated by a forward scattering lobe for the Mie phase function and a symmetric phase function for the Rayleigh regime.

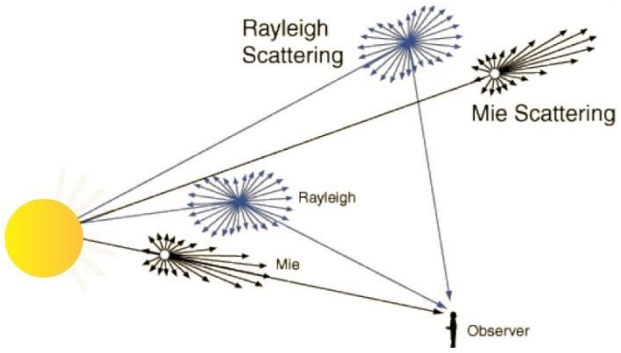

Figure 37: Diagram illustrating the difference between a Rayleigh regime phase function and a Mie regime phase function as viewed by the relative angle between the source, the scattering particle, and the observer. For the Rayleigh regime, light is scattered symmetrically forward and backward. In the Mie regime, light is scattered preferentially forward.

For both observations to be explained in Pluto's tenuous atmosphere (negligible multiple scattering), smaller particles (≤ 10 nm) at higher altitudes must grow to larger particles at lower altitudes during a haze production process (Gladstone *et al*. 2016).

Forward scattering from haze particles at large phase angles between the sun and NH spacecraft during/just after flyby of the Pluto system is the focus of this dissertation. A diagram showing the stages of the flyby is below with sun and Earth direction, and Pluto shadow indicated relative to spacecraft position with time.

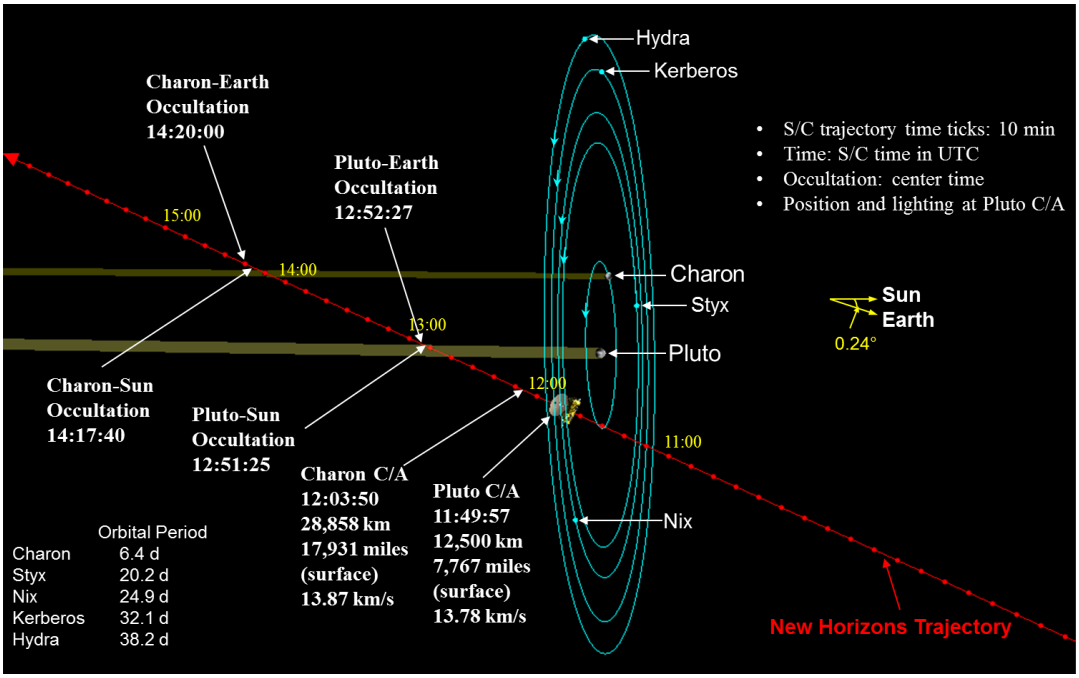

Figure 38: A schematic of the NH trajectory through the Pluto system. Most observations analyzed and modeled in this dissertation were obtained after 15:00, with some higher resolution data obtained ~ 12:00.

If the scattering particles are assumed to be homogeneous spheres, the general expression for the scattering cross section, σ_s , related to the scattering efficiency, Q_s , is

Equation 71

$$\sigma_s = \pi r_p^2 Q_s \, .$$

A complete expression for the scattering efficiency can be derived analytically for the spherical particle case from Mie Theory starting with Maxwell's equations. After constructing the wave equation for unpolarized light incident on a spherical particle, the

resultant fields for the particle both internally and externally can be derived. The resultant general expression for scattering efficiency is then as shown in Bohren and Huffman (1998) (without truncation as mentioned for the Rayleigh regime above)

Equation 72

$$Q_s = \frac{2}{x^2}\sum_{n=1}^{\infty}(2n+1)(|a_n|^2 + |b_n|^2)\,.$$

The scattering efficiency can be numerically calculated from Mie scattering codes for spherical or aggregate particles. The coefficients a_n and b_n are functions of the size parameter *x*, and the complex refractive index, *m*. The refractive index is defined as

Equation 73

$$m = \frac{N_2}{N_1} \approx N_2 = n + ik\,.$$

where Pluto's atmosphere is predominantly Nitrogen, so that $N_1 \approx 1$ as with Earth's atmosphere. The constants *n* and *k* determine the scattering and absorption characteristics of the particles, respectively. They must be determined experimentally. The values adopted in this study were taken from experiments conducted to replicate tholin-like particle characteristics in Titan's atmosphere (Khare *et al*. 1984; Gladstone *et al*. 2016).

As mentioned previously, another quantity important in describing the scattered intensity reaching an observer from a particle is the phase function. The phase function

describes the angular dependence of the scattered light relative to the incident light. Due to this angular dependence, a coordinate system must be defined relative to the source and observer. The conventional coordinate system defining the incident basis, scattering basis, scattering plane, and phase angle is shown in Figure 39 below—taken from Figure 3.3 of Bohren and Huffman (1998).

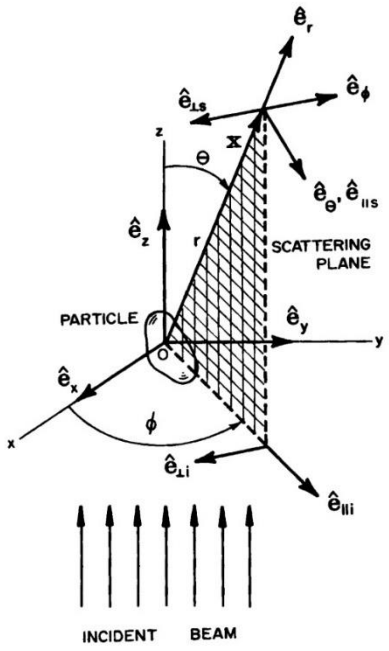

Figure 39: Diagram showing the coordinate basis of the incident beam of light, particle coordinates, and scattering plane with scattering basis—all of which are used to define the phase angle.

This coordinate system can be used to decompose the incident and scattered electric fields into components parallel and perpendicular to the scattering plane. The scattered and incident fields are then related by the amplitude scattering matrix

Equation 74

$$\begin{pmatrix} E_{\parallel s} \\ E_{\perp s} \end{pmatrix} = \frac{e^{ik(r-z)}}{-ikr} \begin{pmatrix} S_2 & S_3 \\ S_4 & S_1 \end{pmatrix} \begin{pmatrix} E_{\parallel i} \\ E_{\perp i} \end{pmatrix}.$$

Stokes parameters can also be constructed from the parallel and perpendicular components of the electric field. The relationship between the incident and scattered stokes parameters are expressed as

Equation 75

$$\begin{pmatrix} I_s \\ Q_s \\ U_s \\ V_s \end{pmatrix} = \frac{1}{k^2 r^2} \begin{pmatrix} S_{11} & S_{12} & S_{13} & S_{14} \\ S_{21} & S_{22} & S_{23} & S_{24} \\ S_{31} & S_{32} & S_{33} & S_{34} \\ S_{41} & S_{42} & S_{43} & S_{44} \end{pmatrix} \begin{pmatrix} I_i \\ Q_i \\ U_i \\ V_i \end{pmatrix}.$$

Above, I_s and I_i are the scattered and incident intensities, and *Q*, *U*, and *V* are parameters defined in terms of the parallel and perpendicular electric field components relative to the scattering plane. Most important to this dissertation are the two definitions of the stokes parameter S_{11}, the first in terms of the amplitude scattering matrix elements, the second defined as the scattering irradiance over the incident irradiance for a given phase angle,

Equation 76

$$S_{11} = \frac{1}{2}(|S_1|^2 + |S_2|^2 + |S_3|^2 + |S_4|^2)$$

$$S_{11} = \frac{1}{k^2 r^2} \frac{I_s}{I_i}.$$

The second definition for S_{11} assumes the incident irradiance is unpolarized. If this is the case, then S_{11} specifies the angular distribution of scattered light and can be used to calculate the phase function. The factor multiplied in the second definition of Equation 76 contains the wavenumber of light being scattered *k*, and the distance from the scattering point to the detector, *r*.

Another important quantity for calculating the phase function is the differential scattering cross section—defined as the energy scattered per unit time into a unit solid angle about a direction Ω for unit incident irradiance. This quantity can be defined in terms of S_{11} by

Equation 77

$$\frac{dC_{sca}}{d\Omega} = \frac{r^2 I_s}{I_i} = \frac{S_{11}}{k^2}.$$

For an isotropic medium, or for randomly oriented particles, the scattered irradiance and differential scattering cross section are independent of ϕ, becoming only dependent on one angle—the phase angle Θ. The phase function can then be defined as the differential scattering cross section divided by the scattering cross section, i.e.

Equation 78

$$P(\Theta) = \frac{4\pi}{C_{sca}} \frac{dC_{sca}}{d\Omega}.$$

The factor of 4π is not assumed in all texts but will be adopted here as it provides values in the range of literature built upon by this study/dissertation (Bohren and Huffman 1998; Gladstone et al. 2016; Cheng et al. 2017). If in the above expression, we take $C_{sca} = \sigma_s$ as defined in Equation 71, then

Equation 79

$$P(\Theta) = \frac{4\pi}{\sigma_s} \frac{S_{11}}{k^2}.$$

The Mie scattering code used to find the scattering efficiency and phase function was adapted from original code outlined in Bohren and Huffman (1998) for a homogeneous sphere. The program outputs the scattering efficiency, S_1, and S_2 given a size parameter and complex refractive index for the sphere. For the cases where the incident light is unpolarized and the sphere is homogenous $S_3 = S_4 = 0$ and the phase function can be calculated directly from the first expression in Equation 76. Phase function values for a range of phase angles and particle sizes are plotted in Figure 40. Values of scattering efficiency are also shown for each corresponding particle radius. Calculations were done with the Khare *et al*. (1984) refractive index previously mentioned. The phase angle of NH adopted for most of the images simulated is shown as the vertical dotted red line.

Depending on the source, the phase angle is sometimes defined as the offset from straight line transmission, but here it is the larger angle swept between the vector pointing to the source of light and the scattering volume/particle. A larger parameter space in particle size and phase angle is shown in Figure 40. The forward scattering peak becomes even more evident here, as well as some back-scattering lobes and a cavity for relatively larger particles at phase angles slightly larger than 90 degrees.

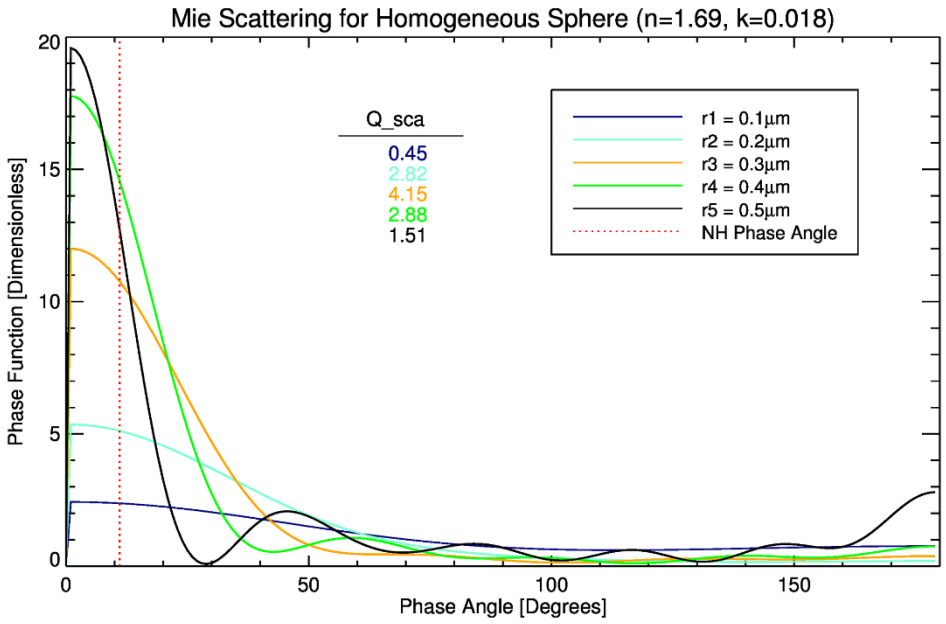

Figure 40: Phase function and scattering efficiency values for several particle sizes and phase angles at LORRI's pivot wavelength of 607.6 nm.

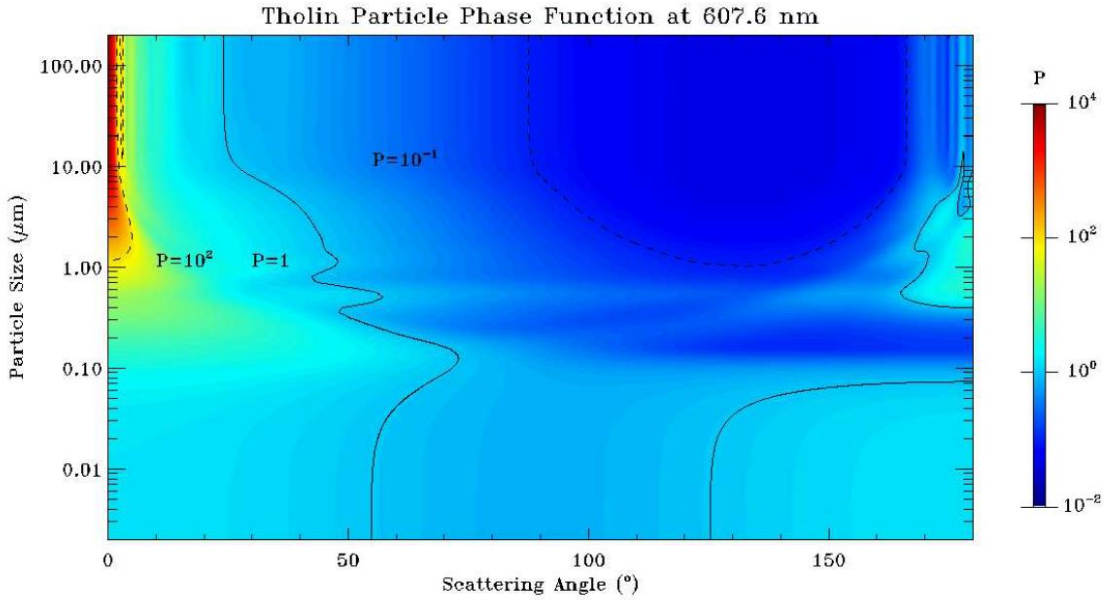

Figure 41: Larger parameter space in particle size and phase angle for the same wavelength of light and particle composition used in Figure 40.

Each particle and scattering volume along the LOS has an associated phase angle. Several additional simplifications in calculating the phase angle can be made to greatly reduce computational time. The Pluto system is far enough from the sun that light rays can be assumed to be parallel to each other (far field approximation). Consequently, the phase angles along a given LOS representing a pixel in the LORRI images can be assumed to be constant and no longer need to be calculated for every point along the LOS. This can be seen in the illustration within Figure 42 along the bold black arrow originating at the spacecraft and pointing through Pluto's atmosphere. The approximately parallel rays are depicted as yellow. The line passing through the nadir point (with spacecraft range) is also shown. If Pluto's radius and atmospheric extent (grey and blue areas) are large enough fractions of the spacecraft range from Pluto center, then the phase angle for a

given LOS on one side of the disk will be considerably different from the phase angle for a given LOS on the other side. However, if the spacecraft range is sufficiently large, then the change in phase angle from one side of the disk to the other is small and can become negligible (visualized by moving the spacecraft in Figure 42to the right and off the page). For this special case, the phase angle can also be approximated as constant across LORRI's entire FOV. Scattering parameters described above can then be calculated all for the same phase angle for a given image captured by LORRI. This was the case for most images simulated for LORRI in this dissertation.

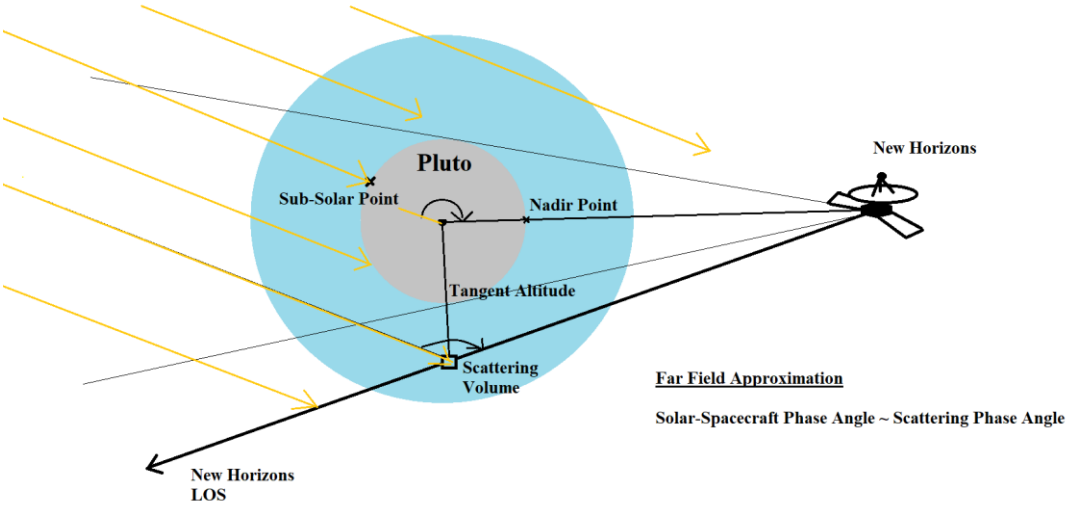

Figure 42: Illustration of the spacecraft and scattering volume phase angles. For the far field approximation, the change in phase angle will be negligible along the LOS for a sufficiently small range of distance (e.g. across Pluto's atmospheric extent). Additionally, if the spacecraft range from Pluto is sufficiently large, then the change in phase angle across LORRI's FOV is also negligible. Consequently, the phase angle can often be approximated as constant for the simulation of a given LORRI image during the calculation of scattering parameters.

2.2.2 Scattering by Fractals

Scattering by aggregates is most commonly handled by considering an aggregate or fractal particle composed of many spheres or monomers, each of which scatters light and contributes to the scattering cross section of the aggregate. Scattering data was implemented here from Tomasko *et al*. (2008), where scattering properties of aggregates were related to physical properties through a parameterization scheme using the fractal dimension, number of monomers, monomer size parameter, and index of refraction. The scheme assumed coherent superposition of scattering by the monomers, and linear superposition of absorption.

The scattering cross section for aggregates was calculated with the modified cross section equation for a particle composed of monomers to be

Equation 80

$$\sigma_{s,agg} = \pi r_m^2 N_m^{2/3} Q_{s,agg} \, ,$$

where the number of monomers N_m in the aggregate with radius r_m can be obtained using

Equation 81

$$N_m = \left(\frac{R_f}{r_m}\right)^{D_f} .$$

for an aggregate/fractal of radius R_f, and fractal dimension of D_f. A fractal dimension of 2 was adopted throughout this dissertation for all aggregate scattering calculations. Fractals of this dimension are known to occur from hierarchical cluster-cluster aggregation where aggregates approach each other in random ballistic trajectories (Cabane et al. 1993; Tomasko et al. 2008).

The scattering efficiency was taken from Tomasko et al. (2008) Appendix A and is shown as a function of monomer size parameter below.

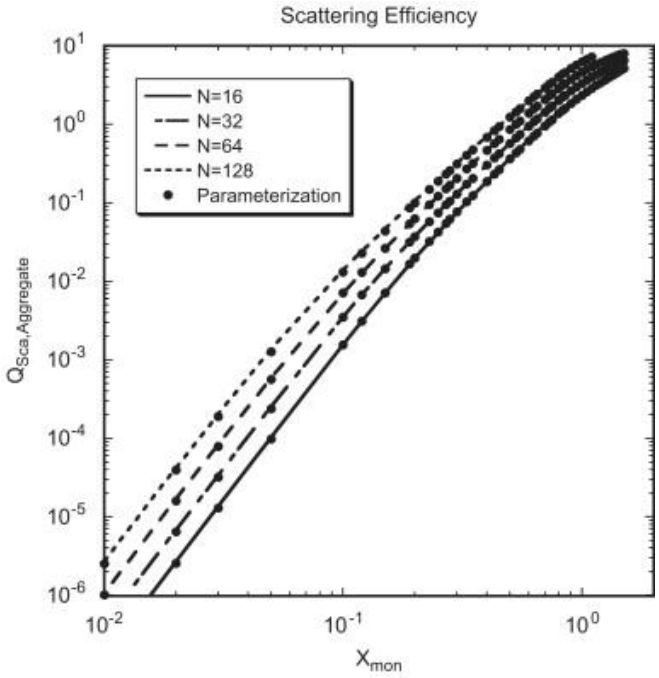

Figure 43: The scattering efficiency of aggregates composed of a range of size parameters. The size parameter for 10 nm monomers at LORRI's pivot wavelength is ~ 0.1.

This scattering efficiency includes an enhancement factor, which takes into consideration the possibility that an aggregate composed of a given number of monomers could have a scattering cross section larger than the associated total scattering cross section of the same number of dispersed monomers.

The phase function for aggregates was again adopted from Tomasko *et al*. (2008). The range of phase function values found for a range of phase angles is shown in Figure 44.

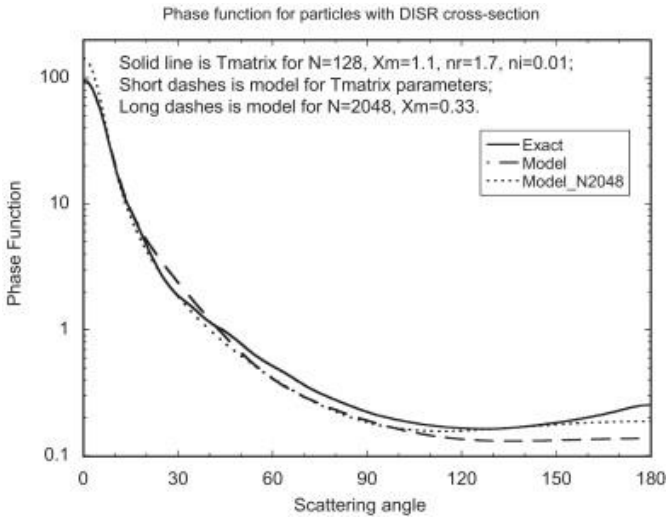

Figure 44: Phase function values adopted from Tomasko *et al*. (2008).

2.2.3 Application of CARMA Datasets to Scattering Model

In the study by Cheng *et al*. (2017), the visible phase function near the surface can be reproduced for a spherical log-normal size distribution with standard deviation of 0.2 around spheres of 0.5 μm radius and surface number density of 0.1 cm^{-3} falling off exponentially with scale height 50 km. Similar agreement was found at and above 45 km with an aggregate exponential haze with bulk radius of 0.15 μm and surface number density of 15 cm^{-3}. The shape of extracted LORRI I/F profiles also were in good agreement with this model (Cheng *et al*. 2017). Due to these findings a similar exponential background haze was assumed when simulating the background haze and layers in this dissertation.

However, a more physically based background haze derived from microphysical processes was also included in this dissertation to explore effects on layering from distribution shapes and interactions with the perturbations. The Community Aerosol and Radiation Model for Atmospheres (CARMA) was adapted in Gao *et al*. (2016) for Pluto's haze and handled the evolution of particle distributions originating from photochemistry and shaped by downward transport and coagulation. The microphysical processes were treated as in Titan's detached haze layer and several cases were considered: spherical particles grown by 5 nm and 10 nm spherical monomers, and cluster-cluster aggregate (fractal dimension of 2) particles again grown by either 5 nm or 10 nm monomers. Data from Gao *et al*. (2016) was obtained for distributions containing 30 radius bins extending from the surface to ~ 2000 km. Due to Pluto's tenuous

atmosphere, only data below 400 km was used in the scattering model. Three cases were considered in the scattering model, and their total number densities (summed across the distributions) with altitude are shown in Figure 45. A couple notable features are the larger number densities of the fractal case below ~ 75 km and a large peak in number density in all cases just above the surface (~3 km).

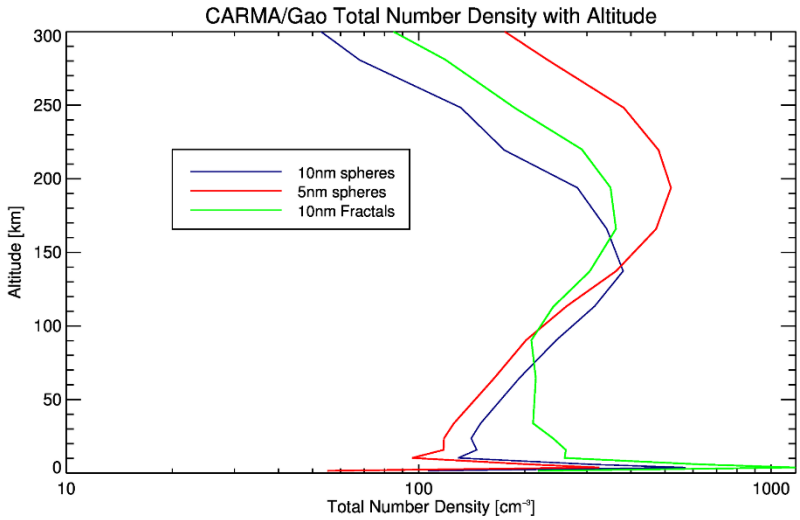

Figure 45: CARMA/Gao et al 2016 total number density profile comparisons for the three cases of background haze considered in the scattering model to show origins of I/F profile shape and magnitude.

The sphere size distributions were used with scattering codes to derive corresponding cross sections and phase functions used by the scattering model. However, for aggregate particles only one case of cluster-cluster aggregates of fractal dimension 2 and monomer size parameter 0.1 (a size parameter matching 10nm monomers at LORRI's pivot

wavelength) could be considered. Data available from T-matrix codes was used to extract scattering cross sections for the aggregate distributions (Mishchenko, M. I. *et al*. 1996, Tomasko *et al*. 2008). Although phase function values are calculated by the Mie scattering code for all sphere sizes, a constant value was taken from Tomasko *et al*. (2008) for aggregates above 80 km in Titan's detached haze layer at a given phase angle (here independent of aggregate bulk size).

Both sphere and aggregate calculations assume refractive index values adopted by Gladstone *et al*. (2016) from Khare *et al*. (1986) for tholin particle compositions. Figure 46 shows resulting scattering cross sections for sizes across most of the size distribution used (top), and a zoom of the portion containing the highest number densities is also shown (bottom). Spheres grown by 5 nm and 10 nm monomers coincide exactly across the distribution and have cross sections considerably larger than the aggregate particles at the same bulk radius. However, an enhancement factor discussed in Tomasko *et al*. (2008) causes the aggregate particles to have a larger scattering cross section than the equal radius sphere for sizes less than ~ 0.04 μm (approaching monomer sizes).

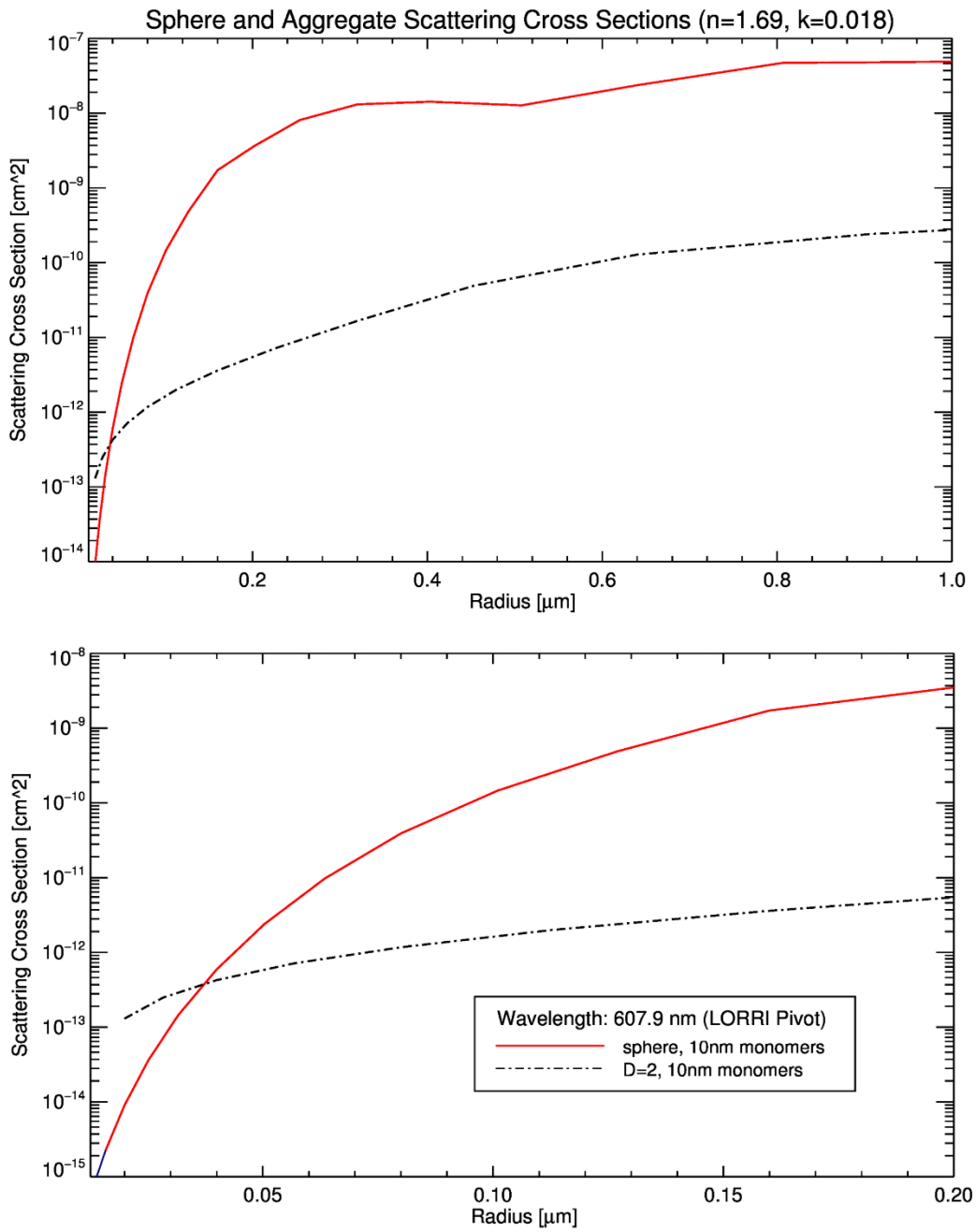

Figure 46: (Top) Scattering cross sections across most of the size distribution range considered in the CARMA model. **(Bottom**) Zoom in of the part of the distribution over which most of the particle number density resides. Fractal aggregates have a scattering cross section 2-3 orders of magnitude less than the equivalent radius sphere over most of the radius range.

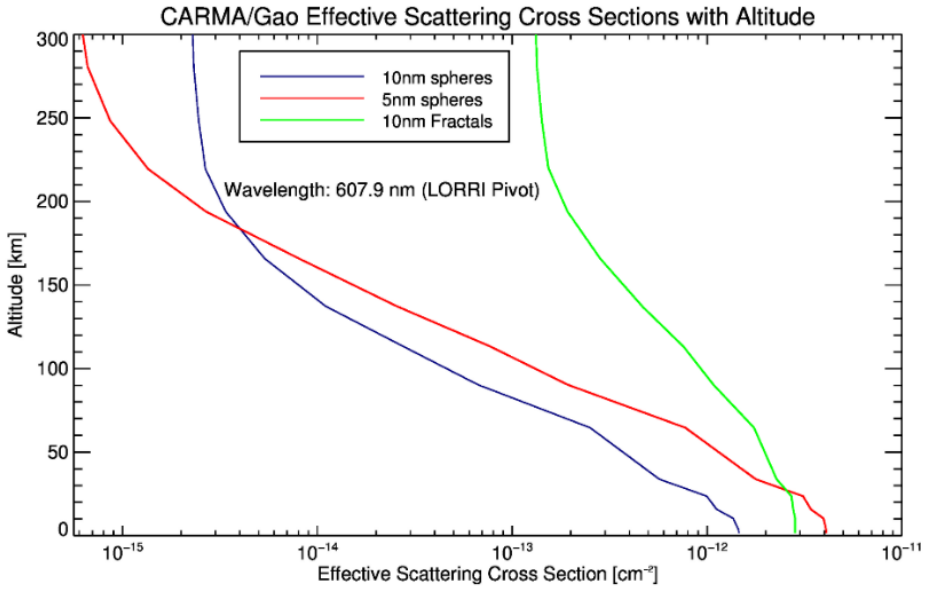

Figure 47: Effective scattering cross sections for the 3 CARMA cases found by weighted contributions at each altitude from each of the 30 radius bins. The 10nm monomer grown fractals have considerably larger bulk radii generating a much larger effective scattering cross section for almost the entire altitude range.

The weighted contribution of radius bins across the distributions for each case is depicted as an effective cross section in Figure 47. The corresponding effective phase functions for the two sphere cases resulted in a phase function only varying between ~ 1.4 – 1.68 over the entire altitude region. The assumed phase function value for aggregates was taken as ~14.5 for the P_MULTI and FULLFRAME image sequences with phase angles of 169° and 165.9°, respectively. The phase function for HIRES, with a phase angle of 148°, was used as a free parameter for aggregates and taken to be ~ 5 for spheres (see Figure 40). A best fit to the background I/F profile magnitude of LORRI

extracted I/F profiles was sought, and a phase function value of 5 provided the best fit for the CARMA distribution.

2.3 Summary of Model Code Structure

In summary, the main scattering model routine calculates the I/F for a grid of pixels representing LORRI's resolution and FOV, as well as the viewing geometry of NH. A background haze is assumed so that scattering parameters can be calculated externally and save computational time. As will be covered in more detail in Chapter 4, perturbations/variations to the background haze can be input to the model and included in LOS calculations (e.g. those caused by gravity waves). The simulated images are then input into several plotting routines to generate the image frame, apply graticules, extract profiles, and undergo processing for 1:1 comparison with processed LORRI images and mosaics. A diagram of the interrelationship of these routines is shown in Figure 48.

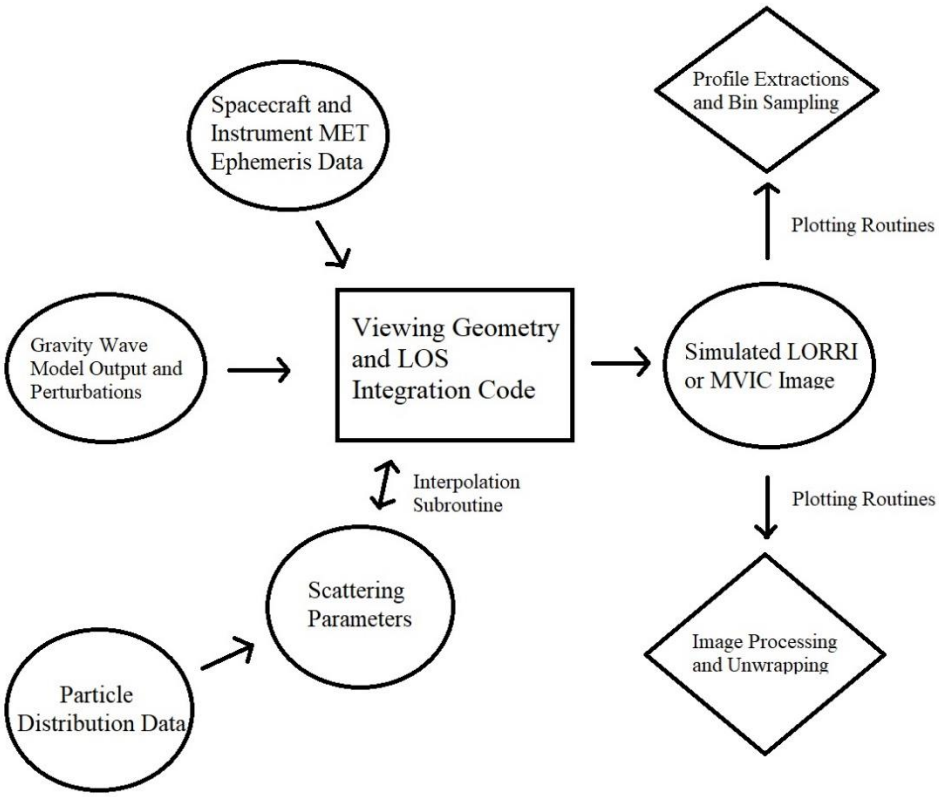

Figure 48: Diagram showing the interrelationships between inputs, main routine, and post-processing routines composing the scattering model.

2.4 LORRI Data Processing for Model Comparisons

2.4.1 Conversion of Data Number to I/F

Below is the conversion of DN to I/F as outlined in the New Horizons SOC to Instrument Pipeline ICD (section 9.3.1.4 on pages 42-45). The irradiance value is first calculated from the corrected DN value using the image exposure time *TEXP* (s), and the conversion factor *RSOLAR* (2.664×10^5 [(DN/s/pixel)/(ergs/cm^2/s/sr/Å)]) which converts count rate to radiance for a resolved source at LORRI's pivot wavelength if the target has a solar-like spectral distribution. The conversion equation to obtain irradiance is

Equation 82

$$I = C/TEXP/RSOLAR\ ,$$

where *C* is the flat-fielded DN signal. The final *I/F* value is then calculated using this irradiance as

Equation 83

$$I/F = \pi\ I\ r^2/F\_solar,$$

where r is the target's heliocentric distance in AU and *F_solar* is the solar flux at a heliocentric distance of 1 AU at LORRI's pivot wavelength (176 erg/cm^2/s/Angstrom).

2.4.2 Sources of Error

Images obtained from the LORRI archive are in FITS file format. LORRI operates in two binning modes: 1x1 and 4x4. The images of interest in this study were collected in 1x1 mode with raw image dimensions of 1028x1024 where columns 0 through 1023 are the optically active region of the CCD and the remaining 1024-1027 columns are the optically inactive region (dark columns) and represent a temperature-specific measurement of the bias value. Level 2 LORRI images are used, so that the calibrated image corrections are bias subtraction, smear removal, and flatfield correction. An example of the error due to smearing is shown below for an image taken near NH Jupiter flyby where the smear removal correction algorithm was applied.

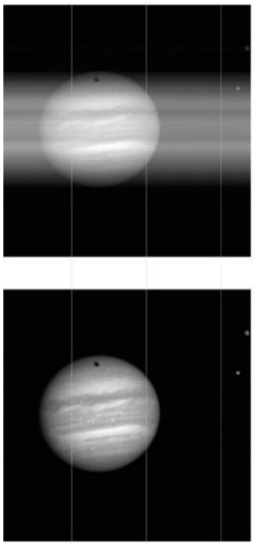

Figure 49: Example of the image smearing effects at top due to the absence of a shutter on LORRI and the corrected image at bottom.

Error sources for each of these corrections can be considered, but the dominant error source is stray light. Stray light contribution to the FULLFRAME images and the associated uncertainty was estimated by taking five 200x200 pixel “dark” regions within the image and finding the average and standard deviation DN. The five regions with their associated stray light sources are shown below.

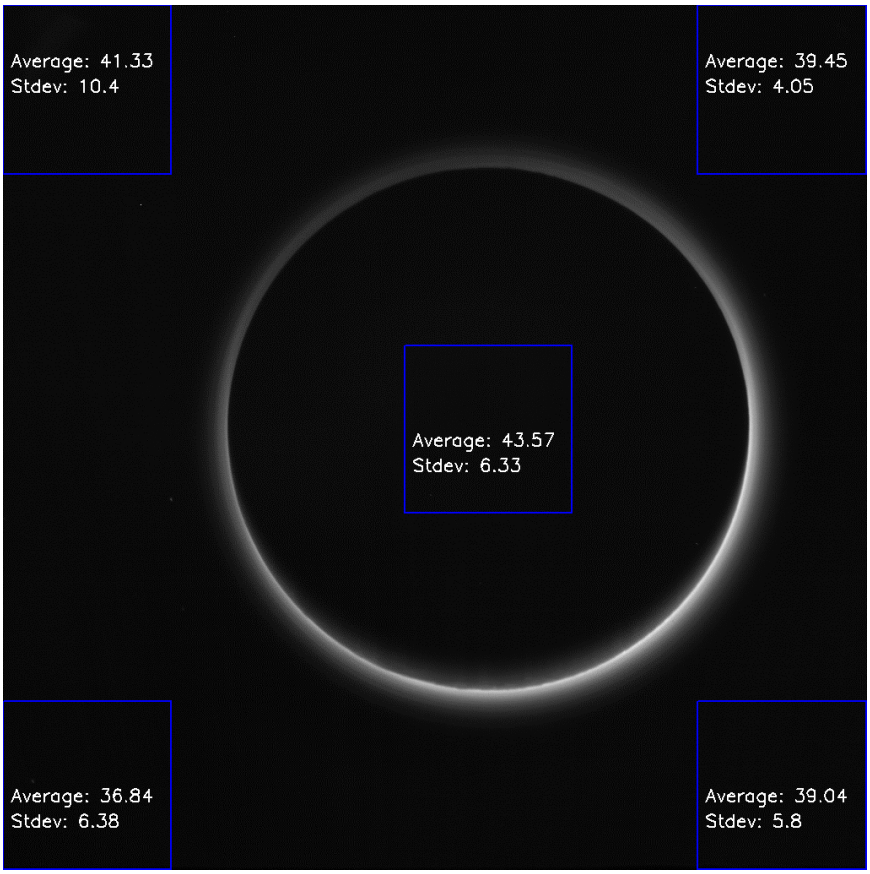

Figure 50: Example of stray light error/contributions in dark regions of a LORRI image. The standard deviation was used to approximate the dominant source of error in the FULLFRAME and P_MULTI image sequences.

The stray light average was then subtracted from the image DN values and the stray light standard deviation can be added in quadrature with the other error sources defined in the following equation for error estimation of a given LORRI pixel is

Equation 84

$$\sigma_I = \frac{\sqrt{\frac{P_{mI}}{g} + RN^2 + (f_{Pm})^2 + \sigma_S^2}}{FF}.$$

The above quantities are P_{mI} : observed signal for each pixel after bias subtraction but before smear removal, g : electronics gain (22 e/DN), RN: electronics noise (1.3 DN) , f_{Pm} : estimated error in the reference flat-field image (0.005), σ_S : stray light error, and FF : the value of the reference flat-field image at the relevant pixel (dimensionless). The 1-sigma error for a given pixel can be estimated as the pixel 1-sigma I/F since conversion factor uncertainties are much smaller than the sources of uncertainty outlined above. Given that most of the uncertainty is due to stray light, the LORRI FULLFRAME error bars on a given radial profile are ~6.59 DN = 0.0032 I/F.

CHAPTER THREE

LORRI Observations of Waves in Pluto's Atmosphere (Jacobs *et al.* 2019a)

Abstract

Observations during the New Horizons (NH) spacecraft flyby of Pluto in July 2015 revealed that Pluto's atmosphere supports an extensive circumplanetary haze with embedded layers, suggesting several possible microphysical and/or dynamical excitation processes. The purpose of this paper is to build upon existing observations and analyses of Pluto's atmosphere—specifically of the complex haze layer structures—to identify wave structure in Pluto's atmosphere. Here three NH/Long Range Reconnaissance Imager (LORRI) image sequences from the flyby at high phase angles (148˚- 169˚) and three different resolutions (0.093 km/pix, 0.96 km/pix, and 3.86 km/pix) are analyzed. Several haze layer characteristics were extracted, namely—slope, amplitude, waveform, and the associated power spectral densities (PSDs); and their variations with local geography. These are then explored in the context of possible wave types in Pluto's atmosphere, such as tidal and orographically driven inertia-gravity (buoyancy) waves. PSD peaks at 8-10 km and 18-22 km vertical wavelength are found in NH images, which is consistent with the perturbations seen in Earth-based stellar occultations of Pluto's

atmosphere. The 8-10 km signals are localized to low-latitudes and equatorial regions and the 18-22 km signals are more globally distributed. Haze layer background relative amplitudes were found to be around 0.01-0.04. Slopes of layers were found to be correlated with the emergence and disappearance of a 25 km layer around 30°N. An amplitude increase of oscillations below 30 km altitude exists in the high-resolution image sequence. These findings indicate the possibility of waves in Pluto's atmosphere and motivate further studies of wave dynamics combining NH data with state-of-the-art models of Pluto's atmosphere. These results are important because they can provide strong constraints to models and to the type of waves that can be present in Pluto's atmosphere.

3.1 Introduction

Waves in Pluto's atmosphere were first proposed as an explanation for resolved structures found in the atmospheric density and temperature of Pluto derived from Earth-based stellar occultation measurements (see Person *et al.* 2008 for details). Models using internal and inertial gravity wave dispersion relations were proposed to explain these observed perturbations (McCarthy *et al.* 2008, Hubbard *et al.* 2009). These investigations focused on tangent altitudes in the range of 150 – 400 km. McCarthy *et al.* (2008) found that the power spectral densities (PSDs) of background normalized flux profiles in the near-infrared yielded evidence for a wave with vertical wavelength ~ 10 km at 150 km tangent altitude, increasing to ~18-20 km near 400 km altitude. The inferred wavelengths and density perturbation amplitudes were found to be consistent

with those produced by a saturated gravity wave dispersion relation with a horizontal wavelength of 1000 km. Hubbard *et al.* (2009), used scintillation theory along with the same atmospheric and wavenumber assumptions to differentiate the observed PSD from that which would be produced by turbulence. They found the strongest inferred vertical wavelength of ~13 km in the lowest 50 km altitude of the data. The possibility that Rossby waves could be present in their PSDs below a theoretical cut-off vertical wavenumber for gravity waves was also proposed. Possible driving mechanisms (other than turbulence) necessary to generate the observed and modeled wave characteristics in these studies were not explored in detail.

Person *et al.* (2008) focused on using the Rossby wave dispersion relation and an assumed isothermal atmosphere above 150 km, with a density profile that fell off exponentially with a scale height of 54 km, to reproduce the large-scale perturbations observed in atmospheric density. The vertical wavelength was found to decrease linearly with decreasing altitude from 35 km at 270 km to 25 km at 150 km altitude. Their model required wind speeds of less than 0.1 m s^{-1} in this region. That study noted how the observed structure remained coherent over horizontal distances of 1200 km during the occultation, and that the Rossby waves could exist simultaneously with internal gravity waves.

The three studies described above did not formulate a forcing mechanism for the observed atmospheric oscillations and the constraints that such a mechanism would require. Both internal gravity waves and Rossby waves are compatible with tidal motions driven by nitrogen condensation-sublimation flows on Pluto, and they also exist as

specific modes in the tidal equations for a thin atmosphere upon a low-gravity planetary body. However, Pluto's small size (~ 1190 km radius), large scale height (~ 50 km), and slow rotation (period of 6.4 earth days) implies a Rossby radius of deformation > 5000 km. This is much larger than Pluto's radius, and should suppress synoptic scale meteorology (Holton 1992, Bertrand *et al.* 2019b). The first modeled forcing mechanism for observed atmospheric waves in Pluto's atmosphere included Nitrogen diurnal sublimation and condensation forced by diurnal heating (Toigo *et al*. 2010). That study found that these mechanisms induced vertical velocities near the surface of 2.7 cm s^{-1}. The summation of all the tidal modes for gravity waves contributed the strongest PSD signals around 8 to 12 km vertical wavelength. The sum of the modes was found to contain amplitudes strongest between -30 and +30° latitude.

After the NH flyby of Pluto returned new, highly detailed information about the planet, another forcing mechanism—the perturbation of flow over topography (orographic gravity waves)—was proposed (Gladstone *et al*. 2016). Surface winds on Pluto are expected to be less than 5 m s^{-1} (Forget *et al*. 2017). Substantial topography was also discovered on Pluto, with mountains reaching heights > 3 km (Stern *et al*. 2015, Moore *et al*. 2016, Schenk *et al.* 2018). The combination of the predicted winds and observed topography show that gravity waves can be triggered by flow over topography (Cheng *et al.* 2017). Temperature and pressure profiles derived from the radio occultation experiment (REX) instrument on NH show no evidence of gravity wave induced temperature and pressure perturbations, therefore suggesting weak perturbations—specifically temperature perturbations < 1 K (Hinson *et al.* 2017). Additionally, such

weak perturbations are not likely to directly produce layers. Based on these new observations, the visualization of haze layering was proposed to occur through haze particle number density perturbations as described by solutions to the perturbed/linearized continuity equation for haze particles in a gas (Cheng *et al.* 2017).

3.2 Measurements and Methods

In this study three LORRI image sequences were selected in which we investigate altitudes, geographic locations, and resolutions where haze layers were superimposed on the observed haze profile. The highest resolution LORRI image comes from image sequence P_HIPHASE_HIRES (hereafter HIRES). The exposure time for this image was 10 ms with a resolution of 0.93 m pix^{-1} and this image was analyzed for fine scale haze layer characteristics below 60 km. LORRI image sequence P_MULTI_DEP_LONG_1 (hereafter P_MULTI) contains images with an exposure time of 150 ms and a resolution of around 0.96 km pix^{-1}. This image sequence was analyzed by constructing a 6-image mosaic that was then "unwrapped" using a Cartesian to polar coordinate transformation so that image columns correspond to radial profiles. Image sequence P_LORRI_FULLFRAME_DEP (hereafter FULLFRAME) consists of 3.85 km pix^{-1} resolution images with an exposure time of 150 ms. This image sequence was chosen to explore larger scale layering variations and to produce a more global picture of haze layer structure that might be associated larger scale processes such as planetary waves. Important parameters for the three image sequences analyzed are summarized in Table 4.

Subsequent sections follow the order in Table 4—with the P_MULTI sequence most complete in resolution and coverage, and the FULLFRAME and HIRES sequences each having their shortcomings of lower resolution and spatial coverage, respectively. Data analysis was conducted on LORRI Level 2 processed images (2D data numbers (DN)).

Table 4: Summary of image sequences at high phase angle considered in this study of visible haze layer structure at multiple scales and resolutions.

Observation Sequence	Start Time (UTC)	Time to Closest Approach (hrs.)	S/C Distance to Pluto (km)	Exposure Time (msec)	Resolution (km/pix)	Solar Phase Angle (deg)
P_MULTI_DEP_LONG_1 (P_MULTI)	7/14/2015 15:42	3.78	193,342	150	0.96	169
P_LORRI_FULLFRAME_DEP (FULLFRAME)	7/15/2015 03:26	15.61	775,278	150	3.85	165
P_HIPHASE_HIRES (HIRES)	7/14/2015 12:04	0.24	18,758	10	0.093	148

The HIRES sequence was analyzed by extracting a single profile. Geographic locations along the limb in the image are indicated with red crosses in Figure 52. Striping artifacts due to the low exposure time are visible throughout the entire profile, so that a smoothed profile (using a boxcar average and width of 9 pixels) was calculated in order to isolate structure on the radial scale of layers as observed in the other two image sequences while reducing higher frequency noise. A waveform of the haze layers was then calculated by

subtracting an exponential fit to the haze profile. This waveform was then used to calculate power spectral densities (PSDs) for unprocessed and processed profiles and to look for persistent signals (peaks in power). A Hann window filter was chosen and applied to the data to minimize aliasing and leakage to side lobes, as described in Press *et al*. (2003).

The P_MULTI sequence used row averaged profiles calculated for the unwrapped image and subtracted to remove an approximate exponentially decaying background trend. However, considerable variations in the shape of this trend motivated the focusing on three individual local regions instead of one (referred to as P_MULTI R1-3) for a more effective background subtraction. The resulting waveforms were then used to calculate PSDs, both with and without Hann windows, as described for HIRES. A Sobel edge filter was applied to the mosaic to bring out layers (Cheng *et al.* 2017). Slopes were then extracted from this image for comparison to models of vertically propagating atmospheric waves. The image mosaic with the frame locations is shown below in Figure 51.

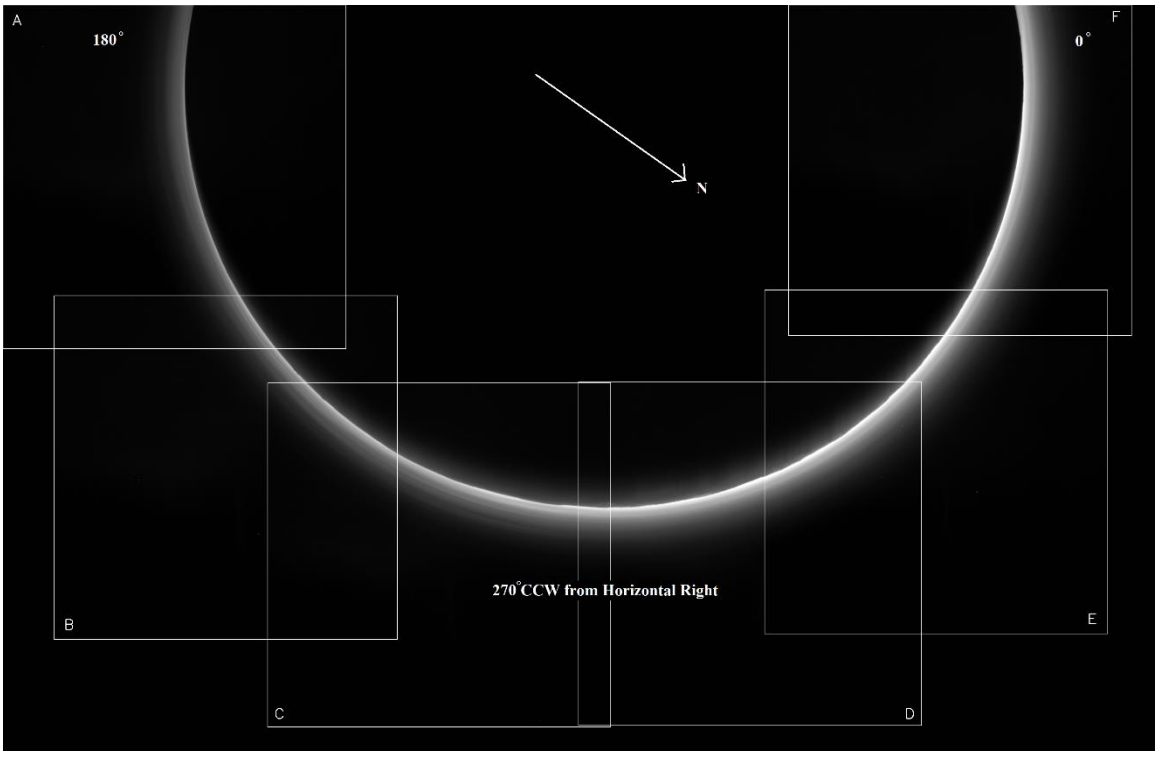

Figure 51: Mosaic of all 6 unique FOV images within the P_MULTI sequence showing clock angle locations (red text) and frame boundary positions, with labels A-F for reference in the text where the unwrapped features are discussed. Image frames B and C (indicated by blue and orange diamonds in Figure 52) contain the most numerous and distinct layers for this sequence. Pluto North direction is shown, and the south pole is just outside the top of mosaic. Clock angles are indicated for reference and are measured counter-clockwise (CCW) from the mosaic top right corner (noted in unwrapped Figure 53 and Figure 54).

The FULLFRAME image sequence was used to estimate how well LORRI resolved layering on the vertical scales identified in P_MULTI and HIRES, as well as to search for changes in the layering around the disk (globally and geographically). The same procedure was used to extract waveforms and PSDs as in P_MULTI, but in this case only one image was unwrapped, which was then split into two halves—dayside and nightside. Here dayside and nightside are defined as data sampling that lies on either the dayside or nightside of the terminator (although haze as seen by NH/LORRI was illuminated for

both dayside and nightside at higher altitudes) as shown in Figure 52. Although large changes in solar flux and diurnal forcing are not believed to occur across the terminator, large day-night haze brightness gradients were in fact observed, likely due to the difference in sampling dayside vs nightside (more or less LOS sampled volume elements being illuminated by the sun). The geographic locations below tangent altitudes for the three image sequences are plotted in Figure 52. The geographic locations below radial

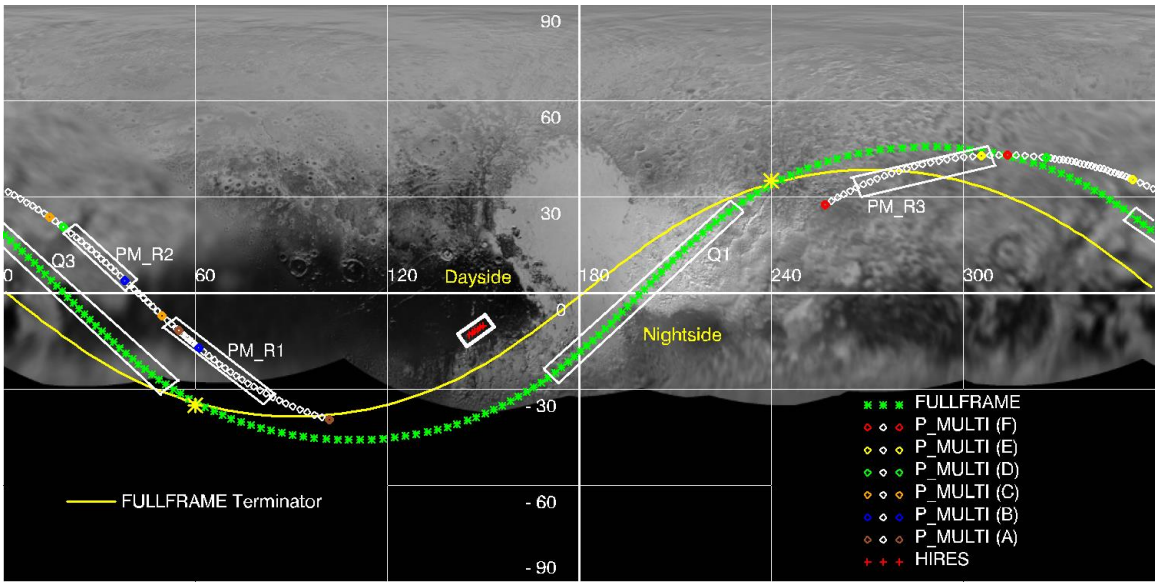

Figure 52: Limb traces for the three LORRI image sequences superimposed on an unwrapped cylindrical base map projection of Pluto's surface (Schenk et al. 2018). Note the relatively consistent latitude extent for the P_MULTI and FULLFRAME sequences, with an approximately 20˚ longitude shift in limb region sampled. Each color symbol for P_MULTI corresponds to a different image frame boundary in the sequence and have considerable overlaps. The terminator location during the FULLFRAME sequence is indicated with the dayside and nightside defined. FULLFRAME quadrant locations and P_MULTI region locations further analyzed in the following section are indicated.

profiles extending outward from the limb are approximately constant. These locations are important because the largest contributions to image brightness originates at or very near

the tangent altitude so that these locations provide information on geographic variations in haze layer structures.

Three regions were then extracted for dayside and nightside, and waveforms and PSDs calculated. Variation in haze layer structure was investigated around the limb by constructing a 4-image stack (4-images aligned with pixel-by-pixel sum) and then applying a Sobel edge filter to the image stack. Layer tilt was identified in quadrants 1 and 3 of this image stack, and these regions were used to calculate the slope orientations and magnitudes. Comparisons between these slopes and those found in P_MULTI, as well as with other features in these sequences are discussed below.

3.3 Results

3.3.1 P_MULTI Haze Layer Characteristics

A little over half of Pluto's limb was observed in P_MULTI, starting toward the North pole and swinging around clockwise toward the South pole as shown in Figure 51, with letters A-F corresponding to Figure 52 legend letters and frame locations. This image sequence mainly covers the half of Pluto's disk facing the sun (hereafter referred to as dayside). Clock angles are specified for three locations around the limb and are used as reference angles for the unwrapped mosaics that follow. Frames B and C in Figure 52 indicate the equatorial/low latitude region where layering was found to be most numerous and distinct in Cheng *et al*. (2017). For these images, larger vertical scale layers are seen to be embedded with finer-scale layering, which provided the motivation to extract PSDs

of all unwrapped image sequence columns (radial profiles) and explore the superposition of multiple signals.

The unwrapped mosaic from Figure 51 is shown in Figure 53 with overlaid limb geography (equator and 0 longitude marked) using a scattering program as discussed in the companion study. Tangent altitudes extend up to ~200 km, with horizontal distances and clock angles indicated below the limb. The more numerous and distinct layering occurs over the geographic region informally referred to as The Tail of Cthulhu Regio.

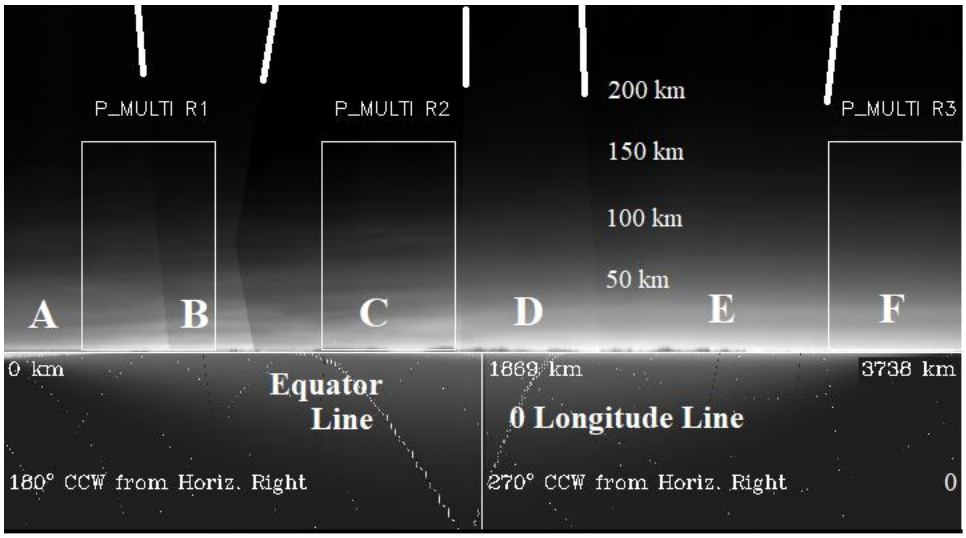

Figure 53: Unwrapped LORRI image mosaic from the P_MULTI sequence, with the locations of regions P_MULTI R1-3 identified. Pre-whitening was done by subtracting the regional row averages from the columns to generate waveforms, and PSDs were then extracted. Frame borders are indicated at the top with bold white lines corresponding to the frame letters A-F defined in Figure 52. Moving left-to-right from A-F corresponds to moving from east to west in longitude (again, see Figure 52).

Regions P_MULTI R1-3 isolated for background subtraction are shown in Figure 53, with borders corresponding to the columns and rows used. P_MULTI R1 corresponds to

southern low latitudes (~ 30-10° S), P_MULTI R2 to the equatorial region and northern low latitudes (~ 0-20° N), and P_MULTI R3 to the highest northern latitudes (~ 30-45° N). The region images produced after row average normalization are shown below in Figure 54.

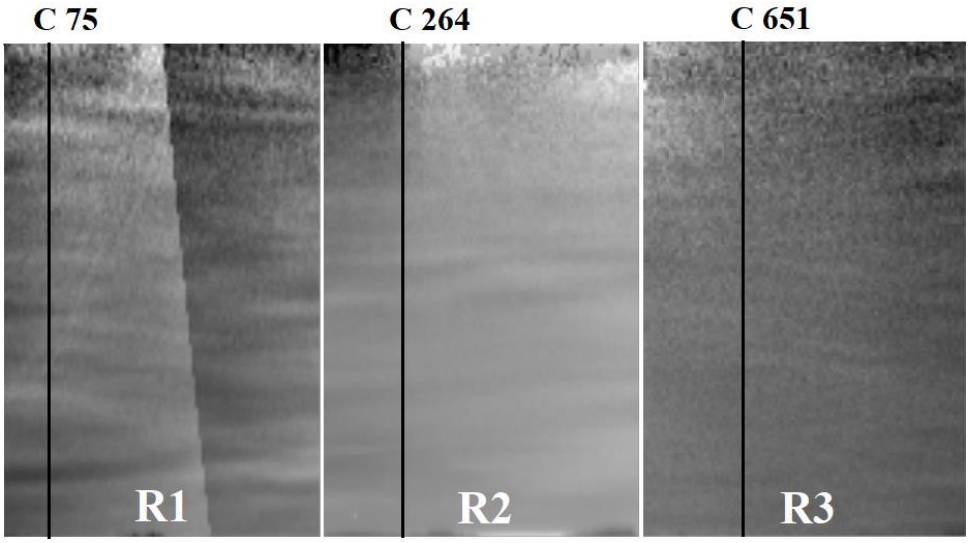

Figure 54: Enlarged regions selected from the P_MULTI mosaic in Figure 53. Layers exhibit both positive (increasing in altitude moving right or toward the west) and negative slopes (decreasing in altitude moving right) in P_MULTI R1, with more consistent positive slopes in P_MULTI R2. Layers in P_MULTI R2 also appear to be less numerous and of larger wavelength. P_MULTI R3 layers have considerably smaller amplitudes. P_MULTI R1 contains a seam between two frames (A and B). P_MULTI R2 contains frame C and P_MULTI R3 contains frame F in Figure 53. The locations of the three examples of columns that were extracted to generate waveforms and PSDs are indicated by the vertical solid lines.

Most notable are the cross-hatching patterns apparent in P_MULTI R1 and P_MULTI R3 (alternating positive and negative layer slopes) as opposed to P_MULTI R2's more consistent positive layer slopes.

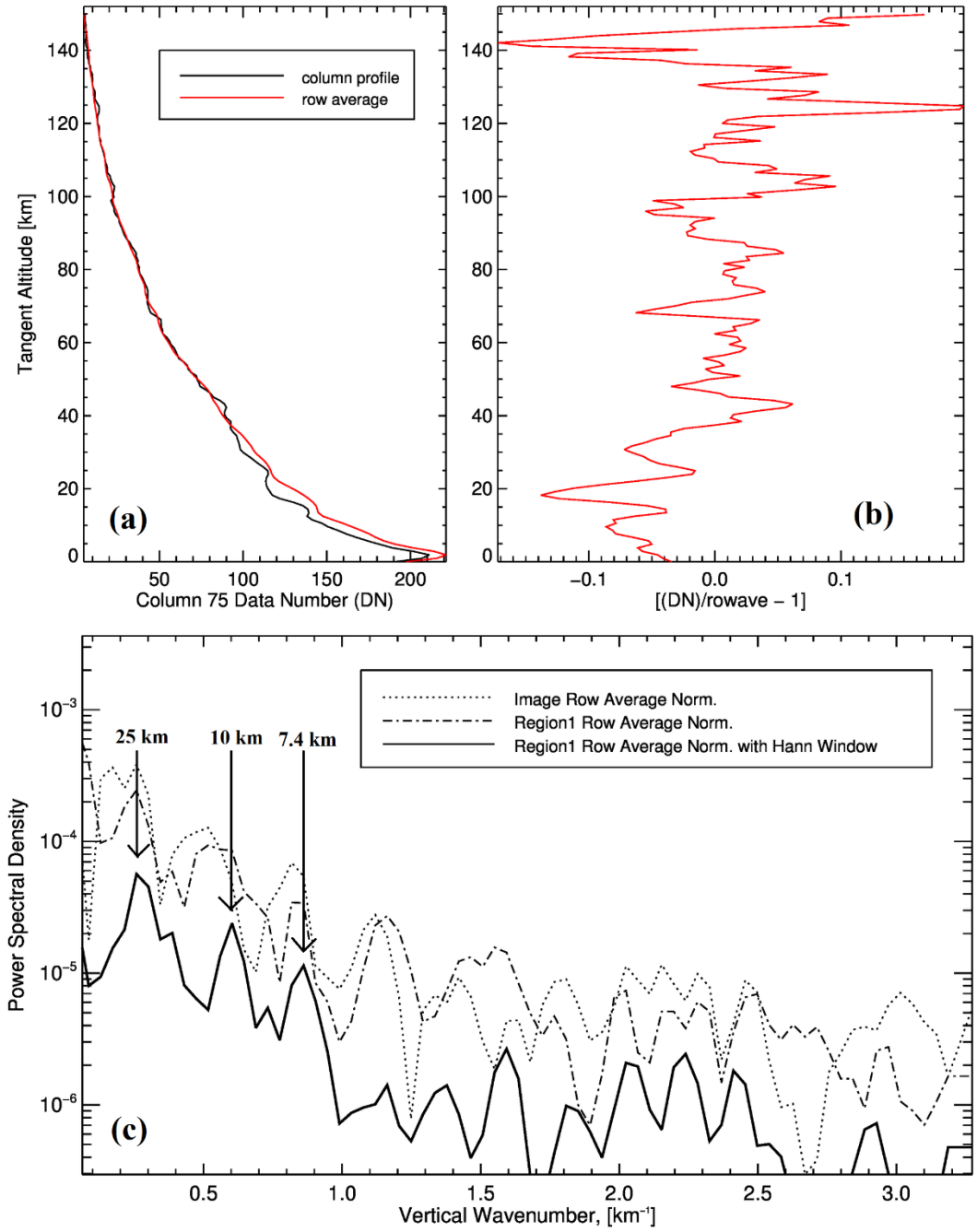

Figure 55: (a) P_MULTI R1 row average and Column 75 profiles (within columns 60-160 in Figure 53 image, profile around Latitude 30S and Longitude 80), (b) the row average normalized waveform showing both large and small scale oscillations, and (c) the corresponding PSD showing a low frequency peak around 0.25 (25 km), a middle peak around 0.6 (10 km), and a third peak around 0.85 (7.4 km). The PSD after application of the Hann Window is shown in red. The three indicated peaks are persistent in power and location between processing steps, but the peaks beyond wavenumber ~1 km^{-1} appear to be less significant due to the loss of power after using the Hann window (taking into account window function effects) and an inconsistent presence between other image columns.

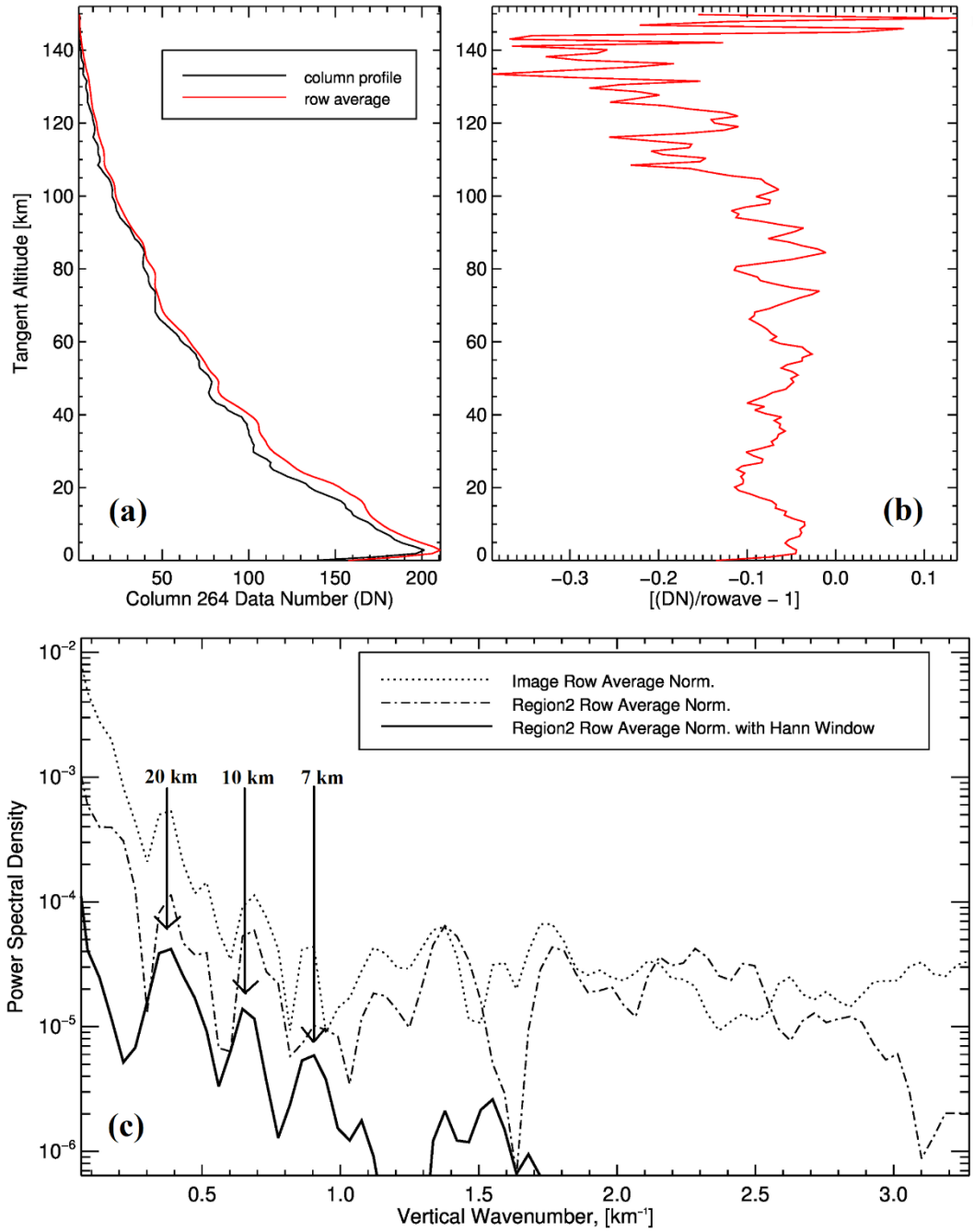

Figure 56: Same as Figure 55 but for P_MULTI R2 (column 264 in range 240-340, profile from around Latitude 10N and Longitude 40). Most distinct here is the ~ 20 km wavelength peak in waveform and spectrum, with a 10 km wavelength peak of comparable power. The row average profile contains some features consistent with the column profile that may act to decrease the power of the 20km signal. The large variation above 120 km altitude is likely the cause of increasing power at the lowest wavenumbers.

Three signal peaks are observed—25 km, 12 km, and 8 km in vertical wavelength ($\lambda_z = 2\pi/m$), with vertical wavenumber (km^{-1}) plotted. The 25 km peak can be seen in the waveform to be embedded with smaller scale oscillations (e.g. the 12 km peak). The P_MULTI R1 column range (60-160) for the mosaic corresponds to latitudes of around 10-25° S. Power decreases toward lower wavenumber with consecutive processing steps, indicating more effective background trend subtractions (the amount of processing is usually sufficient when power levels off moving toward low wavenumber). Peaks also become more isolated after application of the Hann window. Similar peak locations were observed in P_MULTI R2 corresponding to northern latitudes of around 15-25° N, displayed in Figure 56.

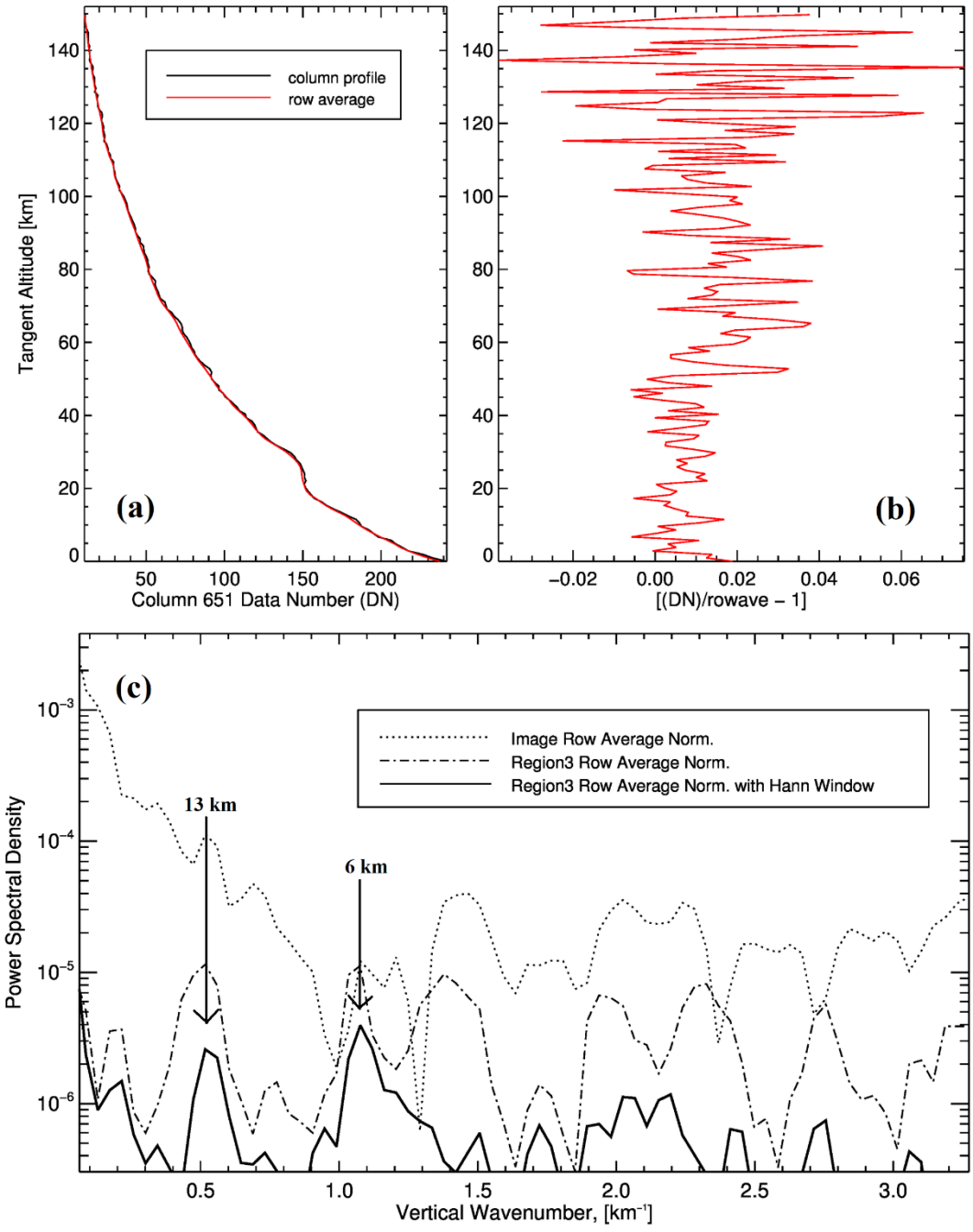

Figure 57: One of P_MULTI R3's clearest cases (column 651 in range 620-720, around Latitude 40N and Longitude 290) isolated with lower power in the area where layering is not as visible and layer amplitudes have considerably decreased relative to background values.

The 20 km and 10 km vertical wavelength peaks were the most consistent across P_MULTI R2 columns. Waveform amplitudes could be considerably decreased here due to the region's row average profile exhibiting oscillations consistent with the individual column profile (region trends consistent with and normalizing out individual profile oscillations). Therefore, the difference in the profiles (background subtractions) will reduce or flatten waveform oscillations that are level with the surface. A large decrease in layer amplitudes occurred for P_MULTI R3—visible in Figure 53. This decrease in amplitude is also shown in Figure 56 top left and right, resulting in PSDs with lower power and peaks throughout the region that are much less consistent. One of the clearest examples of signals is shown in Column 651 (within 620-720 in Figure 54, corresponding to northern latitudes of around 30-45° N), with the finer scale layer peaks much more sporadic and a longer period peak completely absent. A slight increase in power toward low wavenumber was common to spectra extracted for all image sequences. This is likely due to remaining long period trends in profiles even after background subtraction.

The P_MULTI background subtracted spectra confirm a longer vertical wavelength (around 20-25 km) combined with a shorter vertical wavelength oscillation (around 10-12 km). The absence and/or decrease in strength of these peaks in P_MULTI R3 is not only due to the more distinct layering existing at low latitudes and in equatorial regions (as was found in Cheng *et al.* (2017)), but is also a result of layering exhibiting higher consistency from column to column (more level/flat layers). These perturbations then get subtracted from the profile and waveform. The best example of this is the layer located at around 25 km altitude in Figure 57 top left, which is also one of the brightest

layers in the right half of the mosaic in Figure 53. The correlation between numerous sloped layers terminating at the location of the emergence of this layer (and other level layers with an apparent larger vertical scale) is important to note and will be discussed in the following sections. Layer amplitudes generally ranged from 0.01-0.05 in this image sequence.

In addition to haze layer spatial variations, amplitudes, and PSDs, layer slopes (relative to the limb) were extracted from these images. Many layers in the P_MULTI mosaic exhibit considerable tilt, and this analysis highlights them. The Robert's filtered image mosaic from Cheng *et al.* (2017) is shown in Figure 58, with frame labels and edges (A-F), as well as slope locations (1-9) that were extracted from layers that exhibited considerable tilt.

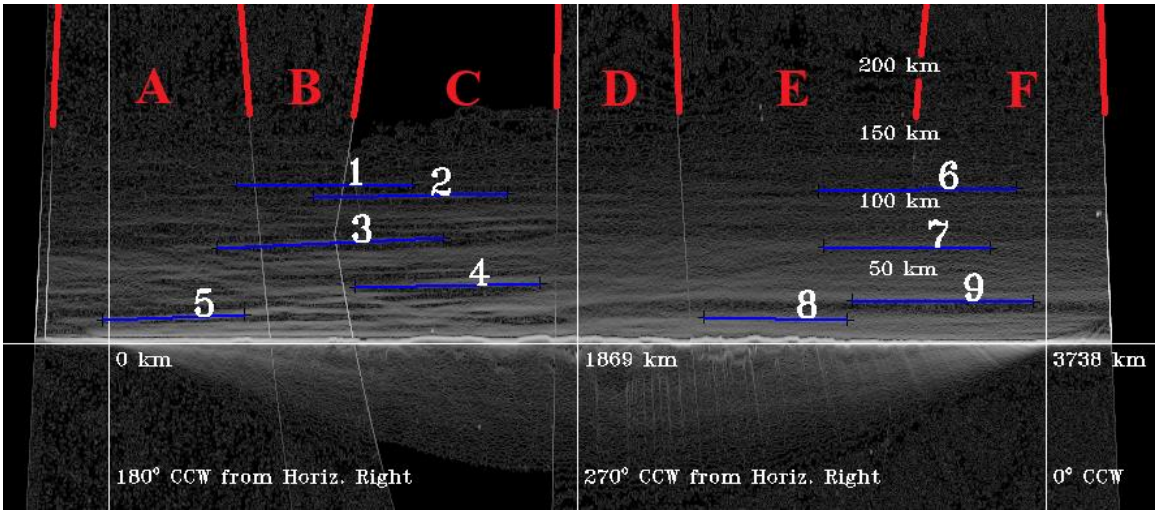

Figure 58: LORRI mosaic with haze layer slope extraction positions, frame boundary locations and labels (red lines and letters) corresponding to Figure 52 frame positions. Slope values of the layers are shown in Table 5. In the left half of the mosaic the layering is more intense, and they exhibit larger tilt, with predominantly positive slopes over equatorial and low latitude regions (see Figure 51 and Figure 53). For this reason, slopes 1-5 were averaged for further comparisons as discussed in the text.

The observed layers are dominated by a positive tilt between clock angles of 180-270°, followed by a leveling-off trend and slight negative slope toward a clock angle of 0°. Slope values (km/km) are summarized for the corresponding numbered layers in Table 5. Tilted layers may be an indication of specific types of atmospheric motions, as for example, vertically propagating waves.

Table 5: Slope values corresponding to the layer location numbers labeled in the P_MULTI mosaic of Figure 58. Slopes/layers 1-5 located between 180-270° are averaged and provide a positive slope value where layers are most distinct and exhibit the largest amount of slope relative to the limb.

Layer Number	LORRI slopes [km/km]
1	0.007
2	0.021
3	0.046
4	0.021
5	0.037
6	0.013
7	-0.008
8	-0.018
9	-0.007
Average (Positive Slopes in Most Distinct Area)	**0.026 (1-5)**

3.3.2 FULLFRAME Resolved Structure and Global Variation

Figure 59 shows a 4-image stack of Pluto's entire disk with the Sobel edge filter. Two quadrants, numbered 1 and 3, were further examined since the layers they reveal were found to have a very large tilt relative to the limb. Quadrant 4 (Q4) contains layers that are level compared to the limb. The majority of Quadrant 2 (Q2) remains in the

nightside (within Pluto's shadow) preventing reliable extraction of layer characteristics. The appearance and disappearance of a layer around 25 km tangent altitude is marked with white circles and coincides with the two areas outside the circles that contain layers exhibiting tilt. Both regions contain tangent altitudes above low latitude/equatorial regions (see Figure 52). Quadrant 3 (Q3) extends over the same latitude range as P_MULTI (specifically P_MULTI R1 and P_MULTI R2, with around 20° longitude offset between them) and can be used as a more direct comparison between the observed haze layer structures.

Figure 60 (top) shows the unwrapped disk and the locations of quadrants Q1 and Q3. The latitudinal boundaries of the low altitude layer are now shown by the white arrows. Below the unwrapped, Sobel edge filtered image stack is a plot co-locating the layer features with tangent altitude latitudes and longitudes (column numbers shown at the boundary between image and plot). Here the 25 km layer is observed to occur only at latitudes > 30° N. Layers appear to contain only negative slopes in Q1 and positive slopes in Q3 (see Figure 60, Figure 64, and Figure 65).

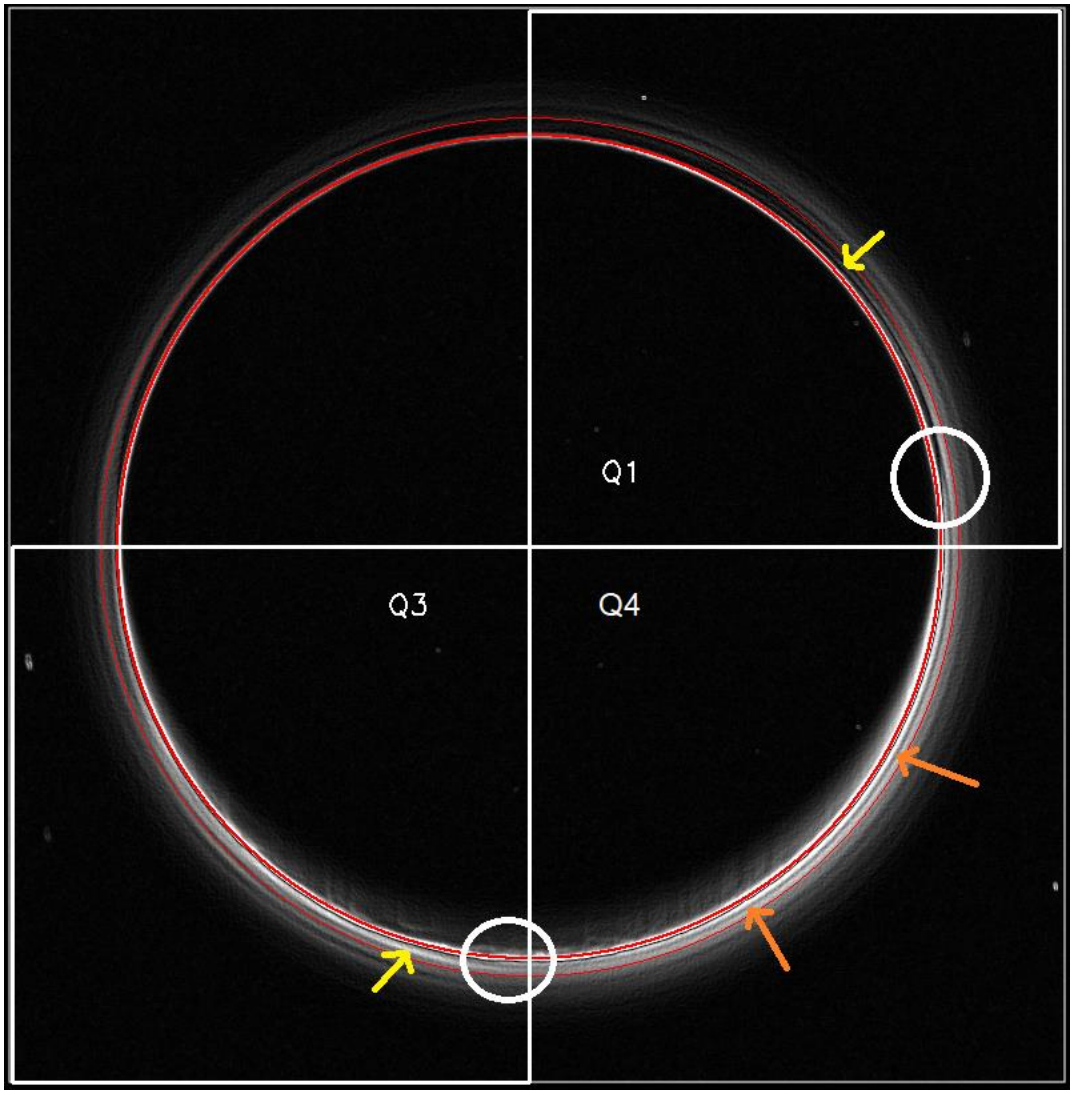

Figure 59: FULLFRAME 4-image stack with Sobel edge filter. Two quadrants were explored, Q1 and Q3, for layer slopes and structure comparisons with P_MULTI. The red concentric circles are applied to indicate the sloping of one layer in each quadrant between the circles (yellow arrows). Also indicated are the locations (white circles) around the limb between which (in Q4) a near surface layer (indicated with orange arrows) is visible toward northern latitudes—its boundaries coincident with regions where layers slope upward or down.

The brightest feature in Q3 lies at the edge of a dark layer coincident with the 25 km altitude layer in P_MULTI R3 (Figure 57). This feature can also be matched with the

dark layer that appears to rise to a constant altitude from mosaic center to left half of Figure 58 in P_MULTI.

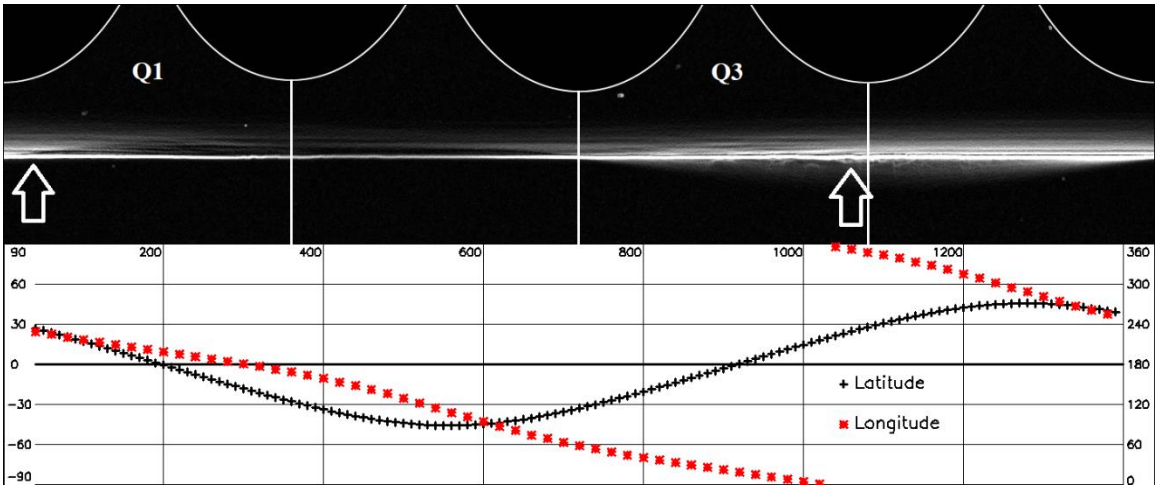

Figure 60: (Top) The unwrapped, 4 image stack FULLFRAME image with Sobel edge filter applied and Q1 and Q3 shown. Also indicated are the boundaries of a northern latitude layer whose start/end points correspond to the region where layering is most visible and exhibit some degree of tilt. **(Bottom)** Plot of latitudes (black) and longitudes (red) below tangent altitudes for each of the unwrapped image columns.

The locations of three regions taken from the dayside and nightside are displayed in Figure 61 top-right and top-left, respectively. Corresponding geographic regions at and below the limb are shown in Figure 61 bottom, with the region names above where the equator intercepts the limb. The dayside half of the unwrapped image is seen to coincide with the left boundary and rightmost image boundary of Q3 in Figure 60.

The existence of a larger scale oscillation consistent with that observed in the P_MULTI sequence with a vertical wavelength around 20-25 km was observed. Peaks below ~15 km appear less consistent and approach the Nyquist frequency/wavenumber of 0.815 km^{-1} (7.7 km wavelength) The lower resolution in FULLFRAME images likely

acted as a low-pass filter on radial brightness oscillations in the images. Peaks in all regions were less consistent and of lower power. The only regions with consistent peaks at a given vertical wavelength for multiple columns were the FULLFRAME dayside R1 and nightside R2 shown in Figure 61.

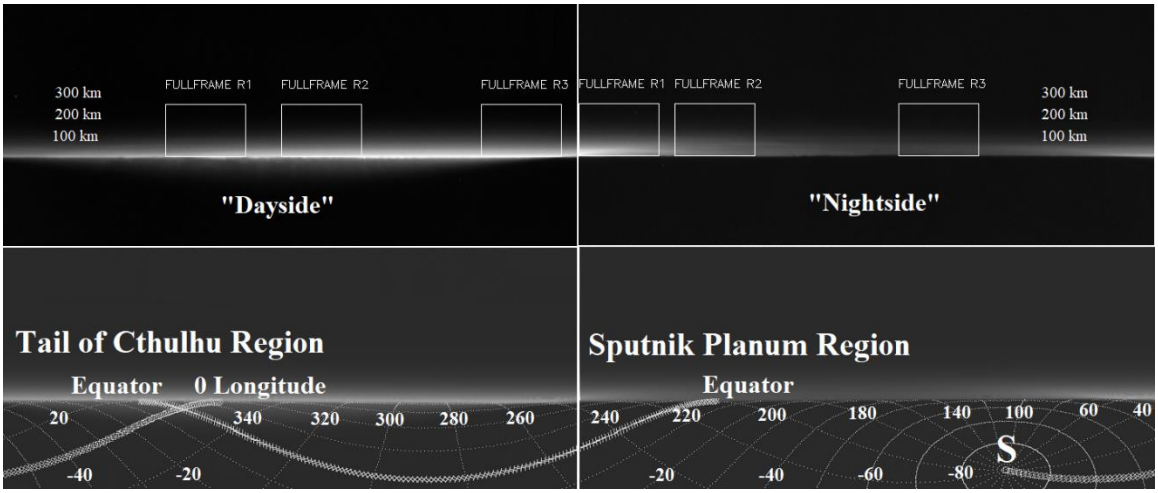

Figure 61: (Left Panel) Dayside half of unwrapped image corresponding to a similar geographic region as that imaged in P_MULTI. Top shows the designated regions in an unfiltered image - bottom the equatorial region below and at limb is labeled. **(Right Panel)** Nightside region where a unique equatorial limb region (the right side of SP) was imaged relative to P_MULTI. Top shows the regions extracted for waveforms and PSDs and bottom the limb geography with SP marked.

The FULLFRAME dayside R1 coincides with the same latitude range (0-30° N) as contained in frames C and D, and overlaps with P_MULTI R2, with a shift to lower longitudes of around 20°. The same vertical profile, waveform, PSD plot structure that was shown for regions in P_MULTI is shown below in Figure 62 for FULLFRAME dayside R1. Three signals are shown corresponding to vertical wavelengths labeled in the bottom PSD plot. The peak around 0.35 km^{-1} is most consistent with the strongest signal in P_MULTI R2.

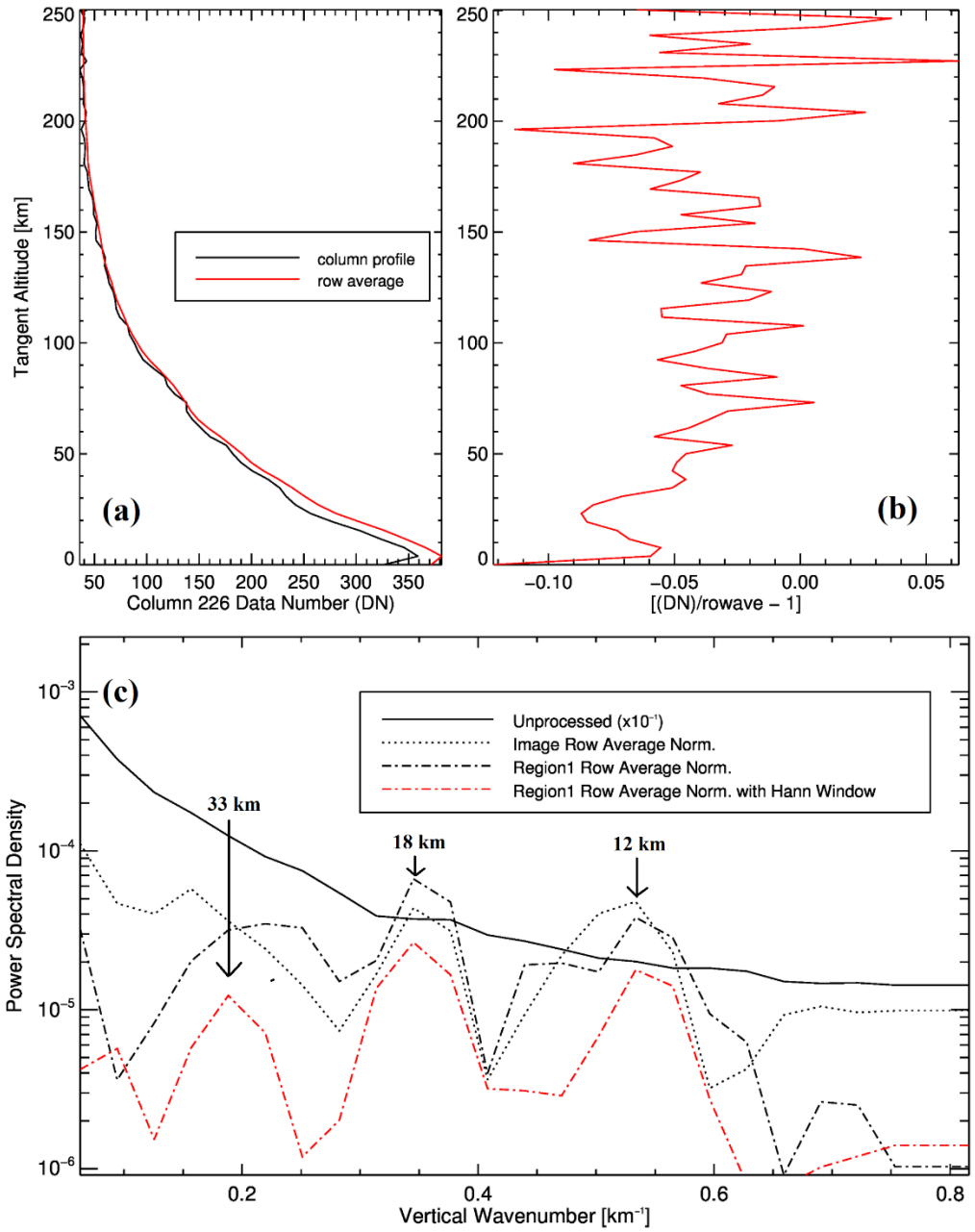

Figure 62: FULLFRAME dayside R1 205-305, column 226. **(a)** The column and row average profiles. **(b)** The row average normalized waveform showing most visibly vertical wavelengths around 20 km and 10 km. **(c)** The PSD confirms the visible wavelength as well as a signal ~ 0.2 km^{-1}. The signal ~ 0.35 km^{-1} is most persistent in the same region columns and agrees with the strongest signal in P_MULTI R2—an overlapping region in latitude.

FULLFRAME nightside R2 profiles, waveform, and PSD is shown in Figure 63. This region is unique geographically relative to the P_MULTI sequence and was sampled above the Sputnik Planum (SP) area. Here it is important to note that although the regional background normalization technique performs well above 70 km, and in general fits the effects of dimming due to Pluto's shadow below, some features (around 50, 30, and 20 km altitude) are consistent in altitude across the entire region and are partially subtracted out (waveform amplitude decreased at right, as was noted in the P_MULTI - Figure 56 profile). This likely decreases the power of the 40 km and 22 km signals. Regardless, these signals are visible in the waveform and PSD, with the 22 km signal most consistent with larger scale oscillations observed in other regions. Layer amplitudes generally ranged from 0.01-0.04 for this image sequence.

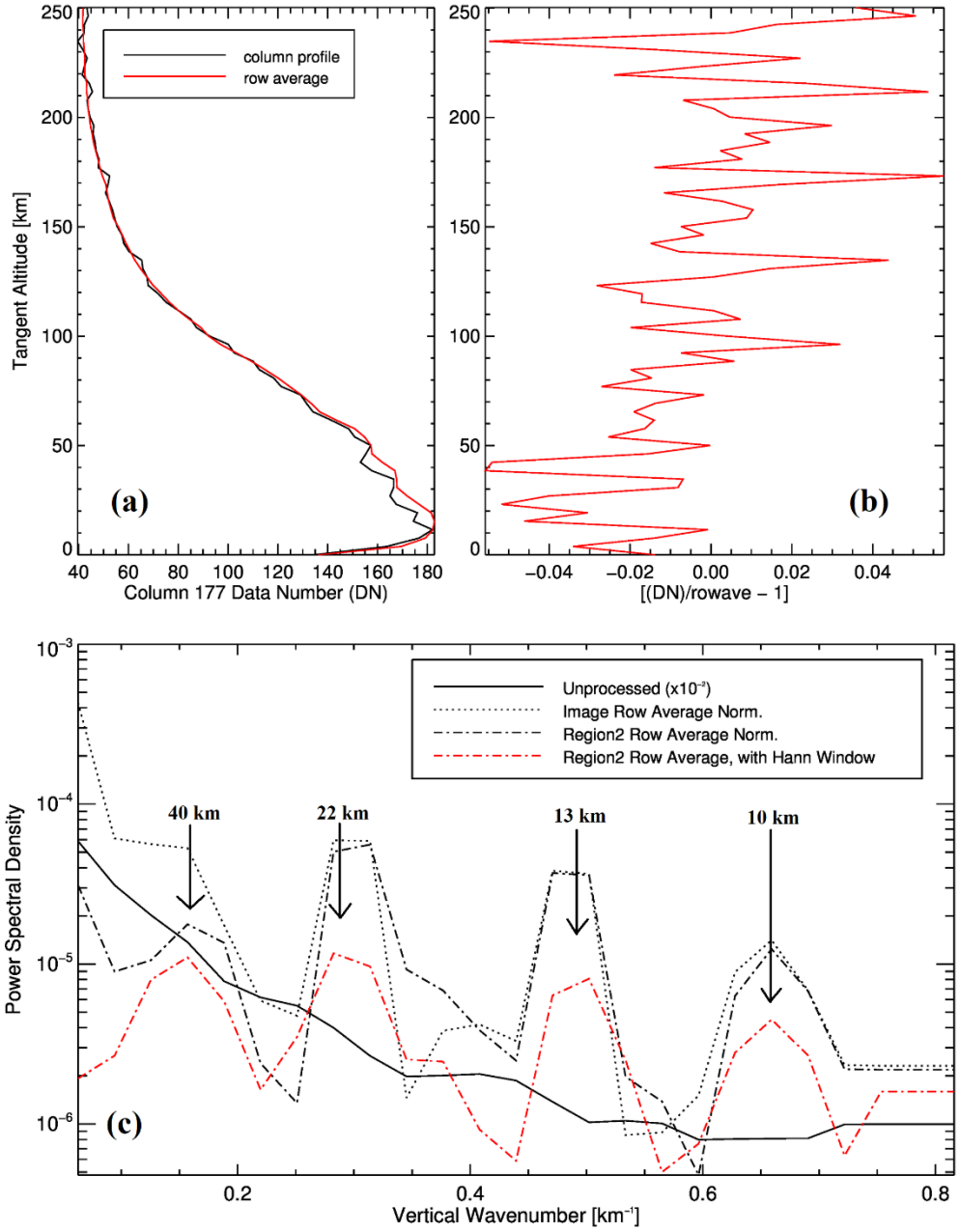

Figure 63: FULLFRAME nightside R2 120-220, column 177. **(a)** Profiles and **(b)** waveforms showing large scale oscillations. **(c)** PSDs showing persistence in all peaks with each additional background normalization technique as well as application of the Hann window. The 22 km signal is most consistent with the dayside large-scale peak, and the 40 km is visible in the waveform, especially for higher altitudes. The 13 km and 10 km peaks approach the Nyquist wavenumber of the image (0.815 km^{-1}, corresponding to a wavelength of 7.7 km).

Both the FULLFRAME dayside R1 and nightside R2 imagery contained bright layers with large enough slope (on either side of the 25 km altitude, higher latitude feature) to be extracted and compared with the P_MULTI sequence. Figure 64 shows the negatively sloped layers located above SP (marked as Q1 in Figure 52). The top panel shows the Sobel edge filtered image where the scale has been adjusted to make the layer edges brighter. The bottom image shows where slopes were extracted, and the FULLFRAME nightside R2 profile shown in Figure 63 intercepts slope 2.

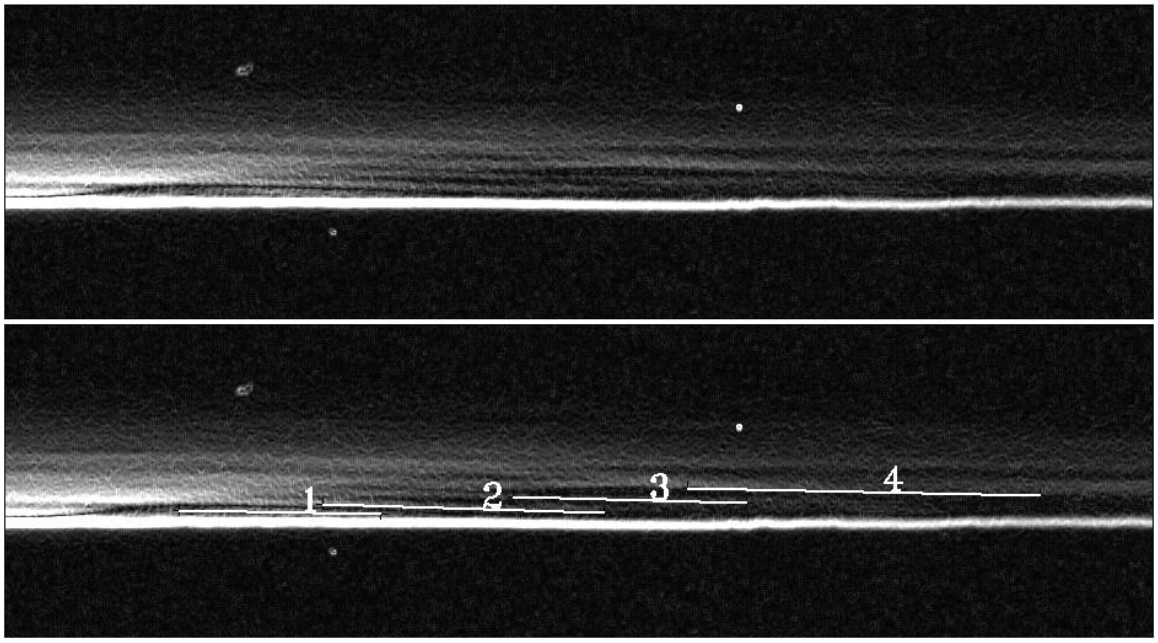

Figure 64: Quadrant Q1, with some portion of Q2 at right, from Figure 60. Edges of layer locations where slopes were extracted are shown at bottom. The degree of slope for all the edges/layers is consistent between layers and across the limb region. The average slope value was -0.025, with specific values shown below in Table 6. Although the opposite sign, these slopes are in good agreement with the average slope obtained for the P_MULTI sequence, 0.026.

These layers contain slopes of opposite sign but of consistent magnitude with the average of the slopes found for 5 layers in the left side of the P_MULTI mosaic (Figure 58). FULLFRAME dayside R1 zoom is shown in Figure 65 (top) and layer edge positions where slopes were extracted at bottom. The profile shown in Figure 62 intercepts slope 2 here. The three slope values (average of 0.03) also agree with the slopes in P_MULTI. The brightest edge and largest slope, slope 1, corresponds to one of the two edges that rise from close to the surface in Figure 58, and on either side of a dark lane that levels out around 25 km. This altitude is known to correspond to Pluto's temperature maximum. It is important to note the differences in layer structure here compared to the P_MULTI R1 and R2 regions with the same latitude range but a 20° longitude offset.

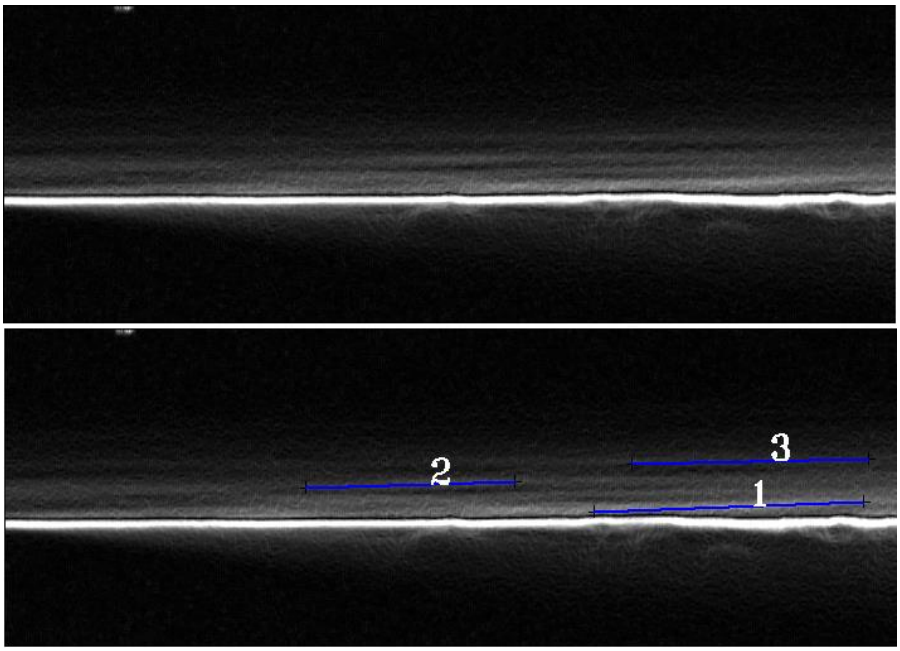

Figure 65: (Top) FULLFRAME dayside Q3 containing FULLFRAME dayside R1 analyzed above. **(Bottom)** Slope extraction locations are indicated, with the profile data shown in Figure 62. Layers have positive slopes with magnitudes consistent with FULLFRAME nightside (Q1) and P_MULTI R1 and R2 (also dayside). However, it is important to note the less numerous layers and absence of small-scale layers here when compared to the same latitude range of P_MULTI.

Layers in Figure 65 are much less numerous and appear to contain more consistent positive slopes with the absence of negative slopes. Only the larger scale layers are visible, and a quasi-periodic brightening and dimming occurs along the layers. The absence of distinct small-scale layers (< 12 km wavelength) is likely due to the FULLFRAME's much lower spatial resolution (3.85 km/pix) acting as a low-pass filter.

Table 6: Slopes (pix/pix) for the layers numbered in Figure 64 and Figure 65. Layers do not spatially correspond, and 3 vs. 4 slopes were extracted for Figure 64 vs. Figure 65 limb regions. The slope magnitudes generally agree with those found in P_MULTI.

Layer Number	Q1 LORRI slopes [km/km] (FULLFRAME nightside R2)	Q3 LORRI slope [km/km] (FULLFRAME dayside R1)
1	-0.018	0.037
2	-0.031	0.030
3	-0.026	0.021
4	-0.021	N/A

3.3.3 HIRES Low Altitude Layers

High resolution, low altitude (around 0-60 km) layers were inspected in the HIRES image sequence as in Figure 5 of Cheng *et al*. (2017). The LORRI image is shown here in Figure 66, with the location where a radial profile was sampled. A persistent surface layer observed around Pluto's limb described as descending from 5 to 3 km and having a thickness of 1-3 km that is also observed in MVIC images is visible (Cheng *et al.* 2017). At least three other layers are distinguishable above that surface layer.

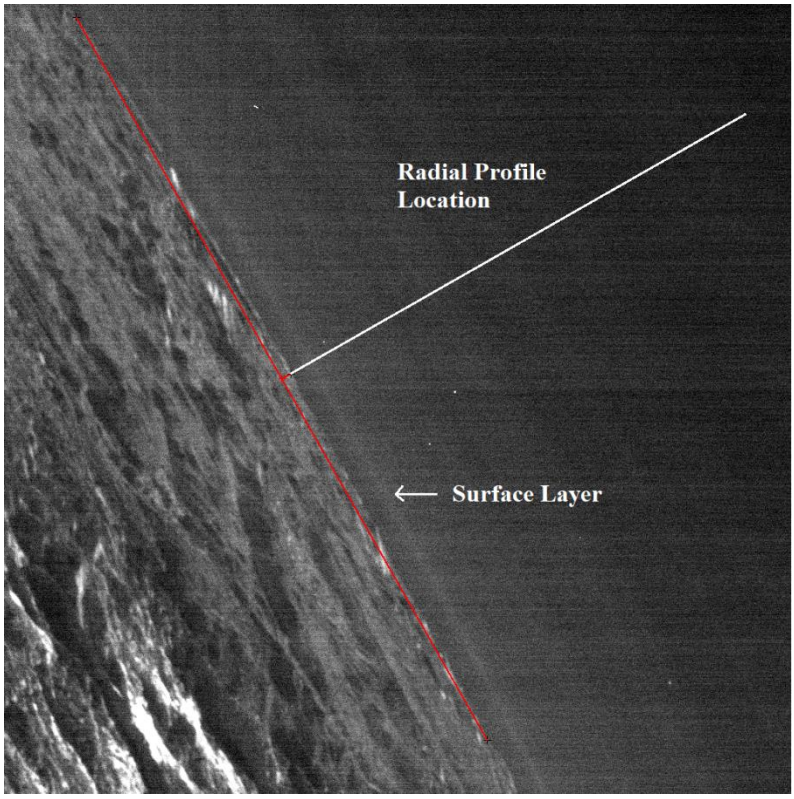

Figure 66: LORRI HIRES image, with markings where a radial profile was taken to extract a waveform and PSD. The surface layer is indicated. This region is shown in Figure 52 to be over the southernmost regions of SP.

The profile for this LORRI image is shown in Figure 67, top left. The thicknesses of the most distinct layers appear to be around 10 km, with a separation between maxima of around the same distance. The surface layer occurs at ~3 km altitude here, with an amplitude above background values of around 0.33. The layer thickness is about 2 km. A large enough altitude range does not exist here for exploration of the larger scale structure (20 km vertical wavelength observed in FULLFRAME and P_MULTI). This image does help show the thickness, number, and amplitude of layers for this low altitude region that could be suitable for future modeling. Perhaps most notable is the increase in amplitude

of the oscillations from just above the surface layer to about 50 km altitude (~ 0.1 to 0.3 from 10 to 50 km, with the entire amplitude range considerably larger than observed for the other two image sequences).

The HIRES PSDs show several peaks, most notably the peak that persists in power with the application of the Hann window at 0.75 km^{-1}. This peak is most consistent with the 6-8 km vertical wavelength signal from the P_MULTI image sequence and the visible layers in the image/waveform. Unfortunately, smaller scale (higher wavenumber) variations and signals could not be differentiated from image striping artifacts.

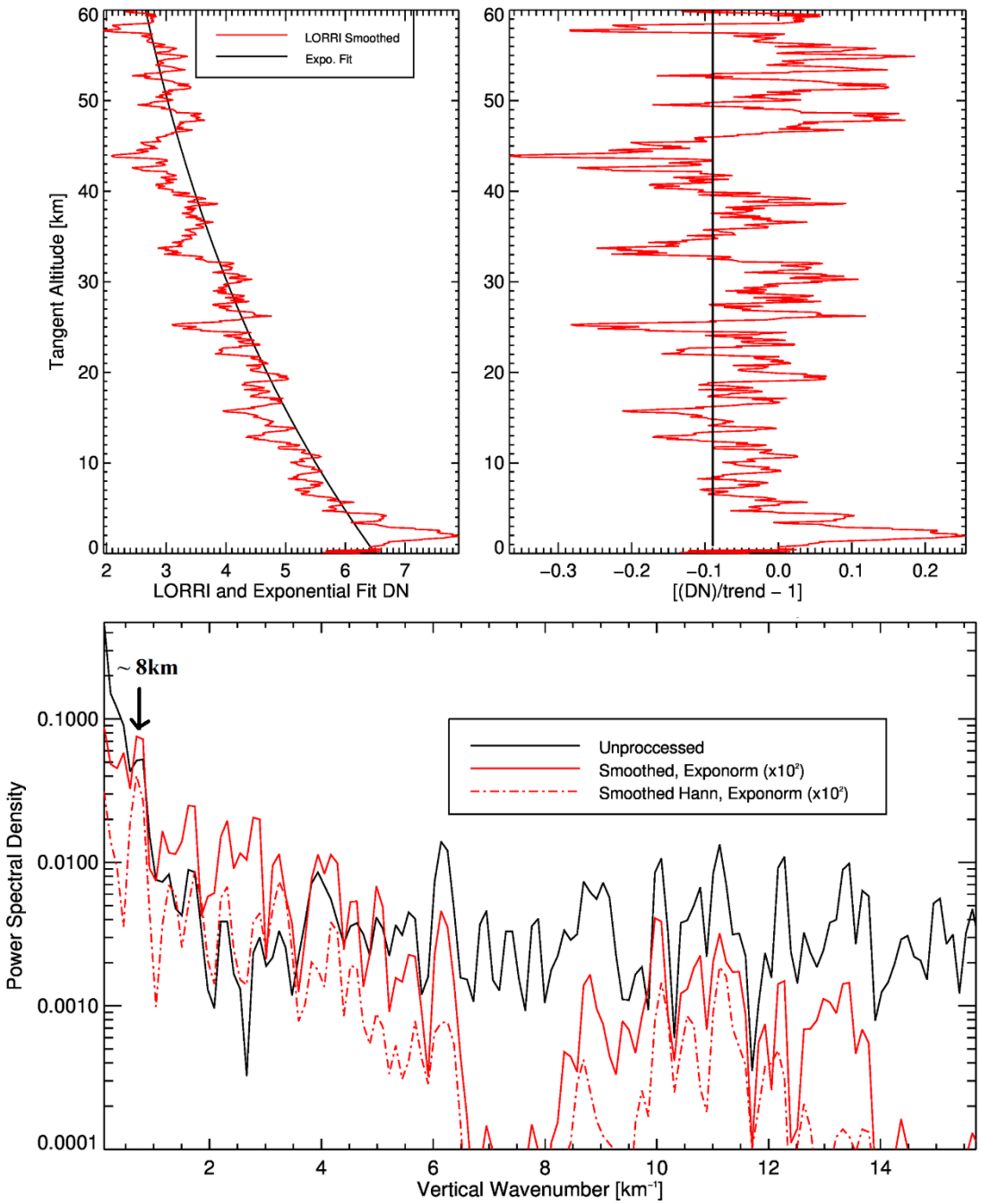

Figure 67: (Top) At left is the smoothed profile extracted from LORRI HIRES image. At right is the resulting trend normalized waveform. At least 3 distinguishable layers exhibiting a 10 km vertical wavelength are visible as well as a surface layer**. (Bottom)** PSDs showing the persistence of several signals through processing. The signal around 0.75 km^{-1} that is in best agreement with a consistent P_MULTI signal around 6-8 km vertical wavelength. A vertical line is placed at top-right to indicate the zero point in oscillations to extract amplitudes.

3.4 Discussion

More than 20 layers were identified in previous studies, which appeared to be more numerous and distinct over equatorial regions/low latitude regions. Haze layers in equatorial regions were difficult to match with layers at northern latitudes except for a near surface layer (3-5 km) and layers at 150, 160, and 170 km altitude (Gladstone *et al*. 2016, Cheng *et al*. 2017). A search for temporal variation in the haze layers altitude was also conducted, with no motion in layer locations detected. The temporal search was conducted over time spans of up to 5.43 hours (Cheng *et al.* 2017).

Three LORRI image sequences at high phase angle were analyzed and reported in this paper. Additional haze layer structure characteristics were extracted that can be identified and/or compared directly with theories and models describing haze layer formation in Pluto's atmosphere due to specific wave generation mechanisms. These characteristics are summarized below in the context of currently proposed wave types and forcing mechanisms.

While the altitude range for the LORRI images used in this study had the best S/N at altitudes between 0-200 km, some consistency between the studies should still exist. The LORRI observed background relative density amplitudes of 0.05 for altitudes of 0-150 km and 20-25 km vertical wavelength in the P_MULTI image sequence are around 5x larger than that predicted by the stellar occultation measurements. By comparison, the FULLFRAME sequence amplitudes of 0.01-0.04, for altitudes 0-250 km at 20 km vertical wavelength are more consistent with the stellar occultation amplitudes. The PSD 18-20 km signal in Hubbard *et al*. (2008) is also consistent with the larger-scale

oscillation in both the P_MULTI and FULLFRAME sequences. A peak below 200 km in the stellar occultation measurements (around 10 km vertical wavelength) is also consistent with those in vertical wavelength with the P_MULTI sequence peaks. In the HIRES sequence, much larger amplitudes of oscillations were observed, in the range of 0.2 - 0.3. Oscillation amplitudes in this image were observed to grow with altitude from around 5 km to the profile extent, 60 km. A PSD peak ~ 8 km vertical wavelength was also identified. The consistency in these signals and their background relative amplitudes further indicates the existence of gravity and/or Rossby waves in Pluto's atmosphere. Taking the average haze layer slope found in this study (~ 0.026 km/km), and two robust peak vertical wavelengths from PSDs of ~ 8 km and 22 km, horizontal wavelengths of around 308 km and 845 km can be inferred (excluding LOS/projection effects).

The adoption of thermal tides as the dominant driving mechanism (Toigo *et al.* 2010) for observed haze layer structure agrees well with LORRI extracted cross-hatching structure (Figure 54, R1), geographic variation (smaller vertical wavelength layer amplitude cut-offs above 30N and 30S determined by combining Figure 52 and Figure 58), and peaks in the PSD at 8 and 12 km vertical wavelength. Toigo *et al.* (2010) predicted the localization of higher perturbation amplitudes to lower latitudes (detailed in their Figure 53 and Figure 54) and the need for this observation (determined here in P_MULTI and in Cheng *et al*. 2017) to support their model.

Three main differences exist between observations and the thermal tides model. (1) There are longer vertical wavelength signals observed in this study (especially in FULLFRAME at all latitudes) associated with a planetary scale feature (25 km altitude

layer indicated in Figure 59) which is not accounted for in their model; (2) perturbations with altitude in temperature are provided but alone do not explain brightness variations—haze particle number density perturbations are likely needed to make comparisons on observed amplitudes (even though gas density perturbations follow $T'/\bar{T} \sim n'/\bar{n}$ to zeroth order); and (3) the model assumes zero mean flow, which may greatly limit the results given the recently calculated Pluto Global Climate model (GCM) zonally averaged retrograde winds approaching 10 m s^{-1} by 40 km altitude (Forget *et al*. 2017, Bertrand *et al*. 2019). The longer wavelength signal may be accounted for in their model with an adjustment in modes due to updating inputs like temperature structure and surface pressure to post-NH values. No statement can be made here on the impact of stronger inferred winds than was originally assumed by Toigo *et al.* (2010), but this could significantly alter the structure of the tides. The tidal model should be re-run with these new inputs and could help explain several observations.

Flow over topography is another way to generate gravity waves and haze layering, a mechanism proposed after the NH flyby (Gladstone *et al.* 2016). An orographic gravity wave model was used to generate haze particle number density perturbations along constant phase lines associated with flow over mountain ridges (Gladstone *et al*. 2016; Cheng *et al*. 2017). An average vertical separation distance between haze layers of around 10 km was matched using a wind of u_0 = 15 cm s^{-1} blowing over 1.5 km high ridges with zonal and meridional wavelengths of λ_x = 160 km and λ_y = 3600 km, respectively. The vertical wavelength was found to be approximately proportional to the wind speed. The relation of these parameters allows the consideration

of this theory with direct comparisons between layer amplitude, vertical wavelength, association with topography/geography, and slope.

Slopes of haze layers generated by the gravity wave model in Cheng *et al*. (2017) have values of around 0.08 km/km for altitudes below 150 km. These slopes are around 2x greater than the slopes reported in this study. However, slope orientation and magnitude can be greatly affected by wind direction and resulting projection effects along the line of sight. This slope value must be viewed as the intrinsic value that is then altered by the observational geometry—e.g. decreased if viewed edge on. Although conditions may exist for this wave type and driving mechanism, orographic gravity waves tend to be localized near their source, within a few 100 km. Very stringent topographic constraints not yet observed on Pluto would have to be placed in order explain the geographic extent of layers observed and outlined in this study—specifically the larger scale (20-25 km vertical wavelength) structure.

3.5 Conclusions and Implications

This study has measured LORRI observed haze layer characteristics in three image sequences important for the comparison with atmospheric wave models and theory seeking to explain Pluto's haze layer structure (e.g. a companion study explores the plausibility of orographically driven gravity waves to explain haze layer structures in Pluto's atmosphere). In the HIRES sequence, layer amplitudes increased from 0.1 to 0.3 from just above a surface layer to 50 km. A PSD peak at ~ 8 km vertical wavelength was identified. This PSD peak was found to be consistent with peaks in the P_MULTI and

FULLFRAME sequences in the range of 8-10 km vertical wavelength. In addition, PSD peaks were identified in P_MULTI and FULLFRAME with the vertical wavelength range of 18-22 km associated with a larger vertical wavelength structure within which finer layers are embedded. Haze layer amplitudes in these to sequences ranged from 0.01-0.04. Sloped layers were found (in the P_MULTI and FULLFRAME image sequences) to be co-located with the boundaries of a 25 km altitude layer emerging and disappearing around 30°N. Slopes on either side of this layer were consistent in magnitude (average of ~ 0.026) but opposite in sign. Inferred horizontal wavelengths of the layer using the average slope and the two vertical wavelengths of 8 km and 22 km are 308 km and 845 km, respectively. This does not take into account projection effects, which will be considered in a companion study.

In the context of our results, several additional developments are needed to facilitate direct comparison and validation of models with the observations.

(1) All models that seek to explain the observed layering need to translate generated atmospheric perturbations into perturbations in haze parameters (number density, size, or shape) to be used in a scattering model that would facilitate direct brightness/image comparisons between modeled and observed layers. Simulated layer amplitudes and slopes could then be directly compared and validated. A companion study will apply this methodology to the orographic gravity wave model layers as well as explore if spatial resolution may have been the main cause of different observed layer structure between the P_MULTI and FULLFRAME observation sequences for the Tail of Cthulhu region.

(2) The diurnal forcing and horizontal winds from a Global Climate Model (GCM) calculation, the observations reported here, and gravity wave and Rossby wave theory can be combined to test for the special conditions inherently required for each wave type to vertically propagate through Pluto's strong temperature inversion.

(3) Models like that used in Toigo *et al*. 2010 should be updated to post-NH input data and knowledge (e.g. thermal structure, ice composition distributions, and wind profiles) as they may shed light on certain observed haze layer structure(s).

(4) Exploration of the cause of the 25 km layer reported in this study should be done (Figure 59 and Figure 60), as its emergence and disappearance are co-located with tilted layers. This feature is also associated with global trends in layer slopes which may point to a planetary wave as the explanation for most of the observed layering (feature can be tracked ~ 1/4 Pluto's circumference) and coincident with the predicted location of Pluto's temperature maximum (Hinson *et al*. 2017).

(5) MVIC images should be analyzed, and haze layer/wave characteristics extracted, to compare against the characteristics outlined here for LORRI images. Also, limitations inherent to FFT/periodogram PSDs should be overcome by applying wavelet analysis to several images.

(6) Lastly, NH data is leading to a better understanding of the possible causes of haze layers in planetary atmospheres. This rich dataset should continue to be used with state-of-the-art models of Pluto's atmosphere.

CHAPTER FOUR

Simulations of Orographically Driven Gravity Waves to Explain Haze Layer Structure in Pluto's Atmosphere (Jacobs *et al.* 2019b)

Abstract

Pluto's atmosphere has an extensive haze with an embedded complex haze layer structure. The purpose of this paper is to consider the plausibility of internal gravity (buoyancy) waves forced directly by flow over topography (orographic gravity waves) in generating the observed haze layering. A single scattering model was implemented to simulate three LOng Range Reconnaissance Imager (LORRI) image sequences. Direct comparisons were conducted using haze layer characteristics outlined in a companion paper. A 2D gravity wave (GW) perturbation field generated from an orographically-driven GW model was used to produce north/south and east/west oriented 3D layered structures. The layer orientations and GW model were informed by Pluto Global Climate Model (GCM) wind speeds and direction. General agreement with LORRI-observed haze layer altitude range (20-140 km) and background relative amplitudes (around 0.025-0.045) were found in simulations for the 2.5-6 ms^{-1} wind cases and after the applications of LORRI's point spread function (PSF). Haze layer tilt orientation inferred from GCM

wind direction contradicted observed haze layer orientations in the Tail of Cthulhu region and matched tilt orientation in the Sputnik Planum (SP) region. For this reason, the SP region was focused upon as the best case for orographically driven gravity waves. Simulated layer slope magnitudes in the SP region were too large compared with observations for all wind speed cases, and projection/viewing geometry effects could not reconcile these differences for both wind orientations tested. Low altitude layer wavelength was in best agreement with observation for the 4.5 and 6 ms^{-1} cases. Both simulated and observed amplitudes grew with altitude, however observed amplitude growth was more pronounced below ~ 40 km. A near surface layer was found to be better represented using Community Aerosol and Radiation Model (CARMA) output where particle size distributions varied with altitude. An aggregate distribution provided best agreement with the observed I/F (although a sphere phase function value ~ 5 was used for HIRES).

4.1 Introduction

Waves in Pluto's atmosphere were first proposed as an explanation for resolved structures in the atmospheric temperature and density radial profiles derived from Earth-based stellar occultation measurements (McCarthy *et al.* 2008, Person *et al.* 2008, Hubbard *et al.* 2009). Tidal oscillations were later suggested by Toigo *et al.* (2010) as one possible forcing mechanism**.** After the New Horizons flyby in July 2015, a new forcing mechanism was put forth—oscillations induced directly by flow over topography (where the flow could possibly be linked to tidal oscillations). Multispectral Visible Imaging

Camera (MVIC) and LORRI images revealed > 20 layers embedded in a background haze. Layers were noted as having a vertical spacing of ~ 10 km, and to be most numerous at low latitudes. Haze layer positions appeared to be stationary with altitude on time scales of 2 to 5 hours. This set of observations motivated the development of an orographic gravity (buoyancy) wave model for stationary waves occurring over periodic topography.

Solar induced sublimation of Pluto's surface ices (N_2 , CH_4 , and CO) drive transport of volatiles from warmer to colder regions where surface deposition occurs. Due to small variations in pressure, surface winds are expected to be less than ~ 5 m s^{-1} (Forget *et al.* 2016, Bertrand *et al.* 2017). However, these winds near the surface can still generate gravity waves (Gladstone *et al.* 2016). Mountains were discovered by New Horizons imagery of Pluto with heights of 2-3 km, The SP basin exhibits an even larger, abrupt change in altitude (~ 4 km) and ridges exist NE of SP that are periodic in nature (Schenk *et al*. 2018).

For gravity wave oscillations to cause layering, they must reach saturation close to the surface. Solutions to the gravity wave equation that reach saturation amplitudes by 4 km require a surface vertical forcing velocity $w_z \geq 0.4$ cm s^{-1}. This threshold was achieved assuming standing waves generated by horizontal winds of u_0 = 5 cm s^{-1} flowing over ridges with height h_0 = 1.5km, zonal wavelength of λ_x ~ 120 km, and meridional wavelength of λ_y ~ 3600 km (or any product of $u_0 h_0$ = 7.5 with u_0 in cm s^{-1} and h_0 in km). Several other thresholds can be applied to the allowed wind speeds and scales of topography generating gravity waves if the atmospheric structure is well constrained as it

was in Hinson *et al*. (2017). The first of which can be expressed as a condition between the Scorer parameter (l) and the horizontal wavenumber (k) of the ridges for which waves could vertically propagate given wind speed (u_0) and Brunt-Vaisala frequency (N_B) profiles. The condition for vertical propagation is $k^2 < l^2$. Vertical lines in Figure 68 are for the corresponding horizontal spacing/wavelength of the ridges and gold lines correspond to the Scorer parameter for different wind speeds. Ridges that are spaced > 50 km apart can generate waves that vertically propagate throughout the entire atmosphere for all the wind cases, whereas horizontal scales of less than 10 km cannot vertically propagate higher than ~ 30 km for the whole range in wind speed.

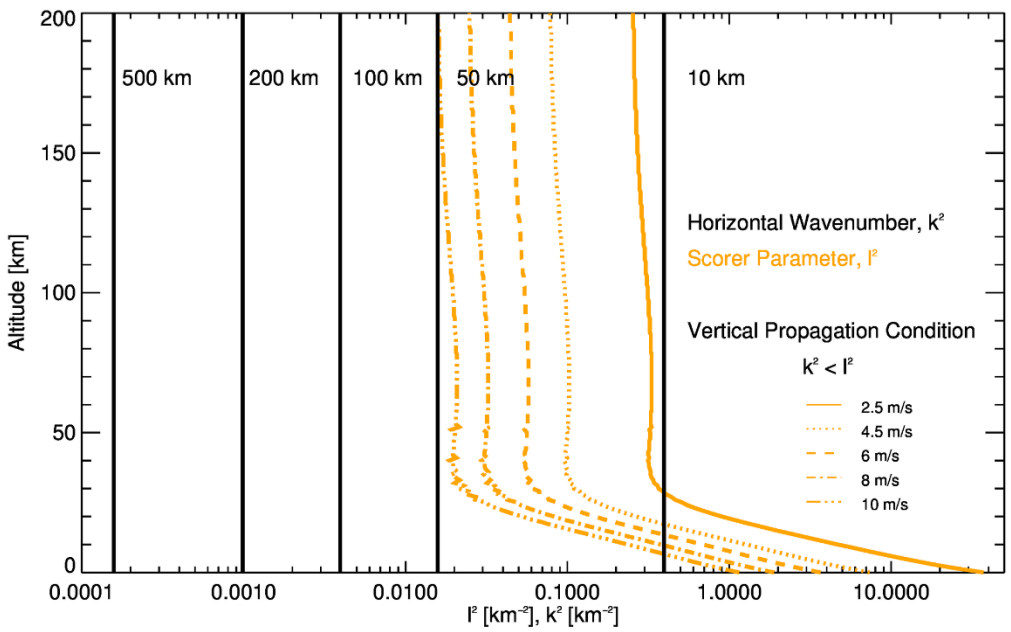

Figure 68: Comparison of Scorer parameter for several wind speed cases to several horizontal wavenumbers (wavelengths). Orographic gravity waves generated by ridges with horizontal scales less than 10 km will not propagate above ~ 30 km altitude for all wind cases. Topography with scales larger than 50 km can vertically propagate throughout the atmosphere for all wind cases.

The second condition relates the vertical scale of topography to the atmospheric structure (N_B) and wind speeds allowed for flow to be forced over, and not around, ridges. This condition can be stated as $h_0 > u_0 / N_B$. One interpretation of this condition follows from the assumption that the vertical scale of ridges is h_0 = 1.5 km above, and that $N_B \sim 3 \times 10^{-3}$ s^{-1} just above the surface. With these values flow would start to be diverted around the ridge as opposed to over it to generate gravity waves for wind speeds greater than 4.5 ms^{-1}.

Haze density changes induced by the gravity waves were found through the solution to the linearized atmospheric continuity equation by action of gravity waves on the background density profile (assumed to decay exponentially with haze brightness scale height of H = 50 km) where the ratio of haze particle number density perturbation to background density is proportional to the 2D divergence of wave induced haze density fluxes. The assumption here is that the haze particles can act as a tracer for wave motions. The sedimentation timescale for a typical haze particle (aggregate, 0.1 μm radius composed of 10 nm monomers) ranges from ~ 10^6 – 10^7 s to traverse the average haze layer spacing (~ 10 km) at 200-10 km altitude, respectively (Gao *et al*. 2016, Cheng *et al*. 2017). The buoyancy period in Pluto's atmosphere ranges from ~ $6 \times 10^2 - 6 \times 10^3$ s for the altitudes 200-10 km, and the wave period for the orographic gravity wave model in this study ranges from ~ $2 \times 10^3 - 1 \times 10^4$ s for the same altitude range. Consequently, the haze acts as a tracer, or relatively stationary, relative to predicted wave motions. A 2D solution aligned with the wind direction was found and a dataset representing perturbation haze particle densities $n'_H(x, z, t)$ relative to the mean densities $n_H(z)$ was generated (Figure 26, Cheng *et al.* 2017).

Several features in this solution are important to note for model results and interpretation presented here. First, the layer spacing (vertical wavelength), to first order, can be given by $\lambda_z \sim 2\pi u_0 / N_B \delta$, where $\delta = (1 + (l/k)^2)^{1/2} \approx 1$ is the aspect ratio. Because N_B is well constrained from occultation measurements, agreement in haze layer spacing can be used to constrain u_0, linking haze layer observations and Pluto's general atmospheric circulation and dynamics.

Secondly, observed and modeled haze layers are measurably tilted relative to the surface of Pluto. Gravity wave model layers exhibit an intrinsic tilt/slope associated with their vertical propagation. Layers correspond to constant phase lines in gravity wave oscillations (Holton 2004). The phase lines tilt upward in the opposite direction of the wind when stationary over the source terrain (e.g. a right to left wind results in positively sloped layers). The slope of the phase lines can be represented using the heuristic treatment of internal gravity waves for oscillations where rotation is insignificant ($N_B \gg f$). The relationship between layer slope and the dispersion relation given by the ratio of the vertical to horizontal group velocities as

Equation 85

$$s \equiv layer\ slope \equiv \left|\frac{c_{gz}}{c_{gx}}\right| = \left|\frac{k}{m}\right| = \frac{\lambda_z}{\lambda_x} = \left[\frac{{N_B}^2}{\omega^2} - 1\right]^{-\frac{1}{2}}.$$

Haze layer slope is then directly related to the ratio between the wave frequency, ω and N_B (when $\omega^2 \gg f^2$). Consequently, with measured slope values information on projection effects (due to wind direction and viewing geometry), and a well constrained N_B with altitude—gravity wave model and/or Global Climate Model (GCM) predictions can be qualitatively and quantitatively tested. Wind direction is used to adjust slope orientation and magnitude, and wind speed is adjusted in the gravity wave model to match observations in λ_z.

Observational characteristics of Pluto's haze layer structure outlined in Jacobs *et al*. 2019a were compared using three LORRI image sequences listed in Table 7. Important parameters for the three image sequences analyzed are summarized, and additional image sequence details can be found in Cheng *et al.* (2017) and/or Jacobs *et al.* (2019a).

Table 7: Summary of image sequences at high phase angle considered in this study of visible haze layer structure at multiple scales and resolutions.

Observation Sequence	**Start Time (UTC)**	**Time to Closest Approach (hrs.)**	**S/C Distance to Pluto (km)**	**Exposure Time (msec)**	**Resolution (km/pix)**	**Solar Phase Angle (deg)**
P_MULTI_DEP_LONG_1 (P_MULTI)	7/14/201 5 15:42	3.78	193,342	150	0.96	169
P_LORRI_FULLFRAME_DEP (FULLFRAME)	7/15/201 5 03:26	15.61	775,278	150	3.85	165
P_HIPHASE_HIRES (HIRES)	7/14/201 5 12:04	0.24	18,758	10	0.093	148

The geographic locations on Pluto above which observations were made and simulations were conducted for direct comparison are shown in Figure 69. Comparisons include slope magnitudes and orientations, profiles (with waveforms and PSDs), and analysis on a best-case region for topographically driven gravity waves (labeled Q1 in Figure 69). Additional comparisons are conducted for the HIRES image sequences where a surface

layer was found to be best reproduced by CARMA particle characteristics instead of dynamics/gravity waves.

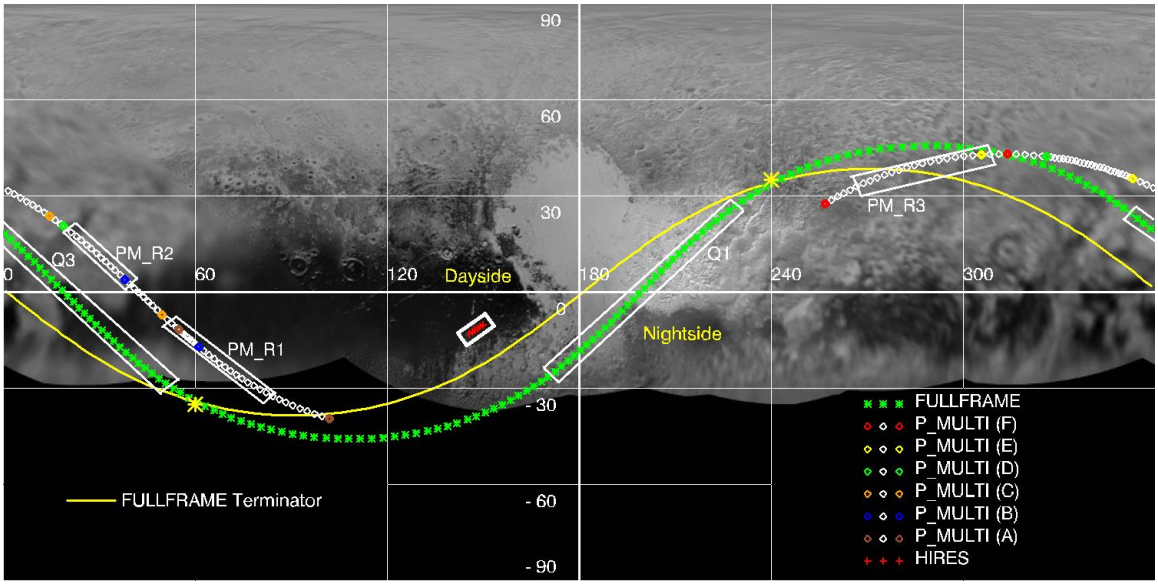

Figure 69: Limb traces for the three LORRI image sequences superimposed on an unwrapped cylindrical base map projection of Pluto's surface (Schenk et al. 2018). Note the relatively consistent latitude extent for the P_MULTI and FULLFRAME sequences, with an approximately 20˚ longitude shift in limb region sampled. Each color symbol for P_MULTI corresponds to a different image frame boundary in the sequence and have considerable overlaps. The terminator location during the FULLFRAME sequence is indicated dayside and nightside defined. FULLFRAME quadrant locations and P_MULTI region locations further analyzed in the following section are indicated.

4.2 Methods

4.2.1 Single Scattering Model Calculations and Viewing Geometry

All LORRI images analyzed in this study exhibit limb viewing geometry, with each pixel representing a line of sight (LOS). The model used to simulate LORRI images has been adapted from a single scattering image simulation code originally developed to

study the Earth's plasmasphere (Gladstone *et al.* 1992). The current code uses New Horizons ephemeris data taken from the Planetary Data System (PDS) repository library files for LORRI observations as well as the New Horizons Geometry Visualizer (NHGV) tool for Pluto right-hand-rule (RHR) atmosphere and geographic axis orientation.

The observed intensity (irradiance) for a single pixel is related to the available flux along the LOS by the radiative transfer equation. Haze I/F (observed light intensity times π and divided by the incident solar flux) was simulated to directly compare with LORRI images where data numbers (DN) were converted to I/F using the LORRI instrument (Science Operations Center) SOC pipeline. The vertical optical depth of Pluto's atmospheric haze at visible wavelengths is ~ 0.02, so that the haze can be considered optically thin and the single scattering approximation is valid (Gladstone *et al.* 2016). If absorption is considered small at LORRI's pivot wavelength (607.6 nm), and there is no direct transmission, the I/F can be given as,

Equation 86

$$I/F = \frac{1}{4} P(\Theta) \sigma_s \eta_{LOS}$$

where $P(\Theta)$ is the phase function at spacecraft-solar phase angle (Pluto-centric) Θ, σ_s the scattering cross section, and η_{LOS} the LOS column density for a given pixel (Petty 2008, Lavvas *et al*. 2009, Gladstone *et al.* 2016). The spacecraft-solar phase angle was used as the constant scattering phase angle for each image due to the far field approximation and LORRI's narrow angle FOV relative to spacecraft range. Another contribution to I/F

which is not considered here is the reflection of light off Pluto's surface that can then be scattered along the LOS. This additional source of irradiance becomes significant at mid-to-low phase angles. LORRI images in the HIRES sequence show considerable surface illumination on the side of the limb facing the spacecraft which may considerably affect the scattering parameters for this image sequence. Surface illumination contributions are likely negligible for the P_MULTI and FULLFRAME sequences.

A simple background haze was adopted for the gravity wave simulations—an exponentially decaying haze number density with constant scale height (~50km), and constant scattering cross section (or constant particle size and refractive index), phase function, and reference/surface number density (azimuthal symmetry in haze density). The set of parameters chosen for the P_MULTI and FULLFRAME image sequence simulations are summarized below in Table 8. The particle composition/refractive index was also fixed and taken from Khare *et al.* (1984). Haze particles were assumed to be homogenous spheres for the simulations with gravity wave perturbations. Although improvements in fitting the phase function and overall I/F vertical profiles are found with a combination of spherical particle properties as in Table 8 below 45 km tangent altitude and aggregate particles of different size above 45 km (Cheng *et al.* 2017), general agreement with observations was found with this set of parameters. A quantitative comparison of background I/F fitting was not the focus of this study.

Table 8: Background haze parameters used by the scattering code to simulate limb I/F with gravity wave perturbations. The set uses the refractive index and homogenous sphere properties from Khare et al. 1984 at LORRI's pivot wavelength. The HIRES simulations received best background haze results with a phase function shifted to 5, likely related to the considerable decrease in phase angle.

	Radius [μm]	**Scattering Cross Section [cm^2]**	**Phase Function [UNITLESS]**	**Surface Number Density [cm^{-3}]**	**Max I/F Simulated [UNITLESS]**
Parameters	0.30	0.8×10^{-8}	20	0.1	~ 0.25

Altitude varying particle characteristics were explored, however their vertical scale of variation inferred from microphysical processes and output from CARMA were large compared to the vertical scales of perturbations and did not considerably affect the simulated layers. The numerical form of Equation 87, with number of points along the LOS, n_{LOS} set by a chosen LOS resolution δs and 0-400km altitude domain of the model is given by,

Equation 87

$$I/F = \frac{1}{4} P(\Theta) \sigma_s \sum_{k=0}^{n_{LOS-1}} N_k(z) \delta s \,,$$

involving only integration of number density along the LOS (where the number density of a given LOS point at altitude z is $N_k(z)$) and interpolation of particle properties. The appearance of layers did not change for LOS resolutions at or below 1 km.

Scattering parameters for spheres were calculated with the combination of code from FORTRAN Mie scattering routines for spheres and the bmie.pro IDL routine (Bohren, C. and D. R. Huffman 1998). An approximation made in this study was that LORRI's response is solely at its pivot wavelength (monochromatic light source). Calculations of scattering across LORRI's entire bandpass have not been calculated and are assumed here to have small effects on the results of background relative brightness variations. This assumption cannot be made in constraining particle properties, but the focus of this study was to analyze the variation in brightness due to perturbations in haze particle number density, for which this assumption is taken to be a good approximation.

A near surface layer was predicted by CARMA, with a rapid change in particle size and number density relative to variations above. Particle distributions were explored to produce this layer in the scattering model. Pluto's haze appears blue, indicative of Rayleigh scatterers with radii < 0.010 μm. However, the haze was also observed to have a large high-to-low phase angle brightness ratio—indicating strong forward scattering by larger particles (> 0.1μm). The Multi-spectral Visible Imaging Camera (MVIC) blue/red channel ratio also increases with altitude, consistent with smaller particles at higher altitudes transitioning to larger particles at lower altitudes (Gladstone *et al.* 2016). Observations indicate that Pluto's photochemical haze is likely an analog of Titan's detached haze layer—consisting of monomer particles which undergo sticking collisions

to form larger fractal aggregate structures that sediment out as complex organic compounds called tholins (Cabane *et al.* 1993, Lavvas *et al.* 2009, Lavvas *et al.* 2010, Lavvas *et al.* 2011). For each CARMA fractal aggregate case, scattering cross sections were adopted using data generated in Tomasko *et al.* (2008). For background haze datasets that needed to be interpolated and do not have number densities derived directly as a function of altitude, a natural log interpolation scheme was used to obtain the background haze density $N_k(z)$.

4.2.2 Predicted Winds from the Pluto Global Climate Model (GCM)

We use the Pluto LMD Global Climate Model (GCM, Forget *et al.* 2017; Bertrand & Forget 2017) to estimate the wind direction and speed in Pluto's atmosphere in 2015 and their potential impact on the orientation of the haze layers. The GCM predicts a North-South weak meridional circulation triggered by North-South nitrogen condensation-sublimation flows and thermal winds. This triggers strong retrograde westward winds in the upper atmosphere of Pluto above 5 km altitude (Bertrand *et al.* 2019, Figure 70). A westward zonal wind direction dominates by 10 km above the surface. Consequently, a westward zonal wind was adopted in considering haze layer tilt orientation for observations over the Tail of Cthulhu region (P_MULTI mosaic frames A-C, FULLFRAME Q3, in Figure 69).

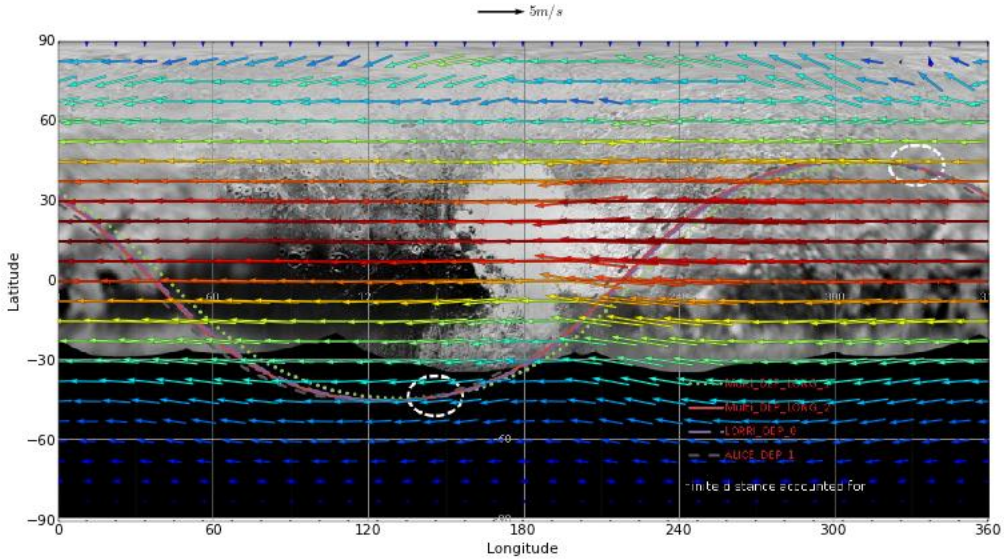

Figure 70: Horizontal winds obtained with the LMD Pluto GCM for 2015 at 10 km above the surface. Vector length for a 5 m s-1 wind is shown at top. A westward zonal wind is the dominant component and persists during one Pluto day for low latitude and equatorial regions where most numerous layering was imaged by LORRI. This robust retrograde wind is used to infer haze layer tilt orientation.

Additionally, southward meridional and westward zonal wind cases were explored for the SP region observations (FULLFRAME Q1, Figure 69). Vertical profiles of the retrograde winds are shown in Figure 71. The rapid increase in wind speed from ~ 1 ms^{-1} close to the surface to ~ 9 ms^{-1} by 20 km was used to inform cases in the orographic gravity wave model in generating haze layer structures simulated in the P_MULTI and FULLFRAME image sequences.

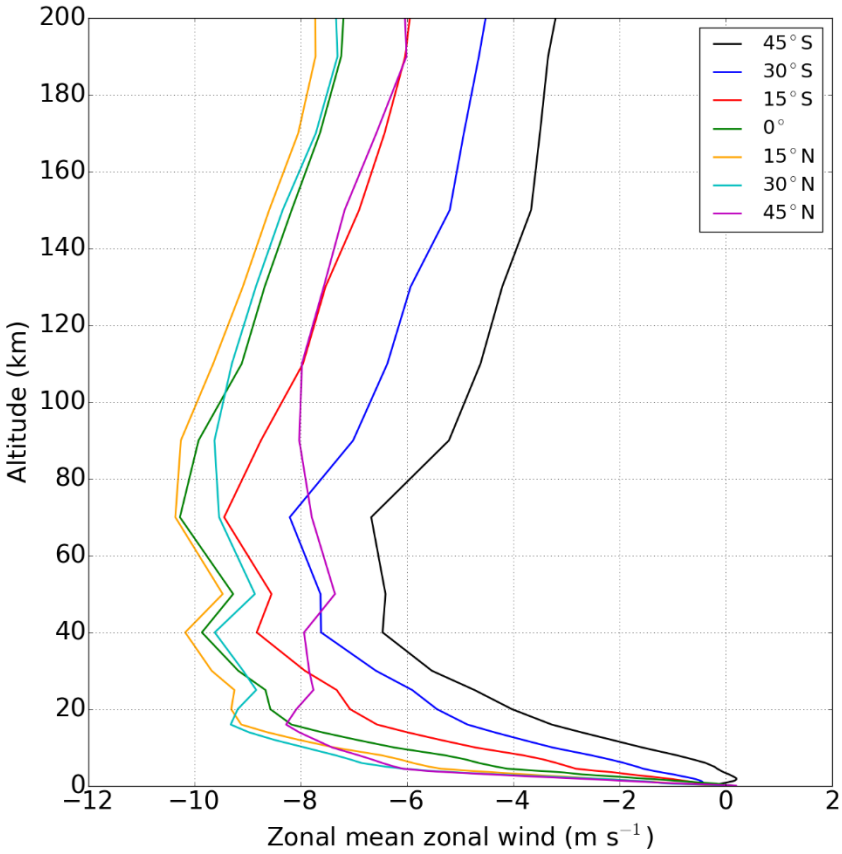

Figure 71: Vertical profiles of zonal mean zonal wind obtained with the GCM for 2015. Winds increase rapidly to as much as 10 ms-1 in the equatorial to midlatitude regions where limb sampling occurred (see Figure 70), and haze layer structure was observed. Important in dictating vertical wave propagation and dynamics, the wind speeds were also used to inform the orographic gravity wave model for layers occurring over SP.

4.2.3 Application of Gravity Wave Density Perturbations

The 2D gravity wave perturbation data in Figure 26 of Cheng *et al.* (2017) are the only currently existing model results of orographic or any other gravity wave type perturbations to haze particle number densities for Pluto. Several wind cases were considered spanning the range of winds speeds in Figure 71. Several gravity wave

variables, including the wind profiles and corresponding vertical wavelengths of induced haze layers, are shown in Figure 72. The temperature profile was adopted from Hinson *et al.* (2017) and Young *et al.* (2018). General trends include the rapid increase in haze layer vertical wavelength with increasing temperature (corresponding rapid decrease in Brunt-Vaisala frequency) and a less rapid increase in wind speed from the surface up to Pluto's temperature maximum.

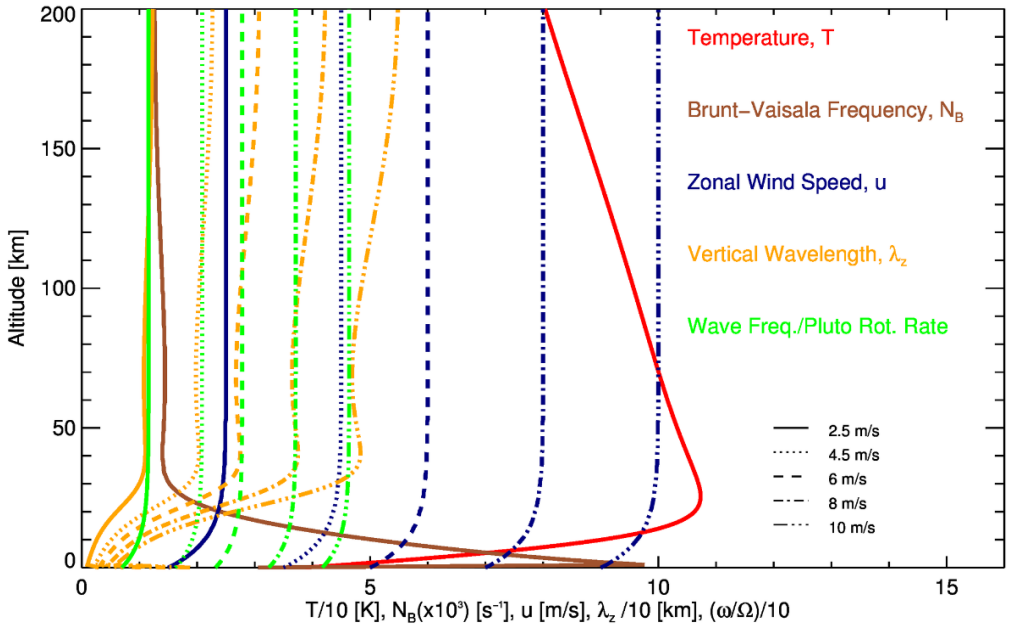

Figure 72: Vertical profiles for key atmospheric variables used to calculate orographic gravity wave propagation and haze layer formation. Colors correspond to each variable and line-styles to each wind case considered in the model. Vertical wavelength of the layers increases with wind speed, with much more rapid increase in wavelength below Pluto's temperature maximum. The rapid increase in N_B dominates trends in λ_z and ω.

A 3D model capable of producing global perturbed haze particle number densities on the vertical scale of the observed haze layers (vertical scales down to ~2-10 km) from the

surface to around 200 km did not yet exist for this study. To simulate 3D LOS perturbed haze scattering, the 2D dataset was repeated along lines of longitude and latitude to allow two perpendicular orientations of the haze layer structure to be analyzed. Figure 73 illustrates the two orientations that result from repeating the datasets along lines of longitude and latitude. Arrows show directions that the tilted layers are repeated, with the left diagram corresponding to gravity wave perturbations initiated by a zonal wind, and the right diagram to a meridional wind.

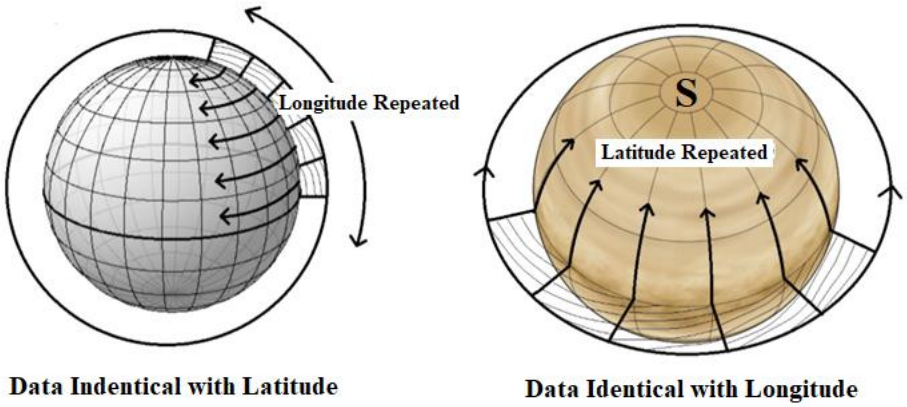

Figure 73: Diagrams depicting how two orientations for the 2D gravity wave perturbation data sets are repeated to make an effective 3D dataset for the scattering code interpolations. (Left) Meridional wind representation, data repeated along longitude lines, data identical with latitude. (Right) Zonal wind representation, data repeated along lines of latitude, data identical with longitude (south pole indicated).

The 2D datasets are haze particle number density perturbations relative to background values and range from -1 to 1. The background relative perturbation is defined as $\eta = n'_H(x,z,t)/n_0(z)$ in Cheng *et al.* (2017), and the total or perturbed number density,

$N_T(z)$, is represented by $N_T(z) = n_0(z)[\eta + 1]$. The haze layer slope orientation set on the perturbation datasets relative to the prevailing wind direction is labeled for two orientations in Figure 74.

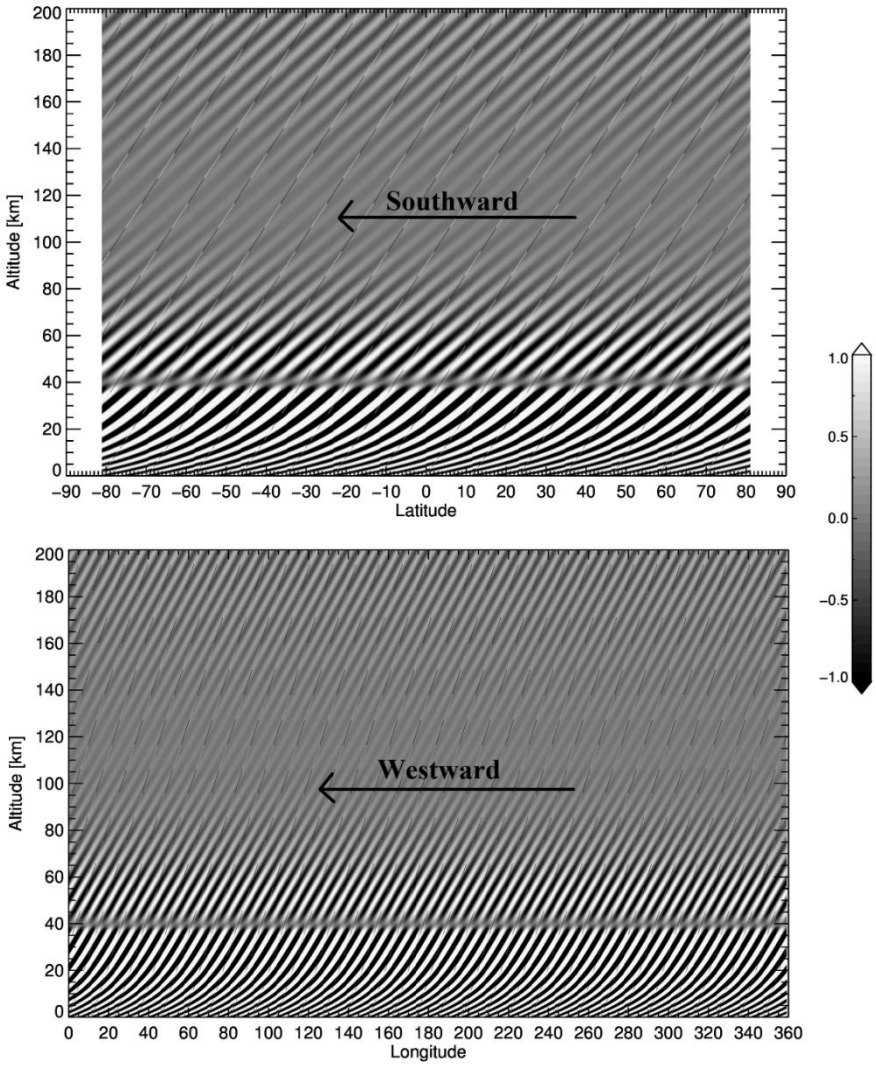

Figure 74: Haze layer tilt orientations relative to wind direction constructed for the southward meridional **(top)** wind case and the westward zonal **(bottom)** wind cases. The bottom case layer slopes appear larger due to the larger horizonal distance (Pluto's circumference at top) being compressed into the plotting space. Both perturbation datasets were constructed from gravity wave model output where the wind speed approached a constant value of 4.5 m s^{-1} by an altitude of 20 km.

The generated layers have an intrinsic tilt associated with their parent mountain ridge spacing dimensions (λ_x) and prevailing wind speed (u_0), and Pluto's temperature structure (N_B). For example, in the P_MULTI sequence, a mosaic was simulated and constructed to compare to the mosaic of observed LORRI images. Preferred zonal mountain ridge spacing of 120 km and a range of winds speed of 2.5 - 10 ms^{-1} generated an intrinsic haze layer slope range of $\lambda_z / \lambda_x \sim 0.06 – 0.08$ km/km below Pluto's temperature maximum (~ 25 km altitude) and ~ 0.03 – 0.1 km/km above. The values for each wind speed case are listed in Table 9.

Table 9: Intrinsic slopes associated with all tested wind speed cases.

Wind Speed [m/s]	2.5	4.5	6	8	10
Data Intrinsic Slope [km/km]	0.046	0.048	0.079	0.083	0.1

This intrinsic layer slope will be altered due to LOS viewing geometry and could create a significantly different magnitude of tilt observed by LORRI around Pluto's limb. The wind magnitude and wind aligned wavenumber can then be constrained from comparisons of observed ranges in layer slope to modeled layer structure slopes for this forcing mechanism. The four wind alignment cases considered in this study are represented in Figure 75 as part of a simulated image for the FULLFRAME sequence. Pluto's axis orientation does not change significantly between the three image sequences considered here, which is the second important factor (other than inferred wind direction)

in determining projection effects on haze layer tilt and appearance. Consequences of projection effects around the limb for these cases will be discussed later.

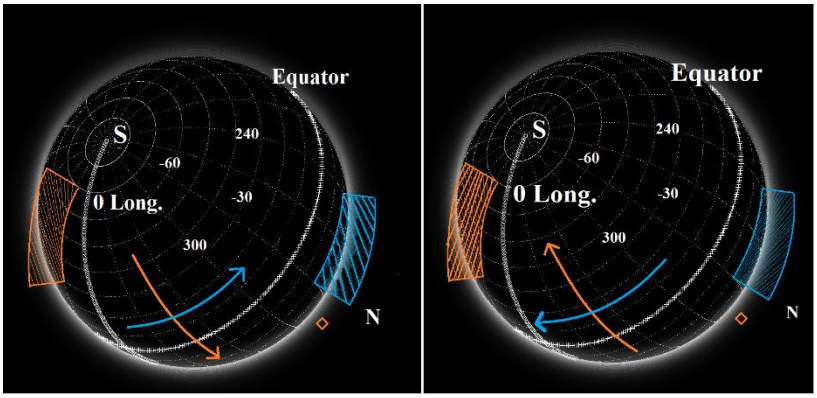

Figure 75: Illustration of all four wind cases imposed on Pluto's axis orientation for visualizing layer projection effects due to a combination of viewing geometry and wind direction. **(Left**) Blue – westward zonal wind orientation; Orange – northward meridional. **(Right)** Blue – eastward zonal orientation; Orange – southward meridional. Both simulated FULLFRAME image spin axis orientations relative to frame are consistent with P_MULTI for all intents and purposes as Pluto's geography only appears to shift/rotate by ~ 20˚ longitude between the two image sequences.

4.3 Model Results

4.3.1 P_MULTI Haze Layer Comparisons with LORRI PSF

Simulated haze layers without the application of LORRI's point spread function (PSF) appeared much sharper than in LORRI images. In addition to physical causes, consideration of instrument performance in resolving the layers was needed (e.g. diffraction effects; Cheng *et al.* 2008). Simulated images were convolved with LORRI's PSF to obtain more accurate representation of layer clarity and amplitude. A comparison

between the simulated, convolved image for frame C (right) and the corresponding LORRI image (left) are shown in Figure 76. The appearance of several thin layers observed by LORRI are comparable in brightness and thickness to the simulated image. However, thicker layers are superimposed with thinner layering in the observed LORRI image. This indicates multiple vertical scales (or wavelengths) present in Pluto's atmosphere, with the larger vertical scale structure not reproduced in this orographic gravity wave simulation. Larger limb-relative tilt is also apparent in simulated layers relative to LORRI layers for this image frame.

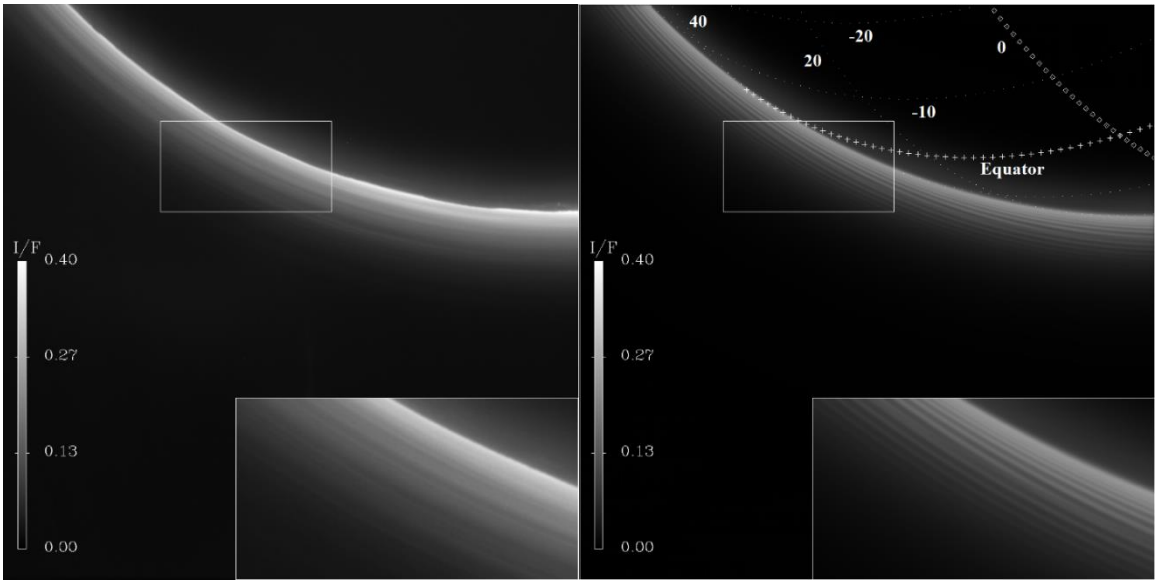

Figure 76: (Left) LORRI image (frame C, Figure 69) with a zoom inset from top left of image, below. **(Right)** Corresponding simulated image after application of LORRI's PSF for the southward meridional wind orientation with zoom inset. Several simulated layers have consistent width and brightness to finer scale layers visible within a larger scale variation in brightness of the LORRI image.

A 2x zoom inset is also shown. The linear scale is consistent between the LORRI and simulated image. A surface layer causes the LORRI brightness maximum (I/F ~ 0.44) to be much larger than simulated (I/F ~ 0.25) with an assumed background exponential decay number density profile. The presence of a surface layer is critical for reproducing the range in I/F observed across image sequence P_MULTI but played a less critical role in the FULLFRAME sequence I/F range agreement. This surface layer cannot be resolved above the limb for P_MULTI but is fully resolved in the HIRES sequence.

Radial profiles are shown in Figure 77 (3 LORRI - blue, 2 simulation – black and red) for frame C. The profiles were taken from the images shown in Figure 76, with the simulation (red) profile extracted from the unconvolved simulated image. Layering in simulations below 20 km altitude was smoothed out after application of LORRI's PSF. In the LORRI profiles, smaller scale layers can be difficult to differentiate from a larger scale oscillation. Simulated image profiles were extracted from the southward meridional, 4.5 ms^{-1} gravity wave wind case.

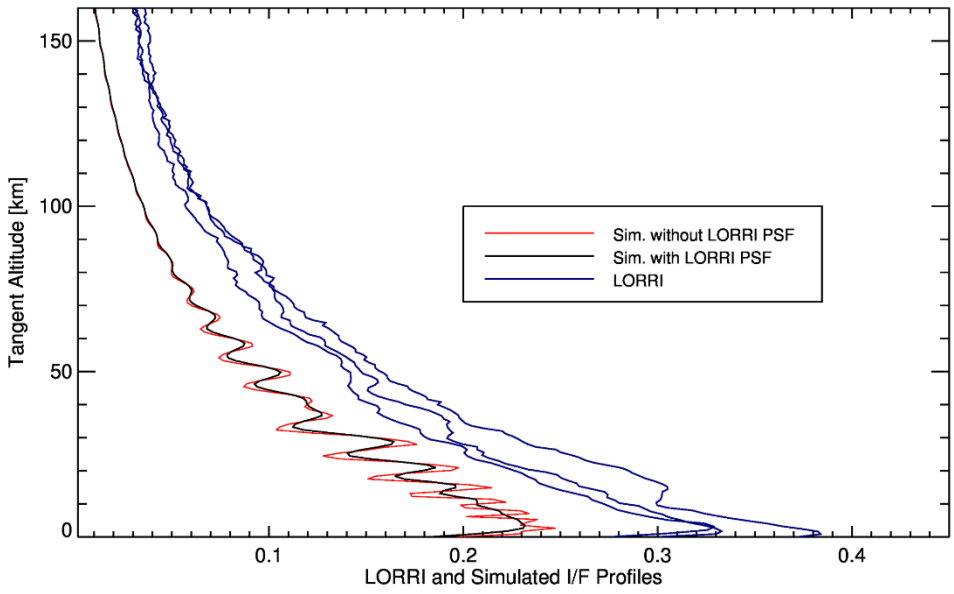

Figure 77: Radial profiles taken from simulation (black and red) and three LORRI image profiles (blue) for frame C. Simulated layer altitude range and thickness are comparable to LORRI's larger scale layers. Largest disagreement appears to originate from simulated layers exhibiting a larger brightness minimum component for each oscillation/layer as compared with LORRI profile oscillations.

The altitude range and thickness of simulated layers is in general agreement with the LORRI profile larger scale layers, however simulated layer amplitudes are considerably larger and do not exhibit an imbedded smaller scale oscillation.

Background trend (decaying exponential) normalized waveforms are shown in Figure 78, top. Haze layer amplitudes increase with wind speed, with the 2.5 ms^{-1} (black) case representing minimum amplitudes, 6 ms^{-1} (red) mid-range amplitudes, and 10 ms^{-1} (orange) the maximum amplitudes considered in this study (amplitudes ranging from 0.015-0.17, for all wind cases). Simulated amplitudes are in general agreement with observed small and larger scale oscillation amplitudes observed in LORRI waveforms for the 4.5 ms^{-1} and 6 ms^{-1} cases, respectively. Observed amplitudes varied between 0.01-0.05 for the P_MULTI image sequence.

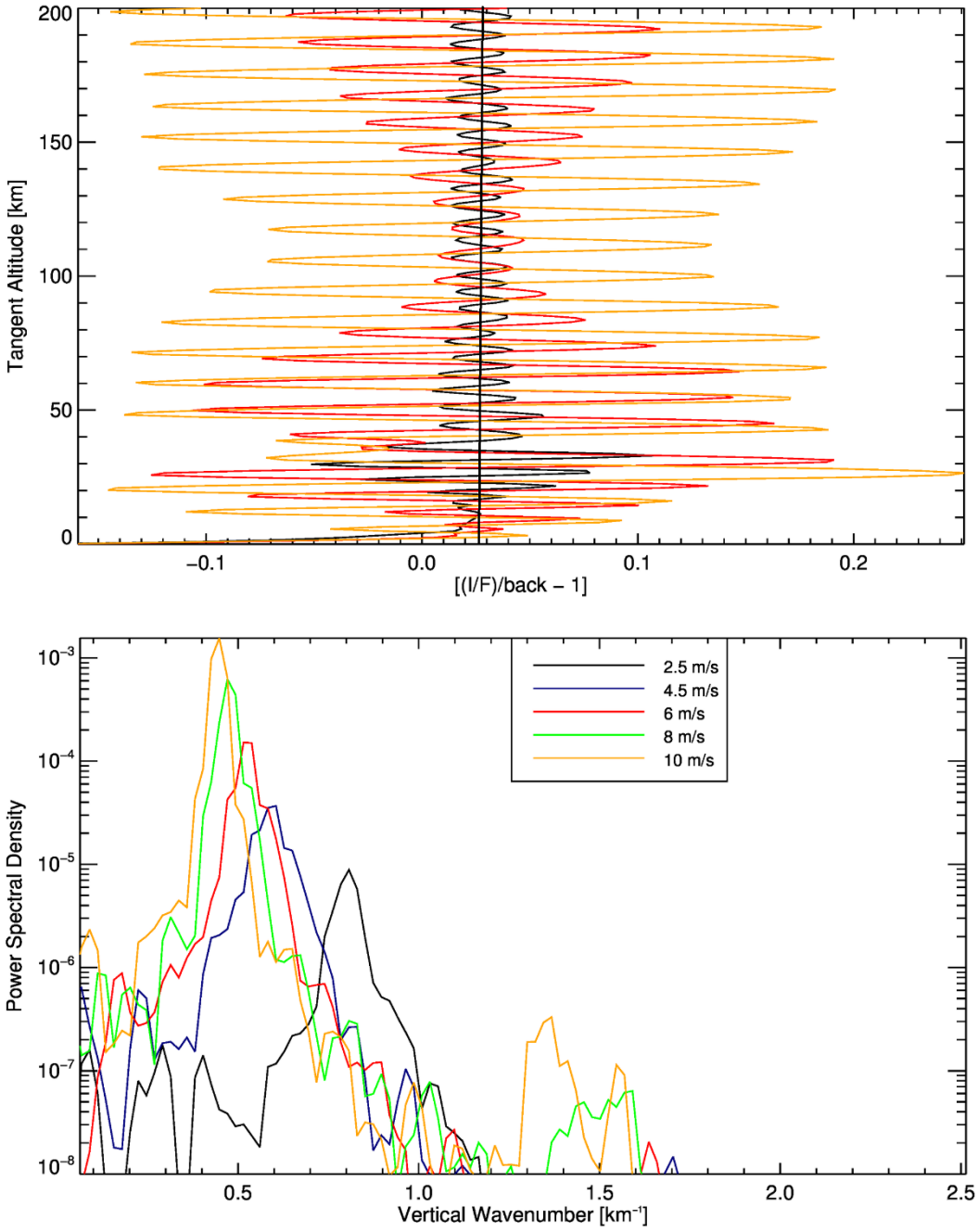

Figure 78: (Top) Simulated frame C waveforms, and **(Bottom)** PSDs with the application of the Hann Window, showing the progression toward lower wavenumber (larger vertical wavelength) and higher power with increasing wind speed. The increase in vertical wavelength with wind speed is less pronounced than predicted due to partial blocking of flow for wind speeds near the surface of ≥ 4.5 ms^{-1} (ratio of λ_z for 4.5 to 2.5 ms^{-1} is ~ 1.3, whereas the predicted factor is ~ 1.8).

This range was mainly set by the larger scale oscillation, since the smaller scale amplitudes were more difficult to quantify in observations (Jacobs *et al.* 2019a).

Corresponding PSDs with application of the Hann window are shown in Figure 78 (bottom) for all 5 wind cases to show the progression in PSD power and wavenumber/wavelength. Simulated peak powers are in best agreement with observed peak powers (10^{-5}-10^{-4}) for the 2.5, 4.5, and 6 ms^{-1} wind speed cases. These wind cases have associated peak vertical wavelengths of ~ 8, 10.5, and 12 km. The vertical wavelengths for the 8 and 10 ms^{-1} cases are around 13 and 14 km, respectively. All the PSD extracted vertical wavelengths are surprisingly smaller than predicted by the λ_z expression and plotted in Figure 72, except for the 2.5 ms^{-1} wind speed case. The cause of this decrease in vertical wavelength by a factor of 2-3 than expected is partial blocking (flow forced around, not over ridges) for near surface winds $\geq$ 4.5 ms^{-1} due to the condition $h_0 > u_0 / N_B$ previously discussed. Waveform vertical separations of maxima and minima are generally consistent with PSD values.

The variation of Pluto's haze layer structure across the entire dayside hemisphere, as well as agreement between haze layer tilt observations and all four wind orientations, were analyzed by constructing unwrapped mosaics of images in the P_MULTI sequence (as was done in Cheng *et al.* (2017) and Jacobs *et al*. (2019a)). Best agreement in slope orientation and magnitude out of all four wind orientations was first determined. Next, the case which had best agreement with GCM inferred winds was selected and compared. Neither simulated mosaic is edge filtered as the layers are considerably more distinct and

regular than observations (without LORRI's PSF) and can be more easily tracked without processing.

A panel comparison between the two best case sets of simulations and the LORRI mosaic for which slopes were extracted is shown in Figure 79. The southward meridional orientation mosaic (middle) contains positively sloped layers that level off moving left to right, transitioning to a slight negative slope close to the clock angle of 0°. Although the slope magnitude of the layers across most clock angles in this orientation is large compared to the LORRI mosaic (top), predominantly positive slopes and the leveling off trend are consistent with observations. This acts as the best case for agreement with observations. Figure 75 illustrates how and where layer slopes can appear to level off (decrease in slope from their intrinsic values). Using the orange dataset, starting at around 0° longitude and rotating around the south pole toward decreasing longitudes causes the layers to start picking up a larger edge on component until completely leveling off once at the longitude that meets the orange diamond limb location. This region at the orange diamond corresponds to layer 7 in Figure 79, middle (and to frames E and F in Figure 69).

If the eastward or westward zonal wind directions are chosen (for any of the 3-image sequence viewing geometries considered in this study), it is not possible for the layer orientations to exhibit a leveling off trend in their tilt when they are tracked around the limb in a similar manner. The westward zonal wind direction case (bottom) was chosen as the best case predicted by GCM winds in this region (see Figure 70).

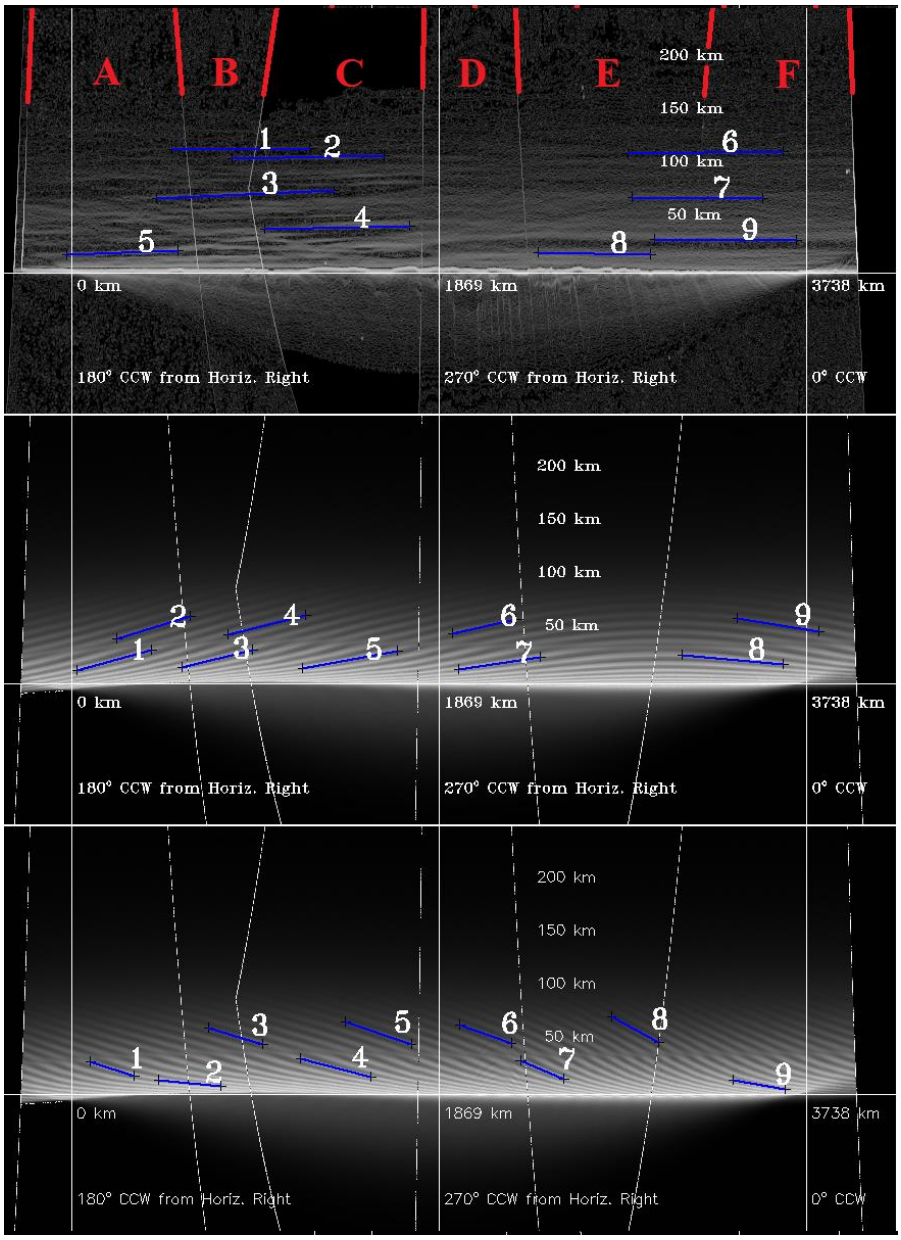

Figure 79: (Top) LORRI mosaic with haze layer slope extraction positions, **(Middle)** southward meridional wind orientation mosaic with layer positions, and **(Bottom)** the westward zonal wind orientation mosaic with layer positions. Both simulated mosaics are for the 4.5 ms^{-1} case. Slope values of the layers are shown in Table 10. The southward case acts as the best case when compared with observations, and the westward case as the best case as inferred from GCM predicted winds.

This orientation generates negatively sloped layers for the entire dayside limb, in contradiction with the predominantly positively sloped layers observed in the left half of the observed LORRI mosaic where layers are most numerous and distinct.

Extracted slope values for numbered layers in Figure 79 are listed in Table 10. Slopes were averaged for clock angles of 180-270° where observed haze layers were most numerous and had the largest tilt (Figure 79, top). Both the southward meridional and westward zonal orientation slopes are on average almost 10x larger than observed in this region, and the westward wind orientation slope sign/orientation inferred from GCM winds contradicts the predominantly positive slopes observed.

Table 10: Layer slopes [km/km] 1-9 labeled in Figure 79 for LORRI and both simulation orientations. Averages are shown for the left half of this mosaic where layers are most numerous and appear to exhibit the largest amount of tilt in the LORRI mosaic.

Layer Number	LORRI Mosaic	Southward Meridional Mosaic	Westward Zonal Mosaic
1	0.007	0.274	-0.326
2	0.021	0.306	-0.098
3	0.046	0.246	-0.302
4	0.021	0.250	-0.261
5	0.037	0.183	-0.338
6	0.013	0.226	-0.353
7	-0.008	0.150	-0.429
8	-0.018	-0.091	-0.543
9	-0.007	-0.163	-0.176
Average (180-270° CCW)	**0.026 (5)**	**0.252 (5)**	**-0.265 (5)**

The dataset intrinsic tilt range for the wind speed range of 2.5-10 ms^{-1} was measured to be 0.046-0.1 km/km, with the intrinsic slope of the 4.5 ms case shown in Figure 75 (middle and bottom) ~ 0.048 km/km. This shows that viewing geometry/projection effects in this region caused slopes to increase by as much as a factor of 4. The considerable increase in simulated layer slopes from their intrinsic values in this region rules out projection effects/viewing geometry as a way to reconcile simulated slope values with smaller observed slopes.

Based on these results and predicted GCM winds, additional adjustments to the gravity wave model winds were not pursued to explain layering in this region. However, initial agreement was found between observed slope orientation in the FULLFRAME Q1 region (see Figure 69) and slope orientation when considering the orographic gravity wave model for westward zonal winds predicted by the GCM. This information, combined with the topographic features resembling semi-periodic ridges with scales around that adopted in this model (λ_x = 120 km, h_0 = 1.5 km), motivated the focus of several cases to this region in the next section.

4.3.2 Global/FULLFRAME Haze Structure Comparisons

General agreement with Pluto haze brightness was found around the entire limb in the model (including Pluto shadow effects, sun direction toward image bottom) for the chosen haze parameters except for the asymmetry in haze brightness toward Pluto N discussed in Cheng *et al.* (2017). The gravity wave perturbations were applied to the

FULLFRAME image sequence background haze, with a focus on the Q1 region due to initial agreement in slope orientation for the GCM predicted wind direction. Due to SP's strong influence on wind direction and general circulation a southward wind direction was also considered for comparison. Figure 80 shows the appearance and slope extraction locations from all wind speed cases for the southward wind direction case, with LORRI Q1 region at top.

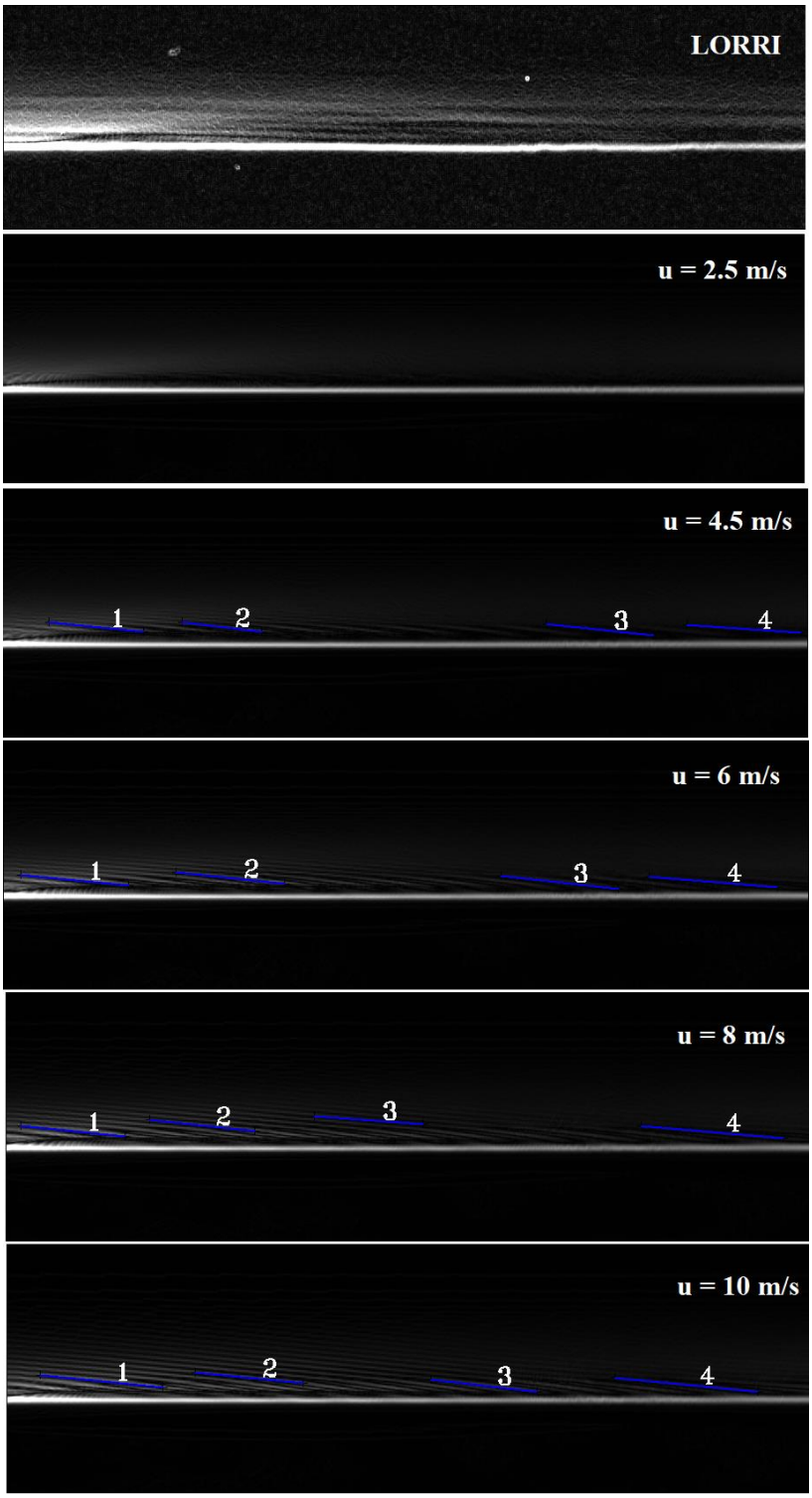

Figure 80: LORRI Q1/SP region layers at top where layer slopes were extracted, with all wind speed cases considered below including numbered locations where slopes were extracted for the simulations. The regions underwent the same processing as the top LORRI region (4-image stack, unwrapping, and Sobel edge filter).

The average values of extracted slopes are shown in Table 11. Layers become resolved for 4.5 ms^{-1} and higher wind speeds once amplitudes become large enough and vertical wavelengths are greater than 10 km. As in the P_MULTI sequence, the layer slopes are noticeably larger below ~ 50 km due to the sharp change in N_B for that altitude region dictated by Equation 85. Layers can be tracked almost down the limb for the higher wind speed cases.

Table 11: Average slope values for each wind speed case and the southward wind direction. The LORRI Q1 and Q3 average slope values are also listed for comparison. As in the P_MULTI comparisons, simulated slopes are considerably larger than observed.

LORRI Q1 Slope Average	Meridional (Southward) Q1 Average Slope	Wind Speed [m/s]
-0.025	N/A	2.5
LORRI Q3 Slope Average	-0.100	4.5
0.029	-0.099	6
	-0.092	8
	-0.103	10

A corresponding panel plot for the westward wind direction is shown in Figure 81. Again, layers are only visible/resolved for the higher wind speed cases, but for this orientation a clear interference pattern develops for lower altitudes where layers cannot be resolved. This also occurs for the region where a sharp change in slope occurs in tandem with the sharp change in N_B.

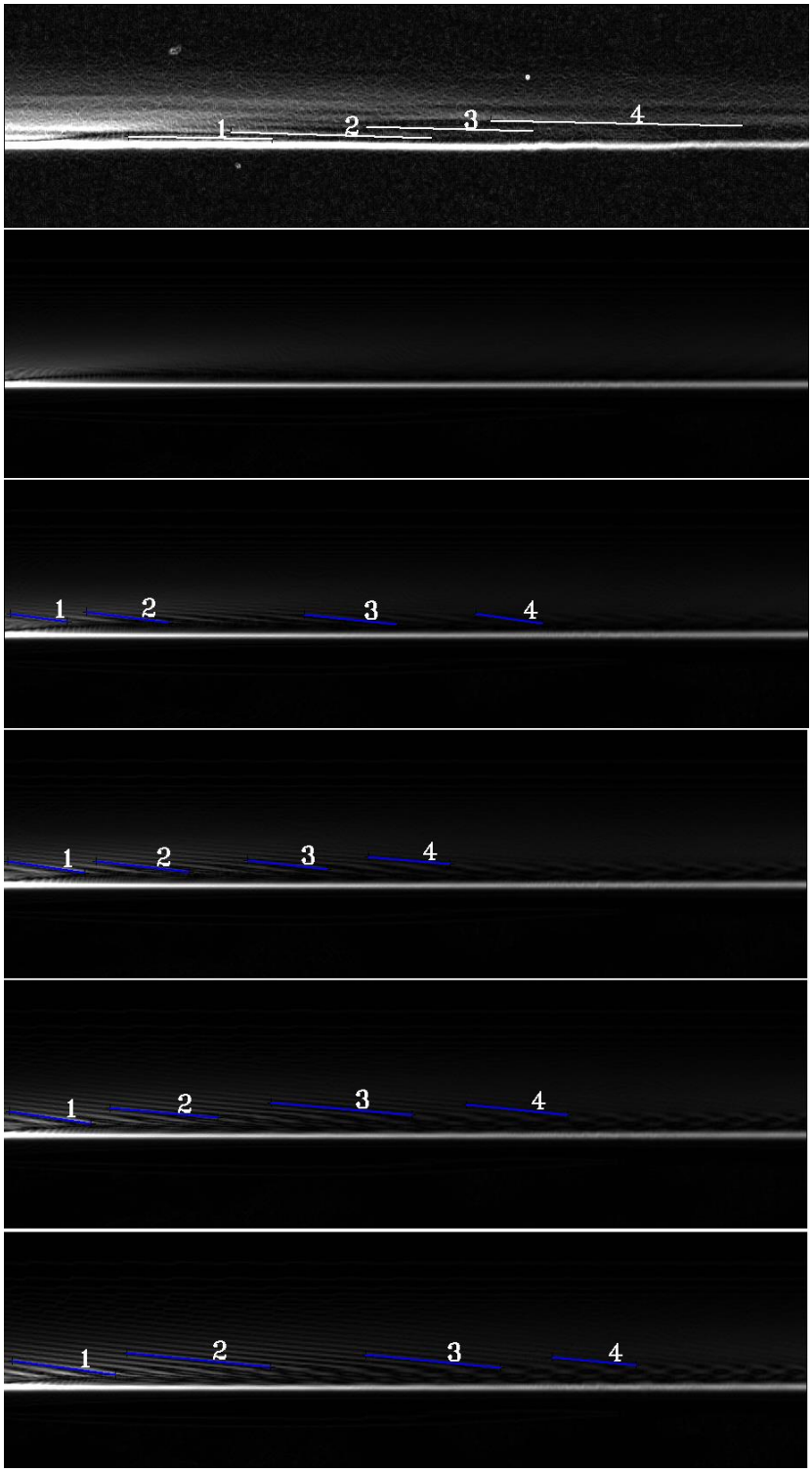

Figure 81: Slopes for each wind speed case of the westward zonal wind direction. Slopes are comparable to the southward wind direction, however viewing geometry effects for lower altitudes where the intrinsic slope of layers changes due to N_B cause the development of an interference pattern and layers not to be resolved.

Average slope values for the westward wind direction cases are shown in Table 12. Slope magnitudes are very comparable to the southward wind direction, so that slope magnitude cannot be used to differentiate inferred wind direction. A closer comparison of layers from the two-wind orientation is shown in Figure 82. The difference in resolution between the two orientations for lower altitude layers may imply that LORRI's observed layers are oriented as increasing more moving Northward as opposed to Eastward, regardless of the generation/driving mechanism. However, caution should be used in this interpretation, as LORRI's layers exhibit a larger vertical wavelength so that they are less susceptible to the development of an interference pattern.

Table 12: Average slope values for each wind speed case and the westward wind direction.

LORRI Q1 Slope Average	Zonal (Westward) Q1 Average Slope	Wind Speed [m/s]
-0.024	N/A	2.5
LORRI Q3 Slope Average	-0.129	4.5
0.029	-0.114	6
	-0.108	8
	-0.106	10

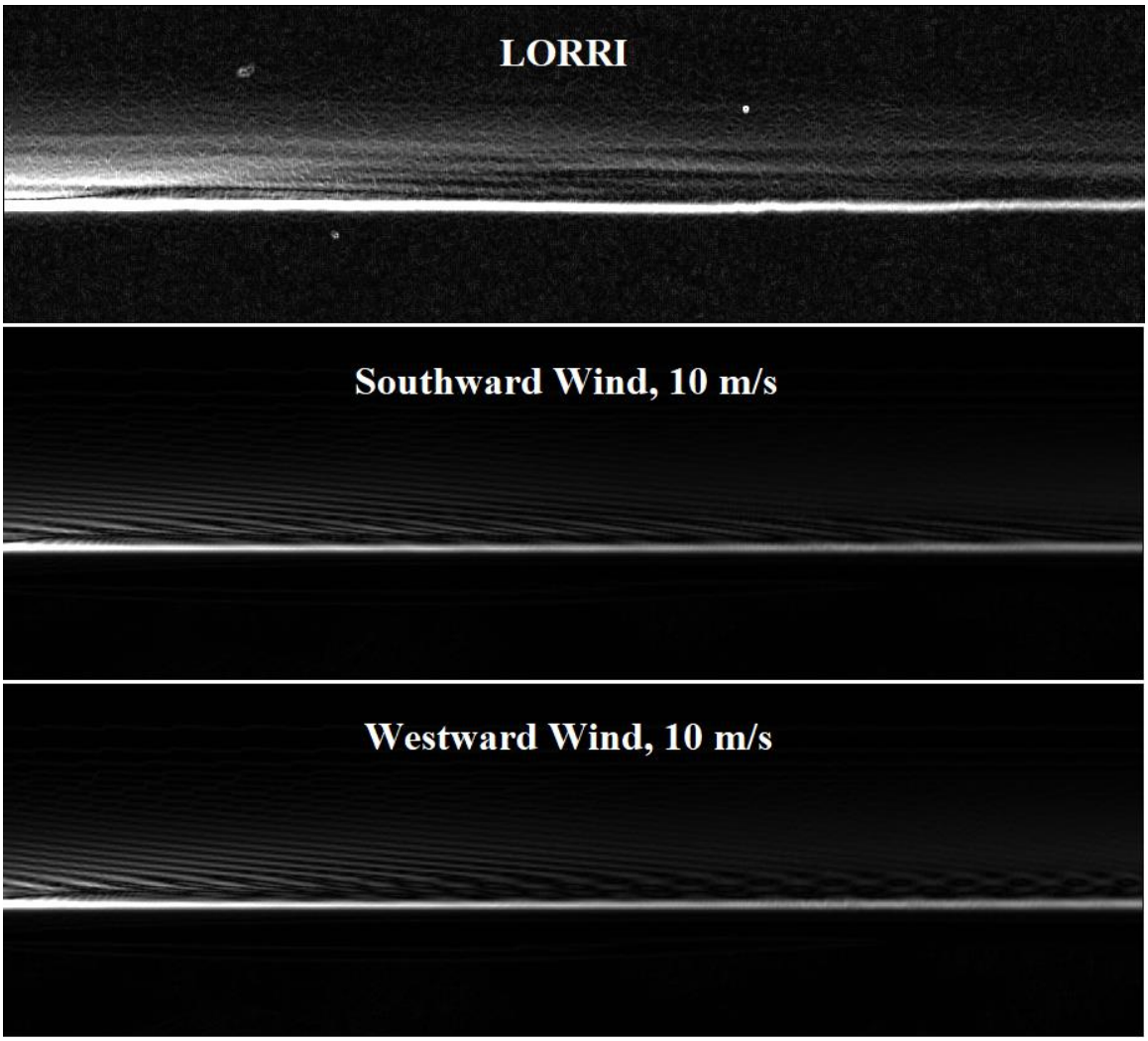

Figure 82: A comparison between the two wind orientations for the SP/Q1 region. Slopes are comparable; however, an interference pattern develops for the westward wind direction for lower altitudes while layers are traceable down almost to the limb for the southward wind direction. Although the vertical wavelength is considerably larger for LORRI layers, the fact that LORRI layers are also traceable almost down to the limb may imply that regardless of generation mechanism they are oriented so that their altitude increases considerably more moving Northward than Eastward.

4.3.3 Low Altitude Haze Layer Comparisons

Altitude dependent CARMA derived particle number density distributions were used to simulate the observed near surface layer and low altitude background haze. A rapid increase in particle number density and effective particle radius create a near surface layer comparable to the one observed by LORRI's HIRES sequence (Cheng *et al*. 2017, Jacobs *et al*. 2019a). The profile for the fractal aggregate haze layer is shown in Figure 83 (black). A vertically and horizontally constant phase function of 5 was assumed. Two exponentially decaying background number density profiles are shown for comparison, each with a different phase function and the parameters in Table 8. A phase function of 5 for spherical particles also produced best agreement with the observed I/F profile in this region. The decrease of the phase function from 20 to 5 was based on the considerable change in phase angle from 169° to 148°, which for spherical particles is very sensitive to small changes in the phase angle range due to the sharp forward scattering lobe.

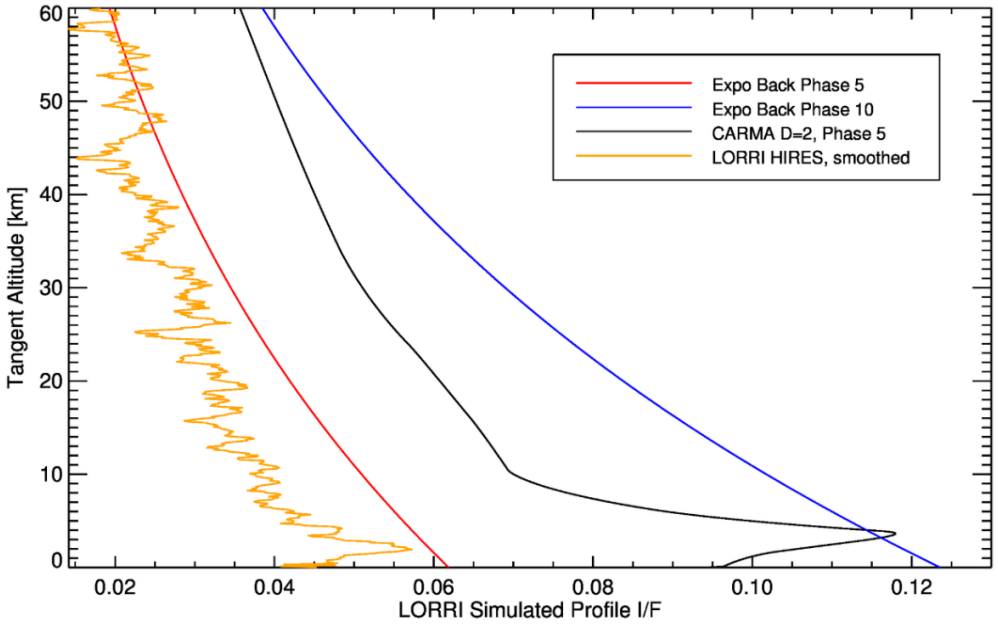

Figure 83: Profiles of HIRES for both the spherical particle exponential decay in number density background and CARMA derived fractal background hazes. Two different phase function values for spheres are shown (red and blue) The red phase function proved best agreement with LORRI I/F (orange) and was used for perturbed hazes below 60km. The CARMA background haze was composed of aggregates particles (Fractal dimension D=2) and produced a near surface layer comparable to observed.

The simulated surface layer has an amplitude ~0.5 (I/F/background - 1), thickness of ~8km (Altitude duration deviated from background), and height of max ~5km. The layer is embedded in a background haze that is 2x brighter than observed for almost the entire region below 60km. For comparison, the observed near surface layer has an amplitude of ~0.33, thickness of ~5km, and altitude of max ~2km. These values are sensitive to interpretation of stripping effects and surface location to around 1km.

The surface layer modeled by CARMA is understood to develop at the tropopause and may be an indicator of Pluto's tropospheric depth around the limb relative to different geographic regions. The sharp decrease of temperature in this altitude region

rapidly reduces particle sedimentation velocities, leading to a piling-up of haze particles. The temperature maximum right above the tropopause creates a region of more rapid coagulation (Maximum in coagulation kernel) where larger particles can form right before the tropopause pile-up (Gao *et al*. 2016). These combined conditions, which are most sensitive to Pluto's temperature profile, generate the maximum in haze particle number density (Total number density across distribution of ~1174 cm^{-3} at 3.8km—grid resolution 2.2km.), effective cross section, and I/F.

Using the spherical particle best fit phase function value of 5 for the image sequence phase angle of 148° and the parameters in Table 8, the exponential background haze was perturbed by both gravity wave orientations to compare low altitude haze layer structure to LORRI. A panel comparison is shown in Figure 84, with (a) the LORRI image, (b) the CARMA background fractal aggregate case containing the near surface layer, (c) the exponential background haze with southward wind orientation, and (d) the westward wind orientation. Both orientations are shown for the 4.5 ms^{-1} wind case. Due to the location on the limb, layer slopes and difference between slopes of the two orientations are negligible. The are some general agreements between both orientations' layers and the layers visible in the HIRES LORRI image. The first 3-4 layers appear most distinct, and simulated layers exhibit a sharp decrease in visibility around the same altitude. Specifically, a couplet of layers, although sharper, appear to match simulated layer position, separation, and thickness (marked with white arrows). Simulated layer edges are too sharp when compared to observed layers in general. This cannot be reconciled with LORRI's PSF function or image stripped and is likely due to a physical

process that is not being considered here (e.g. turbulent mixing at a certain threshold in density gradient).

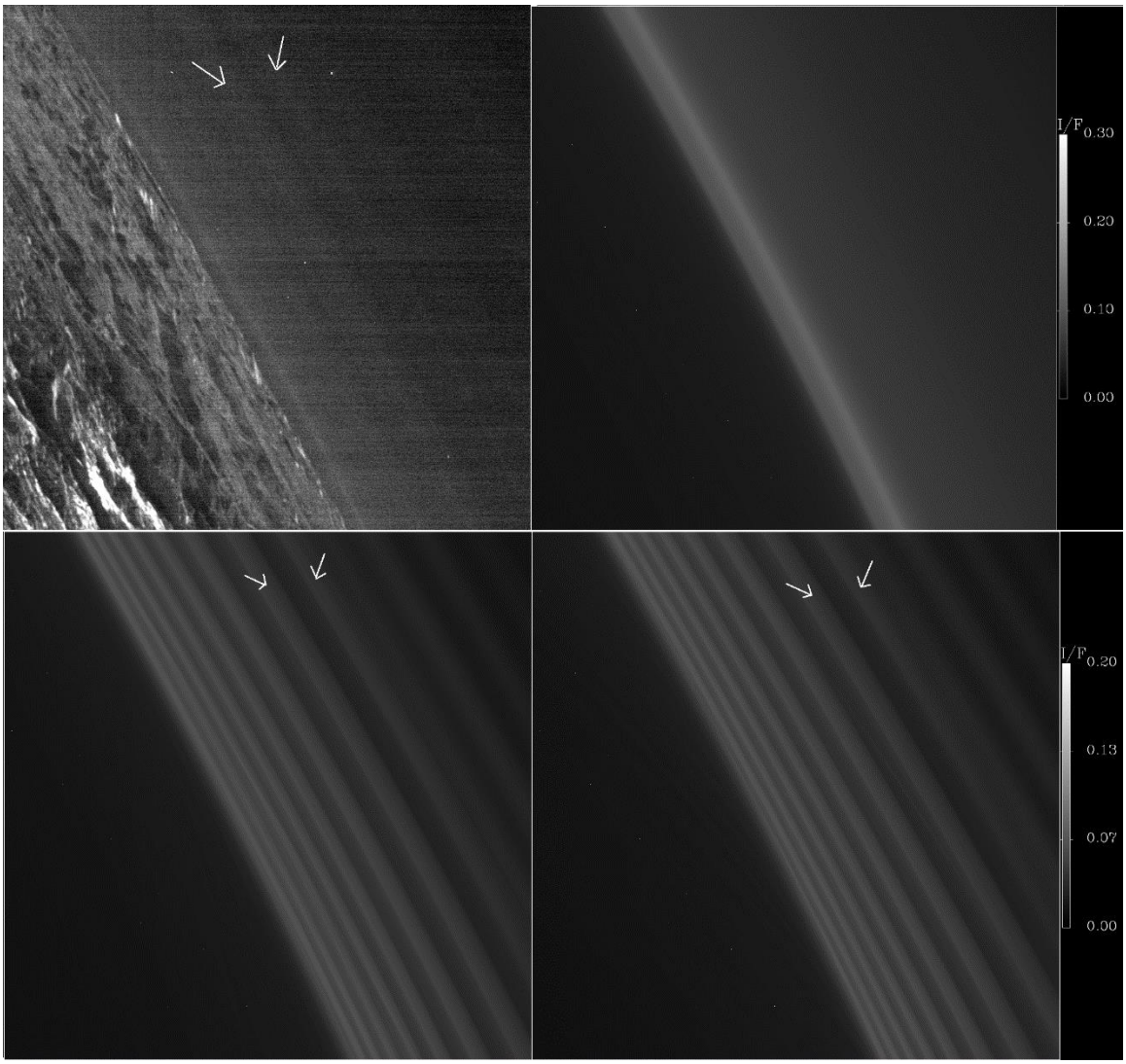

Figure 84: (a) Actual LORRI image, **(b)** simulation with CARMA aggregate background haze and surface layer, **(c)** simulation with exponential background haze and southward wind direction, and **(d)** the same exponential background haze with westward wind direction. Arrows indicate a layer couplet that best matches layers visible in the HIRES LORRI image. A sudden decrease in layer amplitude/sharpness is also consistent in altitude with where LORRI layer clarity decreases.

Waveforms corresponding to a LORRI radial profile that was analyzed in Jacobs *et al*. 2019a (red, top-left) are plotted in Figure 85, and corresponding simulated radial profiles for the 2.5 (black), 6 (green), and 10 ms^{-1} (purple) wind speed cases are shown at top-right. The three cases exemplify the full range in amplitude, vertical wavelength, and trend in amplitudes for the wind cases. A growth in layer amplitude with increasing altitude is replicated for the 2.5 ms^{-1} case and still present for 4.5 ms^{-1} but is lost for higher wind speeds. The 2.5 ms^{-1} has too large of an amplitude cut off around 35 km, indicating larger winds may be needed.

PSDs corresponding to waveforms are plotted in Figure 84 bottom. All wind speed cases are shown here. The power for a peak most likely matching the visible layering in the LORRI image best matches the power for the 2.5 ms^{-1} case. However, the best match in wavenumber (vertical wavelength) in terms of centering the LORRI peak (red) within the simulated peak (green) occurs for the 6 ms^{-1} case around 9 km.

Although box-averaging improved the LORRI profile stripping effects, a better method for comparing to simulated profiles may be taking multiple profile along the limb of different length and averaging with altitude to preserve limb parallel layers and get rid of oscillations due to stripping that is primarily horizontal and not parallel to the limb.

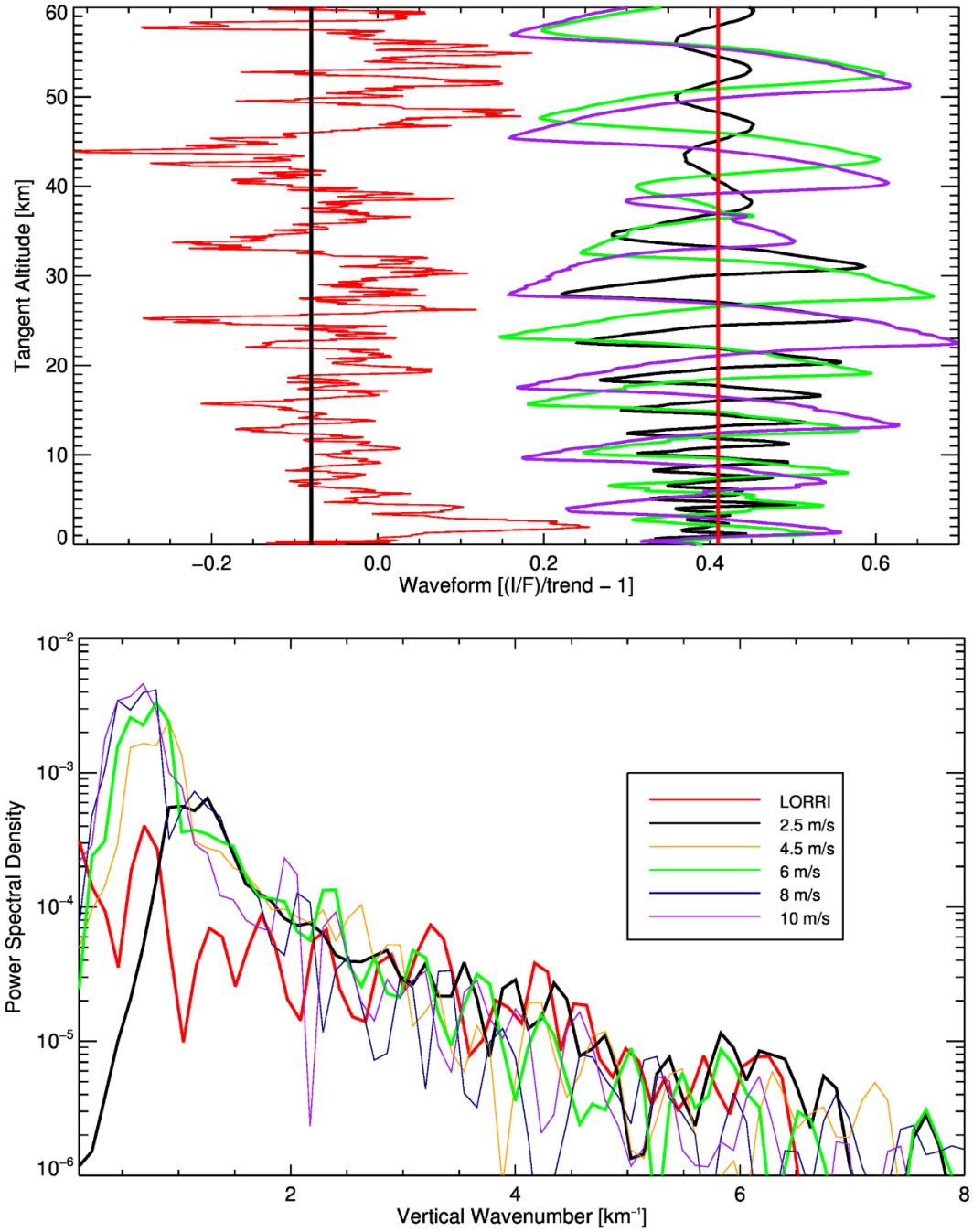

Figure 85: (Top) Waveforms and PSDs for the observed HIRES LORRI profile (red) and simulated profiles (2.5, 6, and 10 ms^{-1} cases). (Bottom) PSDs for the LORRI radial profile (red) and simulation radial profiles. Best agreement in peak location occurs for the 6 ms^{-1} case, but best agreement in power occurs for the 2.5 ms^{-1} case.

4.4 Conclusions and Implications

Three image sequences, which contained haze layer structure from three unique geographic regions, acted as three cases where the plausibility of haze layers formed by orographically driven gravity waves was explored. For each of these three cases, wind direction and speed were varied to conduct exact comparisons between LORRI images and those simulated using an optically thin, single scattering model.

The first geographic region case analyzed was the Tail of Cthulhu region () in the P_MULTI sequence with a resolution of 0.96 km/pix. A mosaic was constructed, and cartesian-to-polar transformation conducted, in order to compare directly with a LORRI mosaic. Terrain below the left half of this mosaic (frames A-C, Figure 69) where layers were most numerous and predominantly positively sloped was not well imaged. Although a southward wind direction generated layers with the same slope and slope trend as observed (positive, leveling off moving left-to-right), this slope orientation contradicts that (negative slopes) predicted by a GCM retrograde (westward) wind direction. Additionally, layer slopes were consistently much larger than observed for both wind directions considered (about 10x larger). These results combined with observations of multiple vertical scales (a larger vertical wavelength not handled here) and the superposition of positive and negative sloping with certain image processing steps implies that orographically generated gravity waves is unlikely to be the dominant layering mechanism occurring in this region. A mechanism like thermal tides (and the gravity waves different modes generate) may better match observations for this region.

The second geographic region analyzed was unique to the FULLFRAME sequence and was over the SP region (Q1 in Figure 69). This case was more extensively considered for containing layers driven by orographic gravity waves because observed layers were more consistently sloped (negative slope) and around much better imaged terrain that could plausibly generate substantial gravity waves (SP's basin walls and periodic ridges to the NE of SP). Simulated layer orientations (negative sloping) also agreed with the GCM predicted westward wind direction (but also did for the southward wind direction). However, simulated slope magnitudes were ~ 4x larger than observed. Intrinsic slopes ranged from 0.046 – 0.1 for the wind speed range of 2.5 – 10 ms^{-1}. Simulated slope magnitudes for all wind cases ended up being ~ 0.1, so that projection effects in this region could not reconcile the differences. Additionally, this implies a horizontal scale even larger than inferred from the observed slope of the layers in this region (~ 308 km and 845 km for the 8 km and 22 km λ_z, Jacobs *et al*. 2019a). This scale cannot be matched with the periodic ridges to the NE of SP, and it is still poorly understood how the comparable horizontal scale of the basin walls of SP could generate the observed layers. Lastly, the southward wind orientated layers can be tracked down to the limb as in the observations, but the westward wind orientated layers develop an interference pattern ~ 50 km altitude that is not present in observations. Although larger scale layers should be tested, this may indicate that observed layers increase in altitude toward the north (southward wind oriented) more than toward the east (westward wind oriented) regardless of the driving mechanism. The scale and orientation of layers may be more indicative again of a tidal mode as opposed to orographic gravity waves.

Lastly, the HIRES image taken above the region to the SW of SP was also considered as a candidate for layers generated by orographic gravity waves. Results from this sequence inherit higher uncertainty due to the limited spatial extent of the analysis but acts as a great case for comparing low altitude layers. A surface layer was best reproduced using an aggregate distribution generated by CARMA—further supporting the hypothesis that this near surface layer is microphysically driven, not dynamically (Gao *et al*. 2016, Cheng *et al*. 2017). After an initial growth in amplitude, observed layers appear to decrease in distinctness around 40 km, consistent with an amplitude drop off present in simulated layers for wind speeds less than or equal to 4.5 ms^{-1}. An observed layer couplet also matches two very distinct simulated layers. However, simulated layers are much sharper than observed, indicating the need to consider additional physical processes for layer simulation like turbulent mixing.

Overall, although additional modelling needs to be done for a larger range of horizontal scales, initial results indicate that orographically generated gravity waves are unlikely to be the dominate driving mechanism behind most visible haze layers observed in LORRI images. The large scales of layers and relatively less stringent constraints on terrain needed to generate waves for layering makes the tidally driven gravity waves a more likely driving mechanism candidate.

CHAPTER FIVE

Conclusions and Future Work: Waves in Planetary Atmospheres

5.1 Main Conclusions for Waves in Pluto's Atmosphere

Several haze layer characteristics were measured and outlined in Jacobs *et al*. 2019a, which can be compared to layer characteristics produced by dynamical models seeking to explain Pluto's observed haze layer structure. In Jacobs *et al*. 2019b, an example study of implementing a single scattering model to directly compare modelled haze layers with observations for validation of a dynamical model (orographic gravity waves) was conducted. Findings in these two companion studies build upon previous observations of waves in Pluto's atmosphere both before and after the July 14, 2015 New Horizons flyby (McCarthy *et al.* 2008, Person *et al.* 2008, Hubbard *et al.* 2009; Gladstone *et al*. 2016; Cheng *et al*. 2017) and previous modelling of haze layers (Person *et al*. 2008; Toigo *et al*. 2010; Gladstone *et al.* 2016; Cheng *et al.* 2017).

More than 20 haze layers were observed, with what appeared to be an average spacing/vertical wavelength of ~ 10.5 km. Layers appeared more numerous and distinct with considerable tilts relative to the limb at low latitudes, with some layers extending to higher latitudes. Haze layer vertical positions of two locations at the limb appeared stationary on timescales of 2 to 5 hours (Gladstone *et al*. 2016; Cheng *et al*. 2017).

Additional processing was then conducted in Jacobs *et al*. (2019a) to extract regions of radials profiles for which background trends were subtracted and waveforms generated. PSDs of these waveforms confirmed the vertical wavelengths observed in stellar occultations and the existence of larger vertical wavelengths for certain regions (~ 20-25 km and ~ 40 km, FULLFRAME nightside R2, Jacobs *et al*. 2019a). Slopes for several layers and geographic regions were extracted and combined with the measured vertical wavelengths and implied a horizontal scale of the layers to be ~ 300 – 900 km. The tilted layers appear and disappear on either side of a relatively level 25 km altitude layer confined to latitudes > 30 N and which rises from the surface. This layer was traceable for ~ 30 % of Pluto's circumference (Jacobs *et al*. 2019a).

Waves have long been postulated as the cause behind density fluctuations found in stellar occultations, but larger uncertainties exist in understanding the driving mechanism(s) behind these waves. It was first proposed by Toigo *et al*. (2010) that thermal tides (and their gravity wave modes) could explain fluctuations in density consistent with the saturated or nearly breaking gravity wave theoretical interpretation of observations. Their model predicted that wave perturbations and amplitudes would be confined to low latitudes (agreeing with the LORRI mosaic layered structure), and PSDs of their modelled temperature perturbation structure matched two vertical wavelengths (~ 8 km and 12 km) in stellar occultations at high altitudes and LORRI radial profiles at lower altitudes. However, the larger vertical wavelengths observed in LORRI radial profiles are not explained by the tidal model, and several layers can be tracked in high latitudes—especially the larger vertical scale layers. Additionally, the tidal model

predicted negligible horizontal winds, which is in contradiction of Pluto GCM predicted winds (up to 10 m/s). NH observed atmospheric structure (cooler upper atmosphere), ice distributions, and topography as well as Pluto GCM predicted winds should be used to update/inform this model and possibly reconcile these differences.

A second forcing mechanism—orographically driven gravity waves—was proposed in Gladstone *et al*. (2016), further outlined in Cheng *et al*. (2017), and tested to explain observations by NH/LORRI in this dissertation. Several images sequences corresponding to four unique geographic regions were explored to test the plausibility of layers occurring over these regions. Limited information and/or inconsistencies between simulated layers and observations made one geographic region (around SP and the mountain ridges to the ENE) the best case for generating orographic gravity wave layers. Current knowledge on wind direction, wind speed, horizontal scale of topography, vertical wavelengths, and projection effects produced considerable discrepancies between gravity wave model simulated layer slopes and those observed. The projection effects could not reconcile these differences, and horizontal scales of topography that would need to be used in the gravity wave model correspond to large scale sinusoidal ridges that have not yet been imaged on Pluto. A driving mechanism like thermal tides would have a less stringent topographic constraint. Additionally, an interference pattern present in E-W wind oriented simulated layers below ~ 50 km that is absent in N-S wind oriented layers contradicts the predicted GCM wind direction as observed layers are tracked down to the surface. This also may indicate that the layers are oriented with increasing altitude moving north regardless of the driving mechanism, but it should be noted that the

background haze is also more extended in the northern hemisphere (Cheng et al. 2017) so that the layers could be driven by this large scale feature.

Lastly, it should be emphasized that several wave types are likely present and superimposed in Pluto's atmosphere. The observations and analysis in this dissertation focused on wave type(s) that may be occurring in specific geographic regions to explain the visibility of haze layers with the observed horizontal and vertical scales. Although the importance of these wave types and scales were emphasized, waves with smaller scales than what can be resolved in images and atmospheric profiles are equally important for interactions with Pluto's general circulation.

5.2 Future Work

Although the LORRI dataset is rich, the same analysis should be conducted on MVIC images to test for consistency and sample wave characteristics for additional geographic regions. More extensive background subtraction techniques should also be used for LORRI images to refine results. In addition, wavelet analysis may be used to better handle waveform variation with location and altitude. These observations should then be compared with all current stellar occultation datasets and matches made for the same altitude range and geographic regions sampled. Stellar occultations also provide the unique opportunity to sample Pluto's waves over a larger time range. A table showing certain selected occultations over ~ 31 years that can be used, or have been used, to study waves is shown in Table 13.

Table 13: Stellar occultations/studies for the past 31 years that can be combined with NH data to show how dynamics vary with time and location.

Team	Date	Site	Citation
MIT	1988 Jun 08	KAO	Elliot & Young 1992; Elliot Person & Qu 2003a
MIT	2002 Aug 21	UH2.2m	Elliot et al 2003b
Paris	2002 Aug 21	CFHT	Sicardy et al. 2003
SwRI	2006 Jun 12	AAT	Young et al. 2008
SwRI	2007 Mar 18	WIYN	Young et al 2007
MIT	2007 Mar 18	MMT	Person et al. 2008; McCarthy et al. 2008; Hubbard et al. 2009
Paris	2012 Jul 18	VLT	Dias-Oliveira et al. 2015
Paris	2013 May 04	Paranal	Dias-Oliveira et al. 2015
MIT	2015 Jun 29	Sofia	Person et al. 2015
SwRI	2018 Aug 15	SPM	Young et al. 2018

Modelling will benefit substantially from the coupling and further analysis of these datasets. In addition to recent development of the Toigo *et al*. 2010 thermal tides model, a NASA New Frontiers Data Analysis Program (NFDAP) proposal was submitted by NH team members, stellar occultations scientists, and the author of this dissertation to continue to explore wave dynamics in Pluto's atmosphere—and ultimately the influence of waves on the mean state. The proposal contains three phases— (1) the continuation of extracting wave properties from observations, (2) quantifying and modelling wave generation and propagation, and (3) wave-mean interaction modelling in a GCM. The contributions toward (1) made by this dissertation have been outlined and general plans laid out. Two wave generation mechanisms will be focused on as in this dissertation—orographic driven gravity waves and tidally driven gravity waves. Special conditions for vertical propagation will be used to constrain the cases considered in the orographic gravity wave model. To date the model has only handled one horizontal wave number component at a time at the scale believed to generate the visible layers. However,

topography on Pluto has multiple scales which should be represented as a Fourier series with multiple wavenumbers. A more detailed topographic input such as this and the consideration of smaller scale waves will be critical to representing the entire wave spectrum likely present in Pluto's atmosphere. These wave characteristics, as well as constraints on how they propagate vertically and horizontally, will then be used to inform a Pluto GCM in phase (3). Wave scales and spatial variation generated by tidal modes will also be used as their superposition with orographic waves is likely occurring on Pluto.

Gravity waves have been known to affect the mean state of several planetary atmospheres through their amplitude growth, instability, and momentum deposition as increases in turbulence and eddy viscosity. One example is the quasi-biennial oscillation on Earth (Lindzen 1981). Gravity wave breaking is also known to cause a seasonal cool mesosphere/mesopause (Thomas 1996). Pluto's upper atmosphere was discovered to be much cooler than expected upon flyby of NH. Several mechanisms for cooling have been proposed including haze heating and cooling which may surpasses gas heating and cooling rates (Zhang *et al*. 2017). Dissipating waves in Pluto's middle and upper atmosphere could also cause heating and cooling as in Earth's atmosphere—which typically heats lower regions and cools upper regions due to energy redistribution. Induced vertical motions on the general circulation may also considerably affect vertical profile concentrations of certain molecules like CH_4 and alter horizontal wind trends that have been adopted in Chapter 4 from the Pluto GCM.

Applications of findings and continuation of research contained in this dissertation will help answer the following three broader scientific questions raised by New Horizons—(i) How variable is the eddy diffusion coefficient with time and location? (ii) How does momentum carried by waves affect the general circulation? (iii) How does the energy flux carried by the observed waves compare with other energy sources, and does it affect Pluto's unexpectedly cold temperature? All three of these also pertain to CH_4 concentrations, transport, and deposition which drives haze formation. This continued research will also help provide an archive for any future wave studies of Pluto from upcoming stellar occultations and missions. Pluto presents a unique natural laboratory to better understand wave generation and propagation, with haze as a tracer for wave motions throughout a deep vertical column of the atmosphere (at least 5 scale heights). Better understanding waves in Pluto's atmosphere will likely lead to broader implications.

REFERENCES

Bertrand, T. and F. Forget (2017). 3D modeling of organic haze in Pluto's atmosphere. Icarus 287, 72-86.

Bertrand, T. et al. (2018). The nitrogen cycles on Pluto over seasonal and astronomical timescales. Icarus 309, 277-296.

Bertrand, T. et al. (2019a). The CH_4 cycles on Pluto over seasonal and astronomical timescales. Icarus 329, 148-165.

Bertrand, T, F. Forget, A. Toigo, and D. Hinson (2019b). Pluto's Atmosphere Dynamics How the Nitrogen Heart Regulates the Circulation. Pluto System After New Horizons, Applied Physics Lab, July 2019.

Bertrand, T, F. Forget, O. White, B. Schmitt (2019c). Pluto's beating heart regulates the atmospheric circulation: results from high resolution and multi-year numerical climate simulations. Submitted to JGR.

Bohren, C. and D. R. Huffman (1998). Absorption and Scattering of Light by Small Particles. Ed. by C. Bohren and D. R. Huffman. Wiley Science Paperback Series.

Cabane, M., P. Rannou, E. Chassefiere, and G. Israel (1993). Fractal aggregates in Titan's atmosphere. Planetary and Space Science 41, 257-267.

Cheng, A. F. et al. (2008). Long-Range Reconnaissance Imager on New Horizons. Icarus 140:189-215. doi: 10.1007/s1121400792716.

Cheng, A.F. et al. (2017). Haze in Pluto's atmosphere. Icarus 290, 112-133. doi: 10.1016/j.icarus.2017.02.024.

Crane, Co. (1988). Flow of fluids through valves, settings, and pipe. Technical paper. Crane Co.

Dias-Oliveira, A. et al. (2015). Pluto's Atmosphere from Stellar Occultations in 2012 and 2013. The Astrophysical Journal 811, 53.

Elliot, J. L. and L. A. Young (1992). Analysis of Stellar Occultation Data for Planetary Atmospheres. I. Model Fitting Application to Pluto. The Astronomical Journal 103, 991.

Elliot, J. L., M. J. Person, and S. Qu (2003a). Analysis of Stellar Occultation Data. II. Inversion, with Application to Pluto and Triton. The Astronomical Journal 126, 1041-1079.

Elliot, J. L. et al. (2003b). The recent expansion of Pluto's atmosphere. Nature 424, 165-168.

Forget, F., T. et al. (2016). A post-new horizons global climate model of Pluto including the N2, CH4 and CO cycles. Icarus 287, 54-71. doi: 10.1016/j.icarus.2016.11.038.

Fray, N. and B. Schmitt (2009). Sublimation of ices of astrophysical interest: A bibliographic review. In: 57, pp. 2053-2080. doi: 10.1016/j.pss.2009.09.011.

Gao, P. et al. (2016). Constraints on the Microphysics of Pluto's Photochemical Haze from New Horizons Observations. Icarus 287, 116-123.

Gladstone, G. R. et al. (2016). The atmosphere of Pluto as observed by New Horizons. Science 351, aad8866.

Gladstone, G. R. (1992). Simulated images of the plasmasphere. Proc. SPIE 1744, Instrumentation for Magnetospheric Imagery. doi: 10.1117/12.60590.

Grundy, W. M., C. B. Olkin, L. A. Young, M. W. Buie, E. F. Young (2013). Near-infrared spectral monitoring of Pluto's ices: Spatial distribution and secular evolution. Icarus 223, 710–721. doi:10.1016/j.icarus.2013.01.019.

Guo, Y. and R. W. Farquhar (2008). New Horizons Mission Design. Space Science Reviews 140, 49-74.

Hinson, D. P. et al. (2017). Radio occultation measurements of Pluto’s neutral atmosphere with New Horizons. Icarus 290:96-111. doi: 10.1016/j.icarus.2017.02.031.

Holton, J. R. (2004). 4th ed.; New York, NY: Elsevier/Academic.

Horanyi, M., A. Poppe, and Z. Sternovsky (2016). Dust ablation in Pluto's atmosphere. EGU General Assembly Conference Abstracts 18, 3652.

Hubbard, W. B., D. M. Hunten, S. W. Dieters, K. M. Hill, R. D. Watson (1988). Occultation evidence for an atmosphere on Pluto. Nature 336, 452-454 (1988). doi:10.1038/336452a0.

Hubbard, W. B. et al. (2009). Buoyancy waves in Pluto’s high atmosphere: Implications for stellar occultations. Icarus 204, 284–289. doi:10.1016/j.icarus.2009.06.022.

Jacobs et. al. (2019a). LORRI Observations of Waves in Pluto’s Atmosphere: submitted to Icarus October 2019.

Jacobs et al. (2019b). Simulations of Observed Haze Layer Structure in Pluto’s Atmosphere (In preparation): to be submitted to Icarus in November 2019.

Khare, B.N., Carl Sagan, E.T. Arakawa, F. Suits, T.A. Callcott, and M.W. Williams (1984). Optical constants of organic tholins produced in a simulated Titanian atmosphere: From soft x-ray to microwave frequencies. Icarus 60, pp. 127-137.

Lavvas, P. et al. (2009). The detached haze layer in Titan's mesosphere. Icarus 201, pp. 626-633.

Lavvas, P., et al. (2010). Titan's vertical aerosol structure at the Huygens landing site: Constraints on particle size, density, charge, and refractive index. In: Icarus 210, pp. 832-842.

Lavvas, P., et al. (2011). Surface Chemistry and Particle Shape: Processes for the Evolution of Aerosols in Titan's Atmosphere. ApJ 728.2, p. 80.

Lorenz, R. D., L. A. Young, and F. Ferri (2014). Gravity waves in Titan's lower stratosphere from Huygens probe in situ temperature measurements. Icarus 227, 49-55.

Sicardy, B. et al. (2003). Large changes in Pluto's atmosphere as revealed by recent stellar occultations. Nature 424, 168-170.

Summers, M. E. et al. (2015). Haze Production in Pluto's Atmosphere. AGU Fall Meeting Abstracts.

Lellouch, E. et al. (2011). High resolution spectroscopy of Pluto’s atmosphere: detection of the 2.3 μm CH4 bands and evidence for carbon monoxide. Astron. & Astrophys. 530, L4.

Lellouch, E. et al. (2016). Detection of CO and HCN in Pluto's atmosphere with ALMA. Icarus 286, 289-307.

Lindzen, R. S. (1981). Turbulence and stress owing to gravity wave and tidal breakdown. Journal of Geophysical Research 86, 9707-9714.

Marrero, T. R. and E. A. Mason (1972). Gaseous Diffusion Coefficients, Journal of Physical and Chemical Reference Data 1.1, pp. 3118. doi: 10. 1063/1.3253094.

McCarthy, D.W et al. (2008). Long-wavelength density fluctuations resolved in Pluto’s high atmosphere. Astron. J. 136, 1519–1522.

Mishchenko, M. I., et al. 1996. T-Matrix computations of light scattering by nonspherical particles: a review. J. Quant. Spectrosc. Radiat. Transfer, 55, 535.

Moore, J.M. et. al. (2016). The geology of Pluto and Charon through the eyes of New Horizons. Science, 351: 1284-93.

Nappo, Carmen J (2002). Introduction to Atmospheric Gravity Waves. San Diego, CA: Elsevier.

Olkin, C. B. et al. (2014). Pluto's atmospheric structure from the July 2007 stellar occultation. Icarus 239, 15-22.

Person, M.J. et al. (2008). Waves in Pluto's upper atmosphere. Astron. J. 136, 1510–1518.

Press, William H. et al. (2003). Numerical Recipes in FORTRAN 77: the Art of Scientific Computing, 2nd Edition. Cambridge University Press, 542-551.

Petty, Grant W. (2006). A First Course in Atmospheric Radiation (2nd Ed.) Sundog Publishing. isbn: 0972903313.

Pruppacher, Hans R and 1940 Klett James D. (1997). Microphysics of clouds and precipitation. Boston : Kluwer Academic Publishers. isbn: 0792342119 (alk. paper).

Schenk, P. M., et al. (2018). Basins, fractures and volcanoes: Global cartography and topography of Pluto from New Horizons. Icarus 314, 400-433.

Seinfeld, John H. and Spyros N. Pandis (2006). Atmospheric chemistry and physics from air pollution to climate change. Hoboken, N.J. J. Wiley. isbn: 0-471-72017-8.

Sicardy, B. et al. (2003). Large changes in Pluto's atmosphere as revealed by recent stellar occultations. Nature 424, 168-170.

Stern, S. A. et al. (2008). Alice: The Ultraviolet Imaging Spectrograph Aboard the New Horizons Pluto-Kuiper Belt Mission. Space Science Reviews 140, 155-187.

Stern, S., Tholen, D., Ruskin, A., Guerrieri, M., & Matthews, M. (1997). Pluto and Charon. Tucson: University of Arizona Press.

Stevens, M. H., D. F. Strobel, M. E. Summers, and R. V. Yelle (1992). On the thermal structure of Triton's thermosphere. Geophysical Research Letters 19, 669-672.

Strobel D. F. (2009). Titan's hydrodynamically escaping atmosphere: Escape rates and the structure of the exobase region. Icarus 202, 632–641.

Summers, M. E., D. F. Strobel, and G. R. Gladstone (1997). Chemical Models of Pluto's Atmosphere. Pluto and Charon 391.

Summers, M. E. et al. (2016). The Neutral Atmospheres of Pluto and Charon. Lunar and Planetary Science Conference. Vol. 47. Lunar and Planetary Science Conference, p. 2864.

Thomas, G. E. (1996). Global change in the mesosphere-lower thermosphere region: has it already arrived? Journal of Atmospheric and Terrestrial Physics 58, pp. 1629-1656.

Toigo, A.D. et al. (2010). Thermal tides on Pluto. Icarus 208, 402-411.

Tomasko, M. G. et al. (2008). A model of Titan's aerosols based on measurements made inside the atmosphere. Planet. Space Sci. 56, 669-707.

Tyler, G. L. et al. (2008). The New Horizons Radio Science Experiment (REX). Space Science Reviews 140, 217-259.

Wong, M. L. et al. (2017), The photochemistry of Pluto's atmosphere as illuminated by New Horizons. Icarus 287, 110-115.

Young, L. A. et al. (2008). New Horizons: Anticipated Scientific Investigations at the Pluto System. Space Science Reviews 140, 93-127.

Young, L. A. (2009). Rapid Computation of Occultation Lightcurves Using Fourier Decomposition. The Astronomical Journal 137, 3398-3403.

Young, L. A. et al. (2007). Visible and Near-IR Observations of the 2007 March 18 Occultation by Pluto. AAS/Division for Planetary Sciences Meeting Abstracts #39 62.04.

Young, E. F. (2008). Vertical Structure in Pluto's Atmosphere from the 2006 June 12 Stellar Occultation. The Astronomical Journal 136, 1757-1769.

Young, E. F. et al. (2018). The Stellar Occultation by Pluto on 15-Aug-2018. AAS/Division for Planetary Sciences Meeting Abstracts 502.01.

Yung, Y. L. et al. (1984). Photochemistry of the atmosphere of Titan - Comparison between model and observations. The Astrophysical Journal Supplement Series 55, 465-506.

Zhang et al. (2017). Haze heats Pluto's atmosphere yet explains its cold temperature. Nature 551: 352-355; doi: 10.1038/nature24465.

Zhu, X., D. F. Strobel, and J. T. Erwin (2014). The density and thermal structure of Pluto's atmosphere and associated escape processes and rates. Icarus 228, 301-314.

BIOGRAPHY

Adam Jacobs graduated from Halifax Area High School in Halifax, Pennsylvania, in 2007. He received his Bachelor of Arts in Physics and Bachelor of Science in Meteorology from Millersville University in 2012. Adam then attended George Mason University for graduate school where he received a Master of Science in Applied and Engineering Physics in 2016 and a Ph.D. in Physics in 2019. Adam is pursuing a career in space science and engineering.